River-Floodplain Connectivity and Sediment Transport Potential: Applications to Sediment Dynamics on Floodplains and Juvenile Freshwater Mussel Settling in Rivers

Sumaiya

Dissertation submitted to the faculty of the Virginia Polytechnic Institute and State University in partial fulfillment of the requirements for the degree of

Doctor of Philosophy
In
Biological Systems Engineering

Jonathan A. Czuba, Chair
Tess Wynn Thompson
W. Cully Hession
Kyle Strom

September 15, 2022
Blacksburg, Virginia

Keywords: River-floodplain connectivity, sediment transport, numerical modeling, and freshwater mussel

River-Floodplain Connectivity and Sediment Transport Potential: Applications to Sediment Dynamics on Floodplains and Juvenile Freshwater Mussel Settling in Rivers

Sumaiya

ABSTRACT

River-floodplain connectivity is the degree of water-driven transport of matter, energy, and organisms between rivers and their floodplains. Recent advancement of high-resolution lidar data and numerical modeling is helpful to explore river-floodplain connectivity precisely to improve our predictions of sediment transport and deposition on floodplains. In the present work, we studied floodplain sediment transport and deposition, and juvenile mussel settling in three river systems in the US. A two-dimensional hydrodynamic model was developed and simulated model results were coupled with field measurements to study river-floodplain systems of the East Fork White River in Indiana, South River in Virginia, and Dan River in North Carolina. Results show that the East Fork White River in Indiana is capable of supplying sand to the channels on the floodplain and these floodplain channels can transport sand in suspension and gravel as bedload. These floodplain channels are supply limited under the current hydrologic regime and identified as net erosional. On the South River floodplain in Virginia, incorporating hydrologic flowpaths as an explicit measure of river-floodplain connectivity can improve predictions of floodplain sediment deposition. Three regression models were developed incorporating flow pathways and the best model was applied to hydrodynamic model results to create a spatial map of floodplain sedimentation rate. The deposition map highlights how floodplain topography and river-floodplain connectivity affect sedimentation rates and can help inform the development of floodplain sediment budgets. Lastly, streamflow conditions were investigated in the Dan River, North Carolina as they

affect juvenile freshwater mussel settling. Two uplooking velocity sensors on the river bed were deployed and hydraulic parameters were measured for a 7-mo period in May-November 2019 to estimate the juvenile mussel settling. Results show that juvenile freshwater mussels as large as 280-508 µm could always be suspended during our study period and not be able to settle onto the river bed at the location of our velocity sensors. Therefore, the flow and shear velocity during our study period was high enough to prohibit the recruitment of juvenile freshwater mussels from settling out of suspension at the sensor locations. Modest flow obstructions such as large boulders, downed trees, or large wood that create downstream wakes may be important features that provide suitable conditions for the settling of juvenile freshwater mussels onto the river bed. Furthermore, low flows have been increasing since the year 2000 which may be exacerbating the decline in freshwater mussel populations.

River-Floodplain Connectivity and Sediment Transport Potential: Applications to Sediment Dynamics on Floodplains and Juvenile Freshwater Mussel Settling in Rivers

Sumaiya

GENERAL AUDIENCE ABSTRACT

Human civilization has developed near rivers due to the wide range of benefits provided by rivers. Rivers provide food, water, and energy to more than 2.7 billion people around the world. However, the health of the rivers is degrading rapidly to meet the increasing demand of the growing population. We studied water, sediment, and mussel transport in the three rivers in the US: East Fork White River in Indiana, South River in Virginia, and Dan River in North Carolina. These rivers play an important role in agriculture, water supply, sediment, and nutrient transport of the surrounding environment. Our research work on East Fork White River in Indiana, USA shows that the area directly adjacent to the river is eroding, which is important information for river managers and policymakers. As part of that work, we identified the potential of various sizes of sediment to move over this area at different flows and developed a method to predict the largest sediment size that could be moved in water and hopping along the ground. This method is also applicable to other areas along rivers and the coast. We estimated the sediment deposition rate, deposition volume, and prepared a spatial map of the sediment deposition pattern for the South River floodplain in Virginia. From this map, deposition hot spots could be identified. We estimated that 66% of the sediment deposited adjacent to the South River was located in 32% of the area. This information will be helpful for understanding how sediment and sediment-associated pollutants deposit around rivers. Our work on the Dan River in North Carolina was focused on freshwater mussels. Our results showed that juvenile freshwater mussels could not have settled onto the river bed at the location of our measurements. Historical data reveal that freshwater mussels are declining

at an alarming rate in that river, posing a threat to the river environment. We identified that streamflow has been increasing over the last two decades, which could be a potential cause of declining freshwater mussels.

ACKNOWLEDGMENTS

First of all, I am grateful to the almighty Allah who has surrounded me with the most supporting people and provided me with the opportunity to complete this research.

I would like to express my sincere gratitude to my Ph.D. advisor, Jonathan A. Czuba, for his continuous guidance, support, invaluable suggestions, affectionate encouragement, and motivation in difficult times which were extremely helpful in accomplishing this study over the last four years. I will always be grateful for having him as my mentor and getting the opportunity to work as part of his research team. His mentorship, support, and motivation helped me pursue my research interests while balancing my personal life, and getting prepared for my future career.

Next, I would like to express my profound respect to my committee members, Tess Wynn Thompson, Cully Hession, and Kyle Strom for providing me with valuable feedback, comments, and suggestions throughout my Ph.D. program.

I would like to extend my appreciation the faculty, staff, and students of the Department of Biological Systems Engineering at Virginia Tech. I enjoyed my time being with them and have learned many lessons from them.

Financial support for this dissertation was provided by the Virginia Agricultural Experiment Station, USDA Hatch program (1017457), and Pratt fellowship from the Department of Biological Systems Engineering at Virginia Tech. I thank each one of them for supporting my research.

I offer my sincerest gratitude to my M.Sc. supervisor, Dr. Anisul Haque, Professor, Institute of Water and Flood Management (IWFM), Bangladesh University of Engineering

and Technology (BUET), for his faith on me. He has always believed in me, supported me during my tough time, and the first person who encouraged me to pursue a doctoral research.

I also want to thank my friend Roja, Anik, Sanjid, Archi, Nabil, Sajal, Kakon, Sefat Banee, Zakia, Nikita, who comforted me during my rough times and made my life full of joy and happiness during my Ph.D. studies.

Finally, and most importantly, I would like to thank my husband and my parents for their motivation and unconditional support that they have always provided me with.

DEDICATION

To my husband *Chayan* and my best friend *Julfa* without their support, this journey would not have been possible.

Table of Contents

List of Tables

List of Figures

Chapter 1 Introduction

Riverine ecosystems provide food, water, and energy that support biodiversity and peoples' livelihoods (Dudgeon et al., 2019; FAO, 2015; Postel & Carpenter, 1997). Perturbing the hydrologic, chemical, and geomorphic functioning of rivers can degrade aquatic and riparian systems (Roy et al., 2016; Van Metre et al., 2019). Various factors determine the healthy functioning of riverine ecosystems including river flow, riparian zone, physical structure, water quality, cutting and dredging, level of exploitation, and barriers to floodplain connectivity (Norris and Thomas, 1999). Acknowledgment of the benefits provided by riverine ecosystems and due to increasing threats, there is a societal desire to restore and conserve the functioning of riverine systems supported by regional and national legislation and policies (Acreman & Dunbar, 2004).

Floodplains are complex geomorphic features in the riparian landscape with positive and negative relief (Lewin & Ashworth, 2014). Negative topographic relief can lead to gradual flooding across a floodplain and establish river-floodplain connectivity (Czuba et al., 2019; Lindroth et al., 2020; Xu et al., 2021). River-floodplain connectivity is the degree of water-driven transport of matter, energy, and organisms between rivers and their floodplains (Amoros and Bornette, 2002; Bracken et al., 2015; Covino, 2017; Freeman et al., 2007; Tockner et al., 2000). Floodwaters can inundate a floodplain through floodplain channels, breaches, crevasses, chutes, and form flowpaths through which connectivity establishes. During an overbank flood, sediment from the main river channel can be transported to the floodplain through these flow pathways and become deposited or resuspended on the floodplain resulting in floodplain erosion/deposition depending on the flow conditions and supplied sediment (Zwoliński, 1992).

Freshwater mussels are an integral part of riverine ecosystems because of their role in water filtration, nutrient cycling, and providing habitat for other aquatic organisms (Geist 2010; Lummer et al. 2016; Vaughn et al. 2008; Vaughn and Hakenkamp 2001). Despite their importance, currently they are recognized as one of the most imperiled faunal groups globally (Lopes- Lima et al. 2017; Master et al. 2000; Williams et al. 1993). Alteration of flow regimes and channel characteristics by man-made modifications like dam construction or changes in the climate has significantly reduced the biodiversity in many riverine ecosystems including freshwater mussels (Haag 2012; Poff et al. 2007).

Recognizing the role of floodplain channels, river-floodplain connectivity, and freshwater mussels for providing riverine ecosystem services, this dissertation incorporates high-resolution topographic data into numerical models, along with field measurements, to better quantify river-floodplain processes to highlight the functioning of each component to ensure sustainability of the riverine ecosystem.

1.1 Goals and objectives

The goal of this research is to improve the understanding of sediment and juvenile freshwater mussel transport in rivers and the implication of river-floodplain connectivity in predictions of floodplain morphodynamic evolution. To accomplish this goal, the following primary objectives were explored:

1. We proposed a method of probabilistically integrating the largest sediment size that can be moved at various flows to predict the upper end of the grain size distribution in suspension and in bed material, which could be applied to predict the deposition/erosion potential of sediment in a channelized floodplain.

2. We proposed three multiple linear regression models incorporating flow pathways as an explicit measure of river-floodplain connectivity to improve predictions of sediment deposition on floodplains.
3. We identified how flow conditions have been changing over time as a potential explanation for the decline in freshwater mussel populations in the Dan River, North Carolina.

1.2 Dissertation organization

This dissertation is composed of five chapters. Chapter 1 is an introduction to the overall dissertation. Chapter 2 discusses the research performed to accomplish the first objective and has been published as Sumaiya et al. (2021) in Water Resources Research. Chapter 3 discusses the research performed to accomplish second objective and is under review in a peer-reviewed journal. Chapter 4 discusses the research performed to accomplish third objective and is intended to be submitted for publication in peer-reviewed journal. The author of this dissertation was the lead author on all three of these manuscripts. Chapter 5 contains the overall conclusions of this research and summarizes future research direction.

References for Chapter 1

Acreman, M. C., & Dunbar, M. J. (2004). Defining environmental river flow requirements–a review. Hydrology and Earth System Sciences, 8(5), 861-876. https://doi.org/10.5194/hess-8-861-2004

Amoros, C., & Bornette, G. (2002). Connectivity and biocomplexity in waterbodies of riverine floodplains. *Freshwater biology*, 47(4), 761-776. https://doi.org/10.1046/j.1365-2427.2002.00905.x

Bracken, L. J., Turnbull, L., Wainwright, J., & Bogaart, P. (2015). Sediment connectivity: a framework for understanding sediment transfer at multiple scales. *Earth Surface Processes and Landforms*, 40(2), 177-188. https://doi.org/10.1002/esp.3635

Covino, T. (2017). Hydrologic connectivity as a framework for understanding biogeochemical flux through watersheds and along fluvial networks. *Geomorphology*, 277, 133-144. https://doi.org/10.1016/j.geomorph.2016.09.030

Czuba, J. A., David, S. R., Edmonds, D. A., & Ward, A. S. (2019). Dynamics of Surface-Water Connectivity in a Low-Gradient Meandering River Floodplain. *Water Resources Research*, *55*(3), 1849–1870. https://doi.org/10.1029/2018WR023527

Dudgeon, D. (2019). Multiple threats imperil freshwater biodiversity in the Anthropocene. *Current Biology*, 29(19), R960-R967. https://doi.org/10.1016/j.cub.2019.08.002

FAO. (2015) Lakes and rivers key to livelihoods of millions, http://www.fao.org/news/story/en/item/276122/icode/

Freeman, M. C., Pringle, C. M., & Jackson, C. R. (2007). Hydrologic connectivity and the contribution of stream headwaters to ecological integrity at regional scales 1. *JAWRA Journal of the American Water Resources Association*, 43(1), 5-14. DOI: 10.1111/j.1752-1688.2007.00002.x

Geist, J. (2010). Strategies for the conservation of endangered freshwater pearl mussels (Margaritifera margaritifera L.): a synthesis of conservation genetics and ecology. *Hydrobiologia*, *644*(1), 69-88. https://doi.org/10.1007/s10750-010-0190-2

Haag, W. R. (2012). *North American freshwater mussels: natural history, ecology, and conservation*. Cambridge University Press.

Lewin, J., & Ashworth, P. J. (2014). The negative relief of large river floodplains. *Earth-Science Reviews*, *129*, 1–23. https://doi.org/10.1016/j.earscirev.2013.10.014

Lindroth, E. M., Rhoads, B. L., Castillo, C. R., Czuba, J. A., Güneralp, İ., & Edmonds, D. (2020). Spatial variability in bankfull stage and bank elevations of lowland meandering rivers: Relation to rating curves and channel planform characteristics. *Water Resources Research*, *56*(8), e2020WR027477.

Lopes-Lima, M., Sousa, R., Geist, J., Aldridge, D. C., Araujo, R., Bergengren, J., ... & Zogaris, S. (2017). Conservation status of freshwater mussels in Europe: state of the art and future challenges. *Biological reviews*, *92*(1), 572-607. https://doi.org/10.1111/brv.12244

Lummer, E. M., Auerswald, K., & Geist, J. (2016). Fine sediment as environmental stressor affecting freshwater mussel behavior and ecosystem services. *Science of the Total Environment*, *571*, 1340-1348. https://doi.org/10.1016/j.scitotenv.2016.07.027

Master, L. L., Stein, B. A., & Hammerson, G. A. K. (2000). Vanishing assets: conservation status of US species. In *Precious heritage*. Oxford University Press.

Norris, R. H., & Thoms, M. C. (1999). What is river health?. *Freshwater biology*, *41*(2), 197-209. https://doi.org/10.1046/j.1365-2427.1999.00425.x

Poff, N. L., Olden, J. D., Merritt, D. M., & Pepin, D. M. (2007). Homogenization of regional river dynamics by dams and global biodiversity implications. *Proceedings of the National Academy of Sciences*, *104*(14), 5732-5737. https://doi.org/10.1073/pnas.0609812104

Postel, S., & Carpenter, S. R. (1997). Freshwater ecosystem services (chapter 11). In G. C. Daily (Ed.), *Natures services: Societal dependence on natural ecosystems* (pp. 195–214). Washington, DC: Island Press.

Roy, A. H., Capps, K. A., El-Sabaawi, R. W., Jones, K. L., Parr, T. B., Ramírez, A., ... & Wenger, S. J. (2016). Urbanization and stream ecology: diverse mechanisms of change. *Freshwater Science*, *35*(1), 272-277. https://doi.org/10.1086/685097

Tockner, K., Malard, F., & Ward, J. V. (2000). An extension of the flood pulse concept. *Hydrological processes*, 14(16-17), 2861-2883. https://doi.org/10.1002/1099-1085(200011/12)14:16/17%3C2861::AID-HYP124%3E3.0.CO;2-F

Van Metre, P. C., Waite, I. R., Qi, S., Mahler, B., Terando, A., Wieczorek, M., ... & Carlisle, D. (2019). Projected urban growth in the southeastern USA puts small streams at risk. *PloS one*, *14*(10), e0222714. https://doi.org/10.1371/journal.pone.0222714

Vaughn, C. C., Nichols, S. J., & Spooner, D. E. (2008). Community and foodweb ecology of freshwater mussels. *Journal of the North American Benthological Society*, *27*(2), 409-423. https://doi.org/10.1899/07-058.1

Vaughn, C. C., & Hakenkamp, C. C. (2001). The functional role of burrowing bivalves in freshwater ecosystems. *Freshwater Biology*, *46*(11), 1431-1446. https://doi.org/10.1046/j.1365-2427.2001.00771.x

Williams, J. D., Warren Jr, M. L., Cummings, K. S., Harris, J. L., & Neves, R. J. (1993). Conservation status of freshwater mussels of the United States and Canada. *Fisheries*, *18*(9), 6-22. https://doi.org/10.1577/1548-8446(1993)018%3C0006:CSOFMO%3E2.0.CO;2

Xu, H., Steeg, S., Sullivan, J., Shelley, D., Cely, J. E., Viparelli, E., et al., (2020). Intermittent channel systems of a low-relief, low-gradient floodplain: Comparison of automatic extraction methods. *Water Resources Research, 56.* https://doi.org/10.1029/2020WR027603

Zwoliński, Z. (1992). Sedimentology and geomorphology of overbank flows on meandering river floodplains. *Geomorphology*, *4*(6), 367–379. https://doi.org/10.1016/0169-555X(92)90032-J

Chapter 2 Sediment Transport Potential in a Hydraulically Connected River and Floodplain-Channel System

Sumaiya Sumaiya[1], Jonathan A. Czuba[1], John T. Schubert[1,2], Scott R. David[3], Graham H. Johnston[4], and Douglas A. Edmonds[5]

Submitted: 15 September 2020

To: *Water Resources Research*

Status: Published

DOI: https://doi.org/10.1029/2020WR028852

Abstract

Meandering river floodplains often contain intermittently flooded complex channel networks. Many questions remain as to the pervasiveness, function, and evolution of these floodplain channels. In the present work, we analyzed size-specific sediment transport potential and assessed whether the channelized floodplain of the meandering East Fork White River near Seymour, Indiana is on a net erosional or depositional trajectory. We applied a two-dimensional hydrodynamic model and used simulated model results to estimate the largest sediment size that can be moved in suspension and as bedload at various flows for grain size classes between 4 µm and 64 mm. We developed a probabilistic method that integrates the largest sediment size that can be moved at various flows to compute an effective grain size, which we compared to measured field data. Results show that the river is capable of supplying sand to the floodplain and these floodplain channels can transport sand in suspension and gravel as bedload. This suggests that sediment supplied from the river could be transported as bedload in floodplain channels. These floodplain channels are supply

limited under the current hydrologic regime and the grain size distribution of the bed surface is set by the flow conditions; thus, these floodplain channels are net erosional. Finally, our proposed method of probabilistically integrating the largest sediment size that can be moved at various flows can be used to predict the upper end of the grain size distribution in suspension and in bed material, which is applicable to floodplains as well as coastal areas.

Keywords: floodplain channel, floodplain erosion, floodplain deposition, effective sediment size, river-floodplain processes, East Fork White River

Key Points:

1. We investigate the potential of various sizes of sediment to move over a complex topographic floodplain surface at different flows.

2. We compute an effective sediment size moved in suspension and as bedload by integrating the largest sediment size moved for all flows.

3. We compare our effective sediment size with field data and conclude unvegetated floodplain channels are on a net erosional trajectory.

2.1 Introduction

Floodplains are intermittently flooded complex geomorphic features with positive and negative relief (Lewin & Ashworth, 2014). Negative relief consists of meso- and macro-scale elements that include accessory through-channels, tributary channels, channel margin slackwater zones, bar-shelter backwaters, contiguous channel remnants, tie channels, internal drainage channel networks, and large-scale flood basins occluded by channel-belt aggradation (Lewin & Ashworth, 2014). This negative relief is present on both braided (Kleinhans & Berg, 2011; Limaye, 2017; Reinfelds & Nanson, 1993; Schuurman et al., 2013) and meandering (David et al., 2017; Lewin et al., 2017; Park & Latrubesse, 2017; Trigg et al., 2012) river floodplains. At least for meandering river floodplains, high-resolution topographic data reveal that negative relief is often organized into a floodplain-channel network (David et al., 2017; Lewin & Ashworth, 2014). These networks create well-connected river-floodplain systems, and examples include the Amazon River in Brazil (Mertes et al., 1996; Rudorff et al., 2014; Trigg et al., 2012), Medway River in southern Ontario (Thayer & Ashmore, 2016), Ogeechee River in Georgia (Benke et al., 2000), Congaree River in South Carolina (Kupfer et al., 2015; Xu et al., 2020), Copper Creek in Australia (Fagan & Nanson, 2004), Kolymar River in Russia (Lewin & Ashworth, 2014), Sava River in Slovenia (Rak et al., 2016), and White River in Indiana (Czuba et al., 2019; David et al., 2017).

The origin of well-connected river-floodplain systems is not entirely, but certainly due to overbank processes, which contribute to a richness of floodplain topographic forms, including floodplain channels of different sizes and shapes. The pathways through which floodwaters first inundate the floodplain can be focused through breaches, crevasses, and chutes which can actively erode the floodplain proximally and terminate into fan or lobe

shaped crevasse splay deposits distally (Allen, 1965; Bristow et al., 1999; Brown, 1996; Lewin et al., 2017; O'Brien & Wells, 1986; Zwoliński, 1992). Floodplain channels are main conduits through which water and sediment are exchanged between a river and its floodplain (Czuba et al., 2019). During an overbank flood, at least suspended sediment from a river can be transported to the floodplain through these pathways and become deposited or resuspended, resulting in floodplain erosion/deposition depending on the flow conditions and supplied sediment (Zwoliński, 1992). Overall, a combination of overbank transport processes driven by water or wind, including turbulent diffusion and advection, can transport sediment in suspension and as bedload, leading to erosion and deposition and the formation of complex floodplain deposits and associated topography (Allen, 1965; Nanson, 1986; Phillips, 2011; Pizzuto et al., 2008). Floodplain surfaces built by periodic erosion and deposition consist of a range of grain sizes and typically fine with increasing distance from the main channel (Nanson & Croke, 1992; Nicholas & Walling, 1996; Marriott, 1992), however, floodplain topography can complicate this general pattern (Moody et al., 1999; Pizzuto et al., 2008).

Many floodplains described in the literature are formed from sediment deposited through lateral point-bar accretion of sand and/or gravel and vertical overbank deposition of finer sand, silt, and clay (Brown, 1996; Jackson, 1976; Lauer & Parker, 2008; Nanson, 1980; Nanson & Croke, 1992; Nunnally, 1967; Wolman & Leopold, 1957). These types of floodplains are classified as Type B3: meandering river, lateral-migration floodplains (Nanson & Croke, 1992). Lateral point-bar accretion occurs where coarse bed-material sediment progressively deposits on the point bar along the inner bank of a meander bed due to secondary flow circulation within the river (e.g., Dietrich, 1987). Vertical overbank deposition occurs when floods deposit fine-grained suspended sediment on inundated areas adjacent to the channel. Additionally, levee crevasses deposit sandy splays on floodplains and abandoned oxbow lakes progressively fill with fine-grained material (e.g., Brown, 1996).

This process of overbank flow and fine-grained sediment deposition on the floodplain is a necessary condition for sustained dynamic meandering in laboratory experiments (Van Dijk et al., 2013).

Yet despite our understanding of the feedbacks between overbank and in-channel processes, in the context of mathematical modeling, the floodplain has often been characterized as a flat feature adjacent to a river channel (at most with a further conceptualization of an associated levee, point bar, and/or sloping floodplain). The conceptualization of a featureless floodplain arises for reasons of data resolution and the need to simplify model geometry. This simple conceptualization appears in geomorphology (James, 1985; Lauer & Parker, 2008; Lauer & Willenbring, 2010; Nicholas et al., 2006; Pizzuto, 1987; Viparelli et al., 2013) and hydraulic engineering (see review by Knight & Shiono, 1996; Sturm, 2001). As a result, the full complexity of sediment transport dynamics on floodplains cannot be simulated using these simple models. Early attempts had been made at two and three-dimensional modeling of flow and sedimentation patterns over floodplains with variable topography (Bates et al., 1996; Middelkoop & Perk, 1998; Nicholas & Mitchell, 2003; Nicholas & Walling, 1997, 1998; Nicholas & McLelland, 2004). However, at the time, these simulations had been limited by data resolution. High resolution topographic data reveal the complex nature of floodplains (David et al. 2017) and provide the opportunity to study surface processes on floodplains in more detail.

The purpose of this paper is to investigate the potential of various sizes of sediment to move over a low-gradient, complex topographic floodplain surface at different flows. We focused our analysis on the same reach of the unconfined, meandering East Fork White River, Indiana, as described by Czuba et al. (2019). We first refined the 2-D HEC-RAS model of Czuba et al. (2019) and verified that the changes we made still agreed with the model calibration and validation data. We ran the model at 21 flows to simulate depth,

velocity, and shear stress. We then used these simulated hydraulic data to estimate the largest sediment size that can be moved in suspension or as bedload spatially across the river-floodplain at various flows. By probabilistically integrating (based on flow recurrence) the largest sediment size that can be moved for all flows, we were able to compute an effective sediment size moved in suspension and as bedload. Finally, we compared our estimated effective sediment sizes with field data and used these estimates to assess whether this floodplain, and the floodplain channels specifically, are on a net erosional or depositional trajectory.

2.2 Study area

The East Fork White River (EFWR) near Seymour, Indiana (Figure 2.1a, b) meanders through an agricultural floodplain with distinctive floodplain channels (Czuba et al., 2019; David et al., 2017). These floodplain channels are subtle, low-relief features that are difficult to differentiate in the field from general undulating topography. Historically, much of the White River basin (approximately 29,400 km^2 drainage area) was forested, had been cleared during the 1800's, and is currently 56% agriculture, 30% forested, and 11% urban (Crawford et al., 1996; Homer et al., 2015).

Previous work in Indiana has taken advantage of state-wide, high-resolution (1.5 m) lidar data to learn that roughly 40% (by area) of floodplains throughout Indiana have floodplain channels (David et al., 2017). These floodplain channels are present most readily in wide, agricultural floodplains where the adjacent river has high migration rates (David et al., 2017). Additionally, these floodplain channels are a combination of old oxbows and likely more recent channels formed by upstream migrating headcuts connecting many floodplain lows, such as old oxbows and other topographic depressions, into an

interconnected floodplain channel network (David et al., 2017, 2019). Of all the floodplains in Indiana investigated by David et al. (2017), the reach along the EFWR near Seymour had one of the most extensive floodplain channel networks without other factors appearing to influence its pattern, such as strong lateral floodplain slope, major backwater, or anthropogenic structures. In this reach specifically, these floodplain channels are inundated roughly 19 days per year, well before most river channel banks are overtopped (Czuba et al., 2019).

Our study focuses on a reach of the EFWR, which we call our area of interest (AOI, Figure 2.1b), that includes 24.4 km of the meandering river, measures 14.3 km along the floodplain valley centerline, and has a drainage area at its downstream end of roughly 6,000 km^2. The only major tributary that enters the study reach is Sand Creek, with a drainage area of 670 km^2. The slope of the river is roughly 3.2×10-4 m/m and the down-valley slope along the floodplain is roughly 5.5×10-4 m/m. The river channel here is roughly 90 m wide at the top of its banks with a 2.7 km wide floodplain (Figure 2.1b). Within the AOI in Figure 2.1b, the land cover is 76% agriculture (predominantly corn and soybean), 13% forested, 7% open water, and 3% urban (Homer et al., 2015).

For clarity in explaining the results that build from our methodology, we further focus on an approximately 500-m long, river-to-floodplain flowpath (Figure 2.1c). Along this flowpath, stationing 0-216 m is within the river channel, stationing 216 m marks the river-floodplain boundary, and stationing 216-477 m is within the floodplain. Along this flowpath within the floodplain, there are two distinct floodplain channels: the floodplain channel at stationing 216-387 m connects the river to the floodplain channel network and flows perpendicular to the down-valley direction and the floodplain channel at stationing 387-477 m is a major segment of the floodplain channel network that conveys water that has largely entered the floodplain from farther upstream and flows parallel to the down-valley direction.

This specific flowpath was selected because it is a location we were able to easily and safely return to during high flow because of nearby road access to collect various field data. The image (Figure 2.1d) of the flowpath (in Figure 2.1c) was taken during data collection on 2 May 2017. Prior to data collection, on 30 April 2017, the flow at a nearby USGS gage (03365500 East Fork White River at Seymour, Indiana; approximately 5.7 km along the channel centerline downstream from the AOI) peaked at 481 m^3/s. The flow then receded to 334 m^3/s on 1 May 2017 and 307 m^3/s on 2 May. A corresponding model simulation at 454 m^3/s (simulated depth in blue, Figure 2.1c), which best matches the water-surface elevations measured in the floodplain (see Czuba et al., 2019 for discussion), shows the same amount floodplain inundation for comparison (Figure 2.1d).

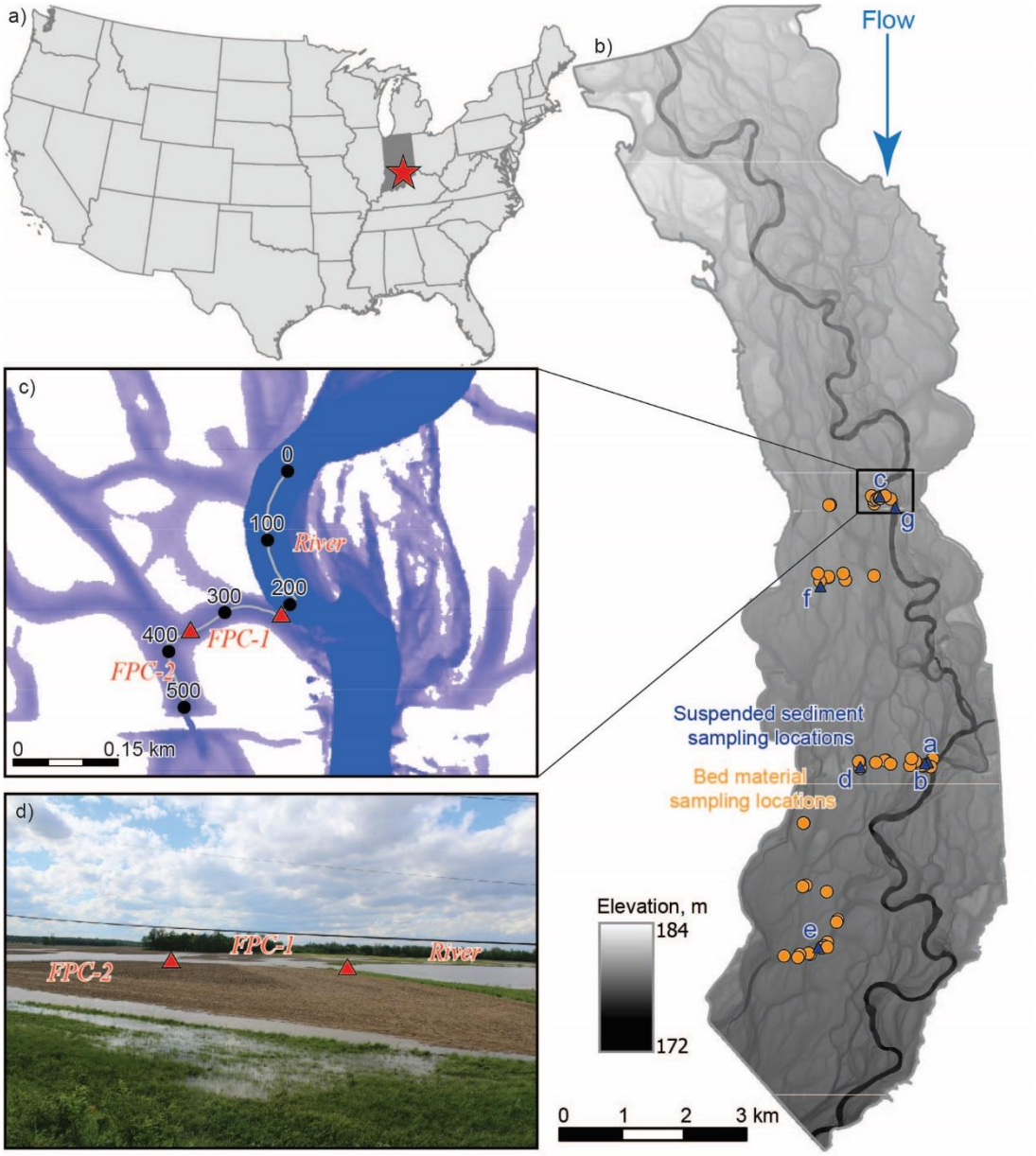

Figure 2.1 Study area of the East Fork White River (EFWR) near Seymour, Indiana (39° 5' 11" N, 85° 51' 42" W). (a) Red star represents the location of the EFWR in Indiana, USA. (b) Elevation of the river-floodplain system within an area of interest (AOI) prepared from the lidar data collected on 23 March 2011. Orange circles represent bed material sampling locations (47 total) and blue triangles represent suspended sediment sampling locations (8 total, labeled a-g; 1 not shown, labeled 'h', located farther downstream). Black rectangular box indicates the highlighted flowpath location within the AOI. (c) Highlighted 500-m long flowpath with stationing (black circles) starting at 0 farthest upstream in the river. Red

triangles represent the break points among the river and floodplain channels (FPC-1 and FPC-2). Blue area shows simulated inundated extent with darker blues corresponding to deeper depths; 454 m^3/s. (d) Picture of the flowpath taken on 2 May 2017 that corresponds to the simulated flood extent in (c).

2.3 Methods

2.3.1 Model development, calibration, validation, and simulations

We refined the 2-D HEC-RAS model (using version 5.0.5) for the EFWR of Czuba et al. (2019) in order to ensure the most accurate estimates of velocity and shear stress in floodplain channels. The full details describing the underlying data used to generate the terrain surface from 1.5-m lidar topography and surveyed river bathymetry, and data used in model calibration and validation can be found in Czuba et al. (2019). Here we only focus on the details we have changed in the model.

We refined the computational grid by adding additional breaklines with a nominal cell spacing of 3 m along the center of all major floodplain channels. In the Czuba et al. (2019) model (what we refer to as the original model), the nominal orthogonal cell spacing for the entire model domain was 15 m, with added breaklines refining the grid along the river channel centerline and banks to 12 m and along selected major floodplain channels and roadways to 3 m. The major improvement for the refined model used here is that some floodplain channels in the original model that had a nominal cell spacing of 15 m were now refined to 3 m. The locations of this refinement (where we added breaklines) traced the centerline of all floodplain channels that were inundated at a 1.2-month recurrence interval flow (382 m^3/s) when the major low-lying floodplain channels become inundated (Czuba et

al., 2019). The refined computational mesh added over 163,000 new cells with a new total of 748,000 cells.

In the refined model, we maintained the original calibrated Manning's n-values. We compared model simulated and measured water-surface elevations (WSELs) and velocities for model validation. In the refined model, root-mean-square error (RMSE) and mean absolute error (MAE) was the same as the original Czuba et al. (2019) model. This suggests that our slight refinement of the model grid did not significantly affect water-surface elevations and velocities in the vicinity of our calibration and validation measurements partly because those floodplain channels had refined grids in the original model.

Model simulations were performed for the same 21 steady-state flow conditions as in Czuba et al. (2019). These flow conditions are referenced to the daily mean flow data at the USGS gage (03365500 East Fork White River at Seymour, Indiana) for water years 1928–2019. From the model, we exported simulated depth, velocity, and bed shear stress for subsequent sediment transport analysis.

2.3.2 Analytical methods

The simulated hydraulic data were used to estimate the largest (sediment particle) size that can be moved (LSM) in suspension or as bedload spatially across the river-floodplain at various flows. To find the LSM in suspension and as bedload we applied a Rouse number and a Shields stress mobility criterion, respectively. Simulated bed shear stresses were used to calculate Rouse number (Z_R) and Shields stress (τ^*)for a wide range of expected sediment size classes transported in suspension and as bedload, 15 sizes in phi increments between 4 µm (very fine silt) and 64 mm (very coarse gravel; Garcia, 2008).

The LSM in suspension was computed by comparing the Rouse number (Z_R) for a range of sediment sizes with a criterion for suspension. The Rouse number (Garcia, 2008) was calculated as

$$Z_R = \frac{w_s}{\kappa u_*} \tag{1}$$

where κ is von Karman's constant (0.41), u_* is the shear velocity (m/s), and w_s is the sediment fall velocity (m/s), which is a function of particle diameter. We computed shear velocity (u_*) from simulated bed shear stress as

$$u_* = \sqrt{\frac{\tau_b}{\rho}} \tag{2}$$

where τ_b is the simulated bed shear stress (Pa) at each grid cell and ρ is the density of water (1000 kg/m^3). Sediment fall velocity was calculated using the Ferguson & Church (2004) equation as

$$w_s = \frac{RgD^2}{C_1 \upsilon + \sqrt{0.75\, C_2 RgD^3}} \tag{3}$$

where R is the submerged specific gravity (1.65), g is the gravitational acceleration (9.81 m/s^2), D is the sediment particle diameter using all 15 values in the range from 4 µm to 64 mm, υ is the kinematic viscosity of water (1×10-6 m^2/s), C_1 is a constant with a theoretical value of 18, and C_2 is a constant representing the asymptotic value of the drag coefficient (C_2 = 1 for natural grains).

For each grid cell at each flow (a single value of bed shear stress), we computed a Rouse number for each of our 15 sediment sizes. The Rouse number is a function of particle fall velocity and shear velocity. The threshold condition for a particle to remain in suspension is when the tendency for a particle to settle out of suspension (fall velocity) is balanced by turbulence acting to keep that particle in suspension (shear velocity). That is, when the fall

velocity is equal to the shear velocity or, equivalently, when the Rouse number is equal to 2.43 ($1/\kappa$), which is the threshold value for a particle to remain in suspension (Engelund, 1965a,b; Van Rijn, 1984; Niño, 1995; Niño & García, 1998; Niño et al., 2003). Therefore, the LSM in suspension was the largest sediment size (from the range of sediment sizes) for which Z_R < 2.43. Note that because the shear velocity is in the denominator and fall velocity is in the numerator of Equation (1), smaller values of Rouse number indicate a greater potential for suspension.

The LSM as bedload was computed by comparing Shields stress (τ^*) with critical Shields stress (τ_c^*) for a range of sediment sizes. At each flow, Shields stress (τ^*) was calculated as

$$\tau^* = \frac{\tau_b}{\rho g R D} \tag{4}$$

where τ_b is the simulated bed shear stress at each grid cell (Pa), ρ is the density of water (1000 kg/m^3), g is the gravitational acceleration (9.81 m/s^2), R is the dimensionless submerged specific gravity of a sediment particle (1.65), and D is the sediment particle diameter using all 15 values in the range from 4 µm to 64 mm. Critical Shields stress (τ_c^*) was calculated for each sediment size as (Brownlie, 1981; Garcia, 2008)

$$\tau_c^* = \frac{1}{2}\left[0.22\, R_{ep}^{-0.6} + 0.06\, exp\left(-17.77\, R_{ep}^{-0.6}\right)\right] \tag{5}$$

where R_{ep} is the particle Reynolds number expressed as

$$R_{ep} = \frac{\sqrt{gRD}\, D}{\upsilon} \tag{6}$$

For each grid cell at each flow (a single value of bed shear stress), we computed a Shields stress and an associated critical Shields stress for each of our 15 sediment sizes. At locations where calculated $\tau^* > \tau_c^*$, that sediment size can be transported. Therefore, the LSM as bedload was the largest sediment size (from the range of sediment sizes) for which $\tau^* > \tau_c^*$.

The LSM at all flows was probabilistically integrated (based on flow recurrence) to compute an effective sediment size that can be moved in suspension and as bedload. This effective sediment size is similar to the idea of "effective discharge" proposed by Wolman & Miller (1960), where instead of integrating over flow magnitude and frequency (in the case of effective discharge), we replace flow magnitude with LSM. We call this effective grain size the Probabilistic Flow Integrated Grain Size (PFIGS) and calculate it as

$$\text{PFIGS} = \sum_i LSM_i \, P_i \tag{7}$$

where LSM_i is the LSM at the ith flow and P_i is the probability of occurrence of the ith flow. The integration (summation in this discrete case) is over all i flows that inundate each grid cell and the probabilities must first be normalized at each grid cell such that $\sum P_i = 1$. For the 21 simulated flows for the EFWR, the 12th flow (382 m^3/s, 1.2-month r.i.) is the flow when the majority of low-lying floodplain channels first become inundated and fully connected. The flow at which each grid cell is first inundated is shown in Figure 2.2 and the integration for computing PFIGS at each grid cell only occurs at the flows at and above those shown in Figure 2.2. Therefore, our integration of LSM to calculate PFIGS was over 10 flow conditions (flows 12-21) or less.

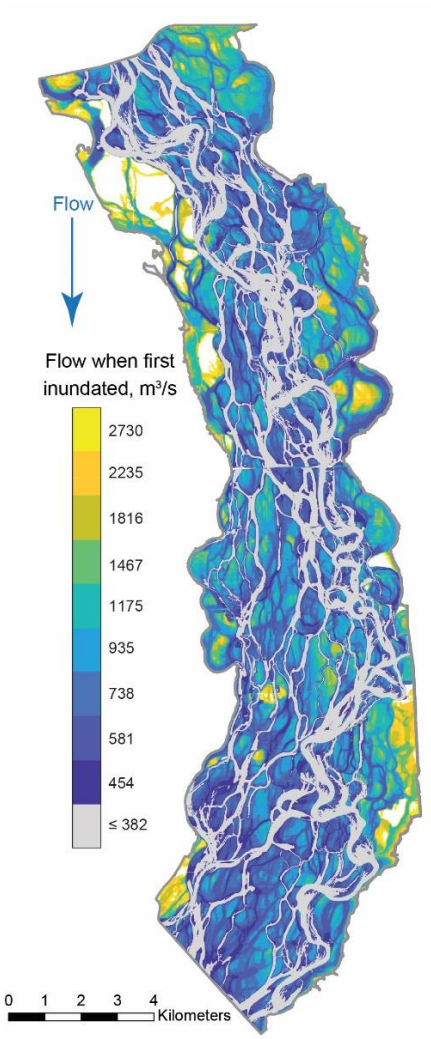

Figure 2.2. Flow at which the floodplain first becomes inundated. The area in light gray are those areas inundated at or below 382 m^3/s (1.2-month recurrence interval).

2.3.3 Sediment data

Suspended sediment was collected as single vertical samples from 6 locations in flowing floodplain channels and 2 locations in the river at bridges on 1-2 May 2017 using a DH-76 depth-integrating suspended hand-line sampler with 1-L plastic bottles or handheld DH-48 depth integrating sampler with 0.5-L bottles. At each location, 3-5 bottles of water and suspended sediment were collected by slowly lowering the sampler through the water

column with a transit rate that collected a sufficient sample without overfilling the bottle (Edwards & Glysson, 1999). Suspended sediment concentration was determined using the evaporation method described in the ASTM International Test Method, D 3977 – 97(B) (see also Guy, 1969) and samples were composited to determine the particle size distribution with a Malvern Mastersizer® 3000E laser diffraction instrument.

Bed material was collected from the floodplain surface (44 locations) and a river bar (3 locations) on 12 August 2019. Floodplain samples were collected using a steel ring (4.76 cm diameter × 5.08 cm height) pounded into the surface to retrieve a 90 cm^3 sample of sediment (roughly 120 g of sediment per sample). Samples from the river bar were collected using a metal trowel to scoop up the top few centimeters of sediment over a local area large enough to fill a gallon-sized plastic bag (roughly 5.6 kg of sediment per sample). In the lab, all sediment samples were air dried. Floodplain sediment samples were additionally placed in a furnace at 400°C for a minimum of 4 hours to incinerate any organics. Then all samples were sieved using sieves in phi-size gradations (Garcia, 2008) down to 62.5 µm to determine a particle size distribution.

Suspended sediment concentration (SSC) and some grain size information (percent finer than 62.5 µm) was downloaded from the USGS gage (03365500 East Fork White River at Seymour, Indiana; USGS, 2020). These data were collected between 1964 and 1981, following established USGS procedures for sediment data collection described in Edwards & Glysson (1999). The largest discharge for which SSC was measured was around 1,000 m^3/s, which has almost a 2-year recurrence interval. Each sample was marked as being on the rising or falling limb of the hydrograph and the season in which, it was collected: Spring (March-May), Summer (June-August), Fall (September-November), and Winter (December-February). The only major difference between the methods used to collect our suspended sediment data and the USGS's data was that we collected suspended sediment from a single

vertical location in each floodplain channel or river channel, whereas the USGS data were a composite of several verticals across the river channel.

2.3.4 Error estimation

Errors of the predicted sediment sizes were calculated using mean absolute error (MAE), root mean square error (RMSE), normalized mean absolute error (NMAE), normalized root mean square error (NRMSE), and relative root mean square error (RRMSE) methods. The MAE method calculates the average of individual differences and RMSE method estimates average magnitude of the error. The NMAE and NRMSE are calculated by dividing the MAE and RMSE by the average of the observed value, respectively. The equation for the RRMSE (Despotovic, et al., 2016) is

$$RRMSE = \sqrt{\frac{1}{n}\sum_{i=1}^{n}\frac{(y_i - x_i)^2}{(y_i)^2}} \times 100 \qquad (8)$$

where y_i is the observed value and x_i is the predicted value.

2.4 Results

2.4.1 Simulated depth and shear stresses

We highlight results at three important flow conditions for the EFWR: (high-frequency flood) at a 1.2-month recurrence interval flow (382 m^3/s), where the majority of the floodplain channels become inundated and convey roughly 25% of the total flow (Figure 2.3a); (intermediate-frequency flood) at an 8.6-month recurrence interval flow (935 m^3/s),

where the floodplain is mostly inundated and conveys roughly 50% of the total flow (Figure 2.3b); and (low-frequency flood) at the peak flow of the 92-year USGS gaging record (2,730 m^3/s), where the floodplain is fully inundated and conveys roughly 75% of the total flow (Figure 2.3c; floodplain conveyance percentages from Czuba et al., 2019).

Inundation depth increases with increasing flow, with the deepest depths on the floodplain in floodplain channels (Figure 2.3a-c). Bed shear stress increases with increasing flow and increasing depth (Figure 2.3e-f). For the high-frequency flood, floodplain channels only first become inundated and begin conveying flow with low bed shear stress compared to the river (Figure 2.3d). Between these floodplain channels are floodplain islands (Figure 2.3a and d), which are areas of relatively higher floodplain elevation that are inundated less frequently. For the intermediate-frequency flood, bed shear stress increases further in floodplain channels and is low on previous floodplain islands that are now inundated (Figure 2.3e). Many locations with locally high bed shear stress (small red patches, Figure 2.3e) are where flow in a floodplain channel overtops a farm road. For the low-frequency flood, bed shear stress in major floodplain channels and at floodplain valley constrictions is similar to the river channel (Figure 2.3f).

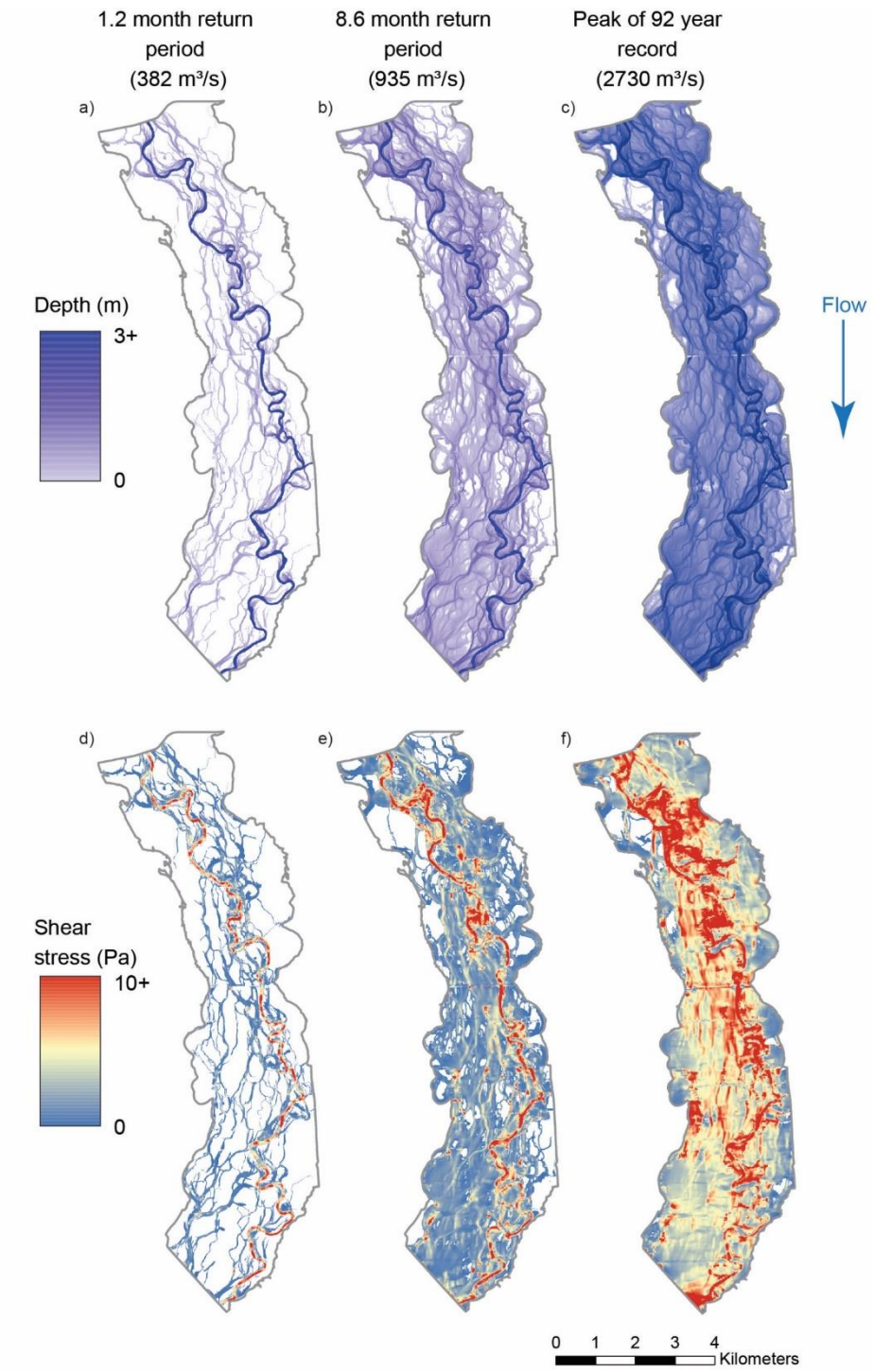

Figure 2.3. Simulated (a, b, c) depth and (d, e, f) bed shear stress for the high-frequency (a, d; 382 m^3/s), intermediate-frequency (b, e; 935 m^3/s) and low-frequency (c, f; 2,730 m^3/s) floods. The river channel can be seen as the darkest blue meandering line in (a).

2.4.2 LSM in suspension and as bedload

LSM in suspension and LSM as bedload were calculated and will be described for the entire AOI. But first, we describe our results along a flowpath from the river and into two different floodplain channels as a detailed example demonstrating our calculations. Rouse numbers along the flowpath (one curve for each sediment size at each flow) are spatially and temporally variable (Figure 2.4a-c). Rouse numbers substantially decrease transitioning from the river to FPC-1 for the high-frequency flood (Figure 2.4a), but are roughly constant for the low-frequency flood (Figure 2.4c). The sediment size corresponding to the curve just above the threshold line in Figure 2.4a-c corresponds to the LSM in suspension (Figures 4d-f).

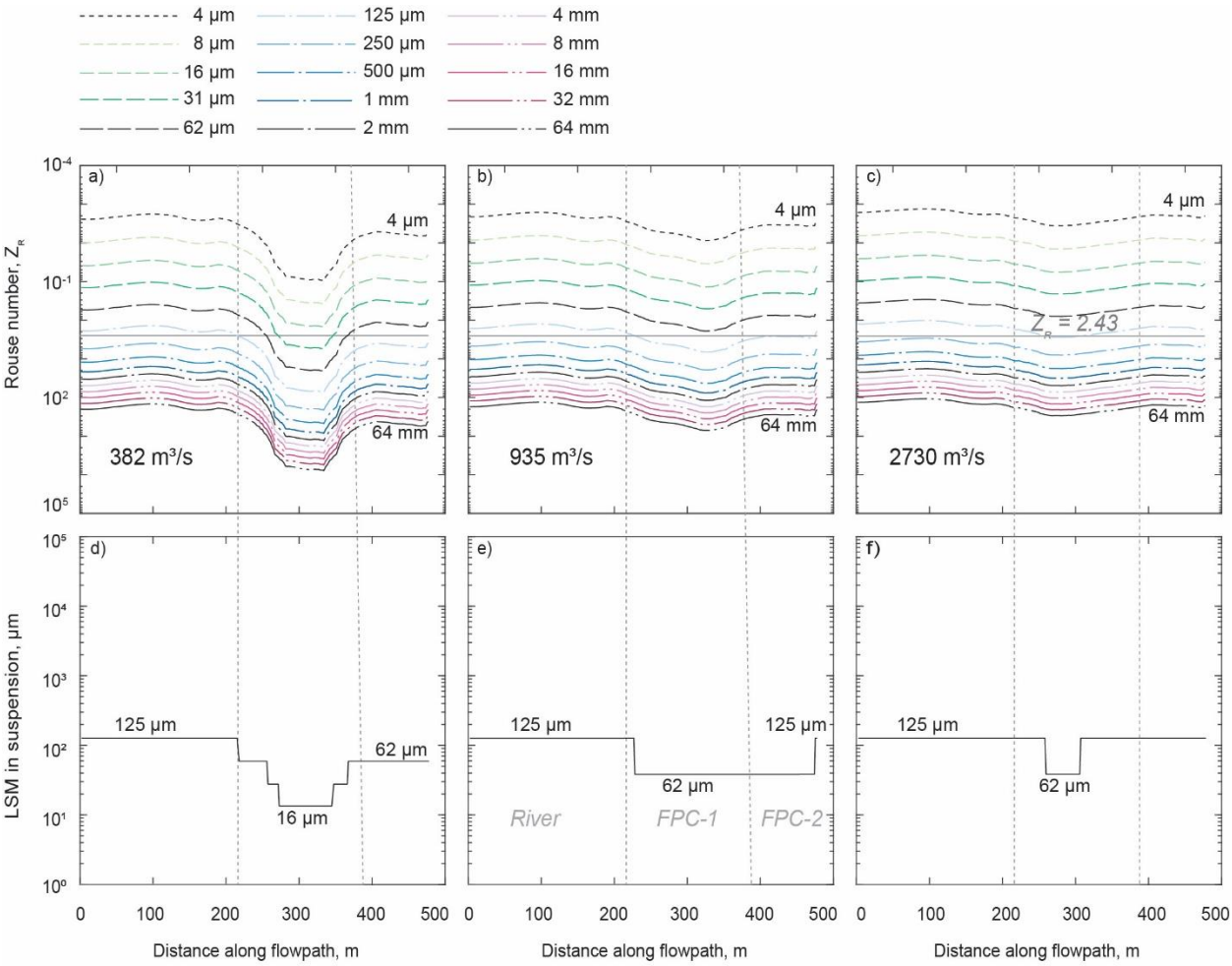

Figure 2.4. Largest size that can be moved (LSM) in suspension at three flows along the flowpath. Curved dashed lines trace the Rouse number along the flowpath (Figure 2.1c) for 15 sediment sizes for the (a) high-frequency (382 m^3/s), (b) intermediate-frequency (935 m^3/s), and (c) low-frequency (2,730 m^3/s) floods. Solid horizontal lines represent the Rouse number suspension threshold (Z_R = 2.43). Curved dashed lines above the solid line represent sediment sizes moved in suspension (Z_R < 2.43; note the y-axis is inverted). Vertical dashed lines show the break points among the river and floodplain channels (FPC-1 and FPC-2). FPC-1 is oriented transverse to the river and FPC-2 is oriented parallel to the river. Solid lines denote the LSM (µm) in suspension along the flowpath for the (d) high-frequency, (e) intermediate-frequency, and (f) low-frequency floods.

The LSM in suspension increases with increasing flow in floodplain channels but remains constant at 125 µm in the river channel (Figure 2.4d-f). This is likely because the high-frequency flood is still a relatively high flow in the river channel where increases in flow progressively spill across larger extents of the floodplain and do not contribute to large increases in shear stresses in the river channel (McKean and Tonina, 2013). In FPC-1, the substantial decrease in Rouse number for the high-frequency flood results in an LSM in suspension of only 16 µm whereas in FPC-2 the LSM increases to a constant 62 µm (Figure 2.4d). As flow increases, the LSM in suspension in the floodplain channels progressively increases, nearly to the same value as in the river (125 µm) for the low-frequency flood (Figure 2.4e and f). This indicates that there is a potential for the sediment in suspension in the river (finer than 125 µm) to enter FPC-1 for the low-frequency flood and subsequently fall out of suspension (coarser than 16 µm for the low-frequency flood and 62 µm for the intermediate-frequency and low-frequency floods; Figure 2.4d-f). However, for the low-frequency flood, there is the greatest potential for any sediment supplied by the river to be

carried in suspension across the floodplain (LSM in suspension in floodplain nearly a constant 125 µm; Figure 2.4f).

Compared to the Rouse number (Figure 2.4a-c), Shields stress along the flowpath has more pronounced undulations (Figure 2.5a-c). For the high-frequency flood, Shields stress is highest in the river channel, and decreases substantially in FPC-1 before increasing in FPC-2 (Figure 2.5a). As flow increases, Shields stress becomes more uniform across the river channel, FPC-1, and FPC-2 (Figure 2.5a-c). The sediment size corresponding to the Shields stress curve just above its critical Shields stress threshold line in Figure 2.5a-c is the LSM as bedload (Figures 5d-f).

For the high-frequency flood, the river can move medium gravel (8-16 mm) as bedload, whereas FPC-1 can only move 2 µm as bedload (the lowest size considered) and FPC-2 can move up to 2 mm as bedload (Figure 2.5d). In FPC-1 at this same flow, the LSM in suspension is fine silt (16 µm; Figure 2.4d). The LSM in suspension in FPC-1 (Figure 2.4) is larger than the LSM as bedload in FPC-1 (Figure 2.5) because our formulation does not account for entrainment of fine sediment from the bed (Lamb & Venditti, 2016; Nino et al., 2003; Van Rijn, 1984), but rather focuses on whether sediments already in suspension will settle out (i.e., where would sediments already suspended in the river settle out once they enter the floodplain). For this high-frequency flood, FPC-1 is likely depositional because the LSM in suspension is much higher than the LSM as bedload. Coarse gravel (16-32 mm) can move in the river for the intermediate-frequency and low-frequency floods, whereas very coarse sand (1 mm) and fine gravel (4 mm) can move in FPC-1 and fine gravel (4-8 mm) and coarse gravel (16 mm) can move in FPC-2 for the intermediate-frequency and low-frequency floods, respectively (Figure 2.5e and f).

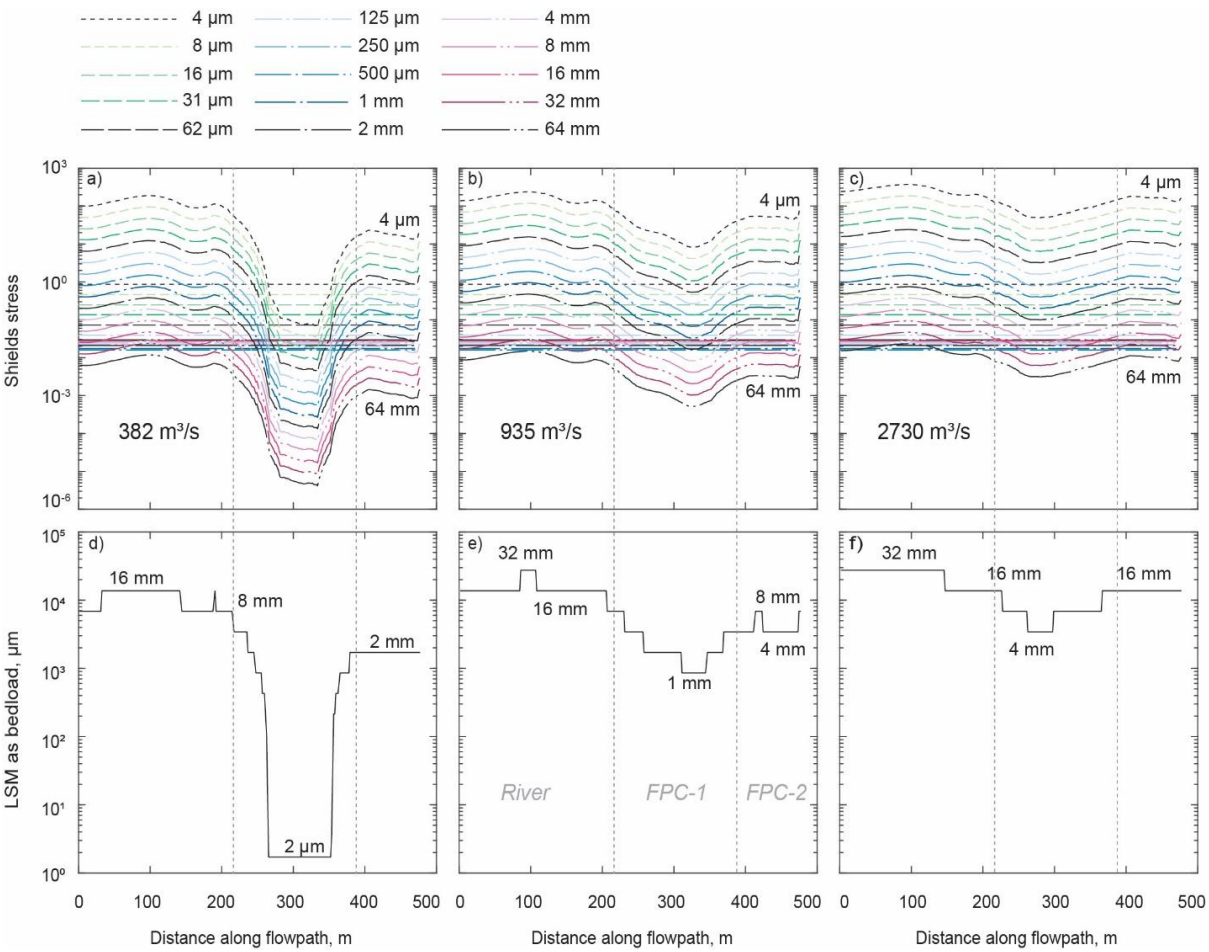

Figure 2.5. Largest size that can be moved (LSM) as bedload at three flows along the flowpath. Shields stress (τ^*, curved dashed lines) and corresponding critical Shields stress (τ_c^*, horizonal dashed lines) along the flowpath (Figure 2.1c) for 15 sediment sizes for the (a) high-frequency (382 m^3/s), (b) intermediate-frequency (935 m^3/s), and (c) low-frequency (2,730 m^3/s) floods. Curved dashed lines above their corresponding horizontal dashed line represent sediment sizes moved at least as bedload ($\tau^* > \tau_c^*$). Vertical dashed lines show the break points among the river and floodplain channels (FPC-1 and FPC-2). Solid lines denote the LSM (µm) as bedload along the flowpath at (d) high-frequency, (e) intermediate-frequency, and (f) low-frequency floods.

An LSM was calculated at each grid cell of the AOI, which represents the largest sediment particle size that can be moved in suspension or as bedload in a specific location at a specific flow. The largest of all values spatially across the AOI of LSM in suspension for the high-frequency and intermediate-frequency floods in the river channel is fine sand (125 µm). However, the largest of all values of the LSM for the low-frequency flood in the river channel and across the floodplain at all simulated discharges was medium sand (250 µm) (Figure 2.6a-c). The most common LSM in suspension (based on largest percentage of area) for both river and floodplain for the high-frequency and intermediate-frequency floods was very fine sand (62 µm) (Figure 2.6a and b). Very fine sand (62 µm) could be transported in suspension in 73% and 92% of the wetted floodplain area and 66% and 94% of the river area for the high-frequency and intermediate-frequency floods, respectively. For the low-frequency flood, the most common sediment size in suspension was fine sand (125 µm), which could be transported in 74% of the wetted floodplain area and 77% of the river area. This shows, consistent with the findings from Figure 2.4, that the LSM in suspension is greater in the river than floodplain for the high-frequency flood and as flow increases, the LSM in suspension in the river and floodplain is similar.

The largest of all values spatially across the AOI of LSM as bedload for all three flows was very coarse gravel (32 mm), however, the area of the river-floodplain that can move this size particle is very small. The most common LSM as bedload (based on largest percentage of area) for both the river and floodplain for the high-frequency, intermediate-frequency, and low-frequency floods are 2 mm, 4 mm, and 8 mm, respectively. These LSM can be transported as bedload in 54% of river and 64% of floodplain areas (2 mm) for the high-frequency flood, 56% of river and 62% of floodplain areas (4 mm) for the intermediate-frequency flood, and 82% of river and 78% of floodplain areas (8 mm) for the low-frequency flood (Figure 2.6d-f). Some discrete patches of the floodplain can transport larger particles

(32-64 mm) than in the river channel because of locally high bed shear stresses (Figure 2.3) where flow in floodplain channels overtops farm roads. At these locations, we have found angular gravel (~2 cm diameter) washed from farm roads downstream into floodplain channels.

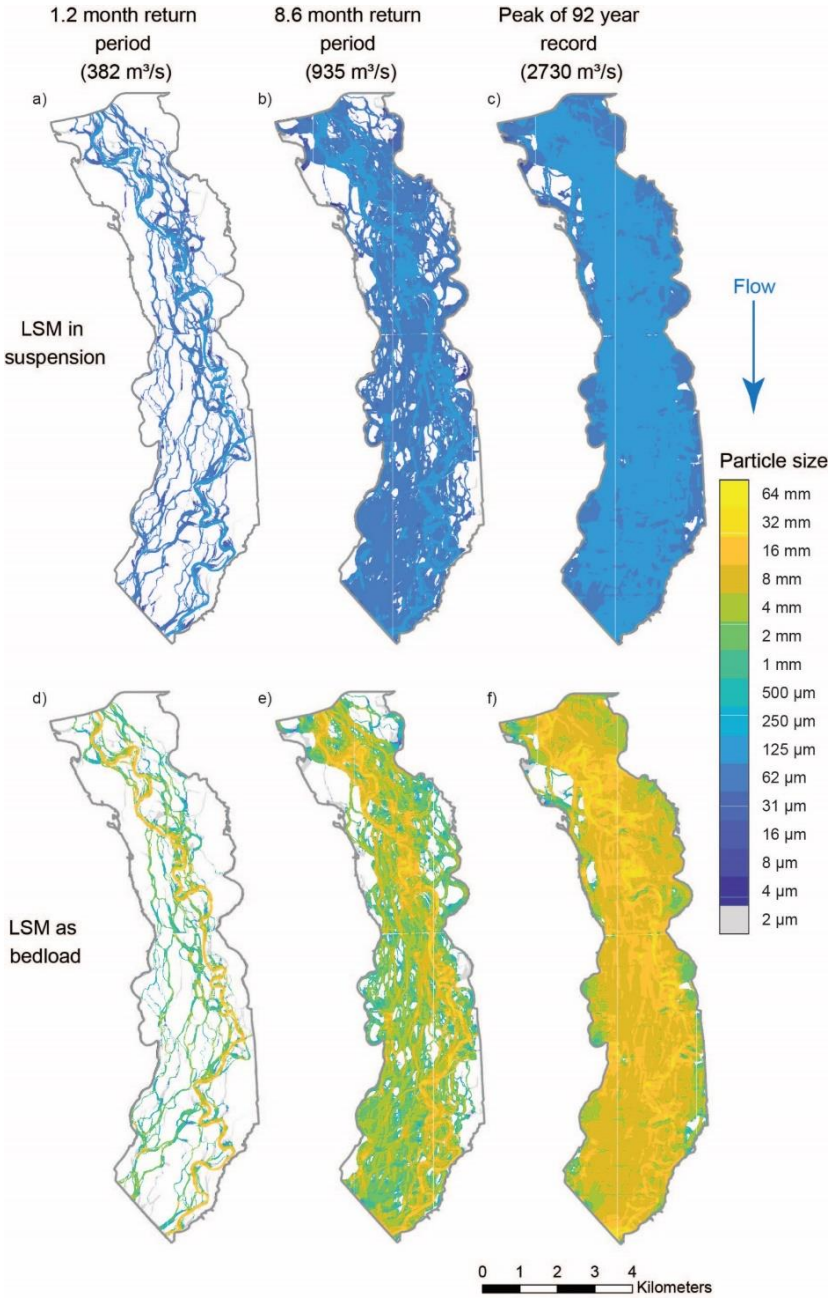

Figure 2.6. Largest size that can be moved (LSM) in suspension (a-c) and as bedload (d-f) within an area of interest (AOI) for the high-frequency (a, d; 382 m^3/s), intermediate-frequency (b, e; 935 m^3/s), and low-frequency (c, f; 2,730 m^3/s) floods.

We have further summarized the data in Figure 2.6 as percentiles of LSM (25th, 50th, and 75th) in suspension in the river and as bedload on the floodplain (Figure 2.7). These summary statistics represent characteristics of the spatial distribution of LSM at each flow. We focus on suspended sediment in the river because those grains are supplied to the floodplain and bedload in the floodplain because that limits that largest size transported across the floodplain. At the lowest flows considered, the 25th percentile LSM as bedload on the floodplain is 2 µm and lower than that for suspended sediment (Figure 2.7, see also previous discussion of FPC-1 in the context of Figures 4-5: section 4.2, paragraph 4). These are locations where segments of floodplain channels are wet, likely from backwater, but are not conveying flow. These locations can be seen in Figure 2.6 when comparing the gray segments of floodplain channels in Figure 2.6d with corresponding locations in Figure 2.6a that are blue. For the high-frequency and intermediate-frequency floods, the LSM in suspension in the river is nearly constant at 62 µm, increasing to 125 µm only at the highest flows (Figure 2.7). In comparison, the 50th percentile LSM as bedload on the floodplain increases by nearly an order of magnitude, from 1 to 8 mm (Figure 2.7). These data clearly show that the EFWR is capable of suspending and supplying sediment as coarse as sand to the floodplain, but the floodplain, in general, and floodplain channels, specifically, have the capacity to transport gravel (Figure 2.7).

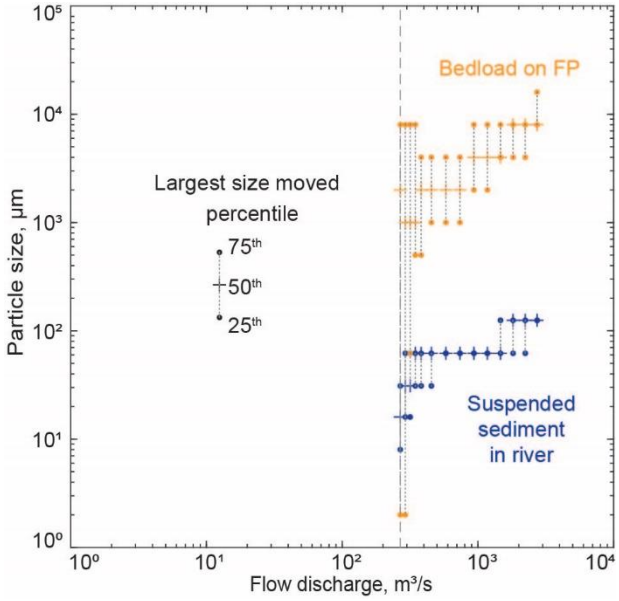

Figure 2.7. Percentiles (25th, 50th, 75th) of LSM (µm) in suspension in the river (blue) and as bedload on the floodplain (orange). These summary statistics represent characteristics of the spatial distribution of LSM at each flow. Dashed line represents the activation of floodplain channels.

2.4.3 Effective grain size or Probabilistic Flow Integrated Grain Size (PFIGS)

From our LSM analysis, larger particles could be transported over large areas during low-frequency floods and smaller particles could be transported over small areas during high-frequency floods. Therefore, to probabilistically integrate the LSM into an effective grain size, we developed and computed the PFIGS (Equation 7), which synthesizes the collection of LSM results at each flow into a single grain size that is most likely to play a key role in river-floodplain morphodynamics. In subsequent sections, we show that PFIGS is predictive of the D97 in suspension and D98 of bed surface material (characteristic of the largest sizes transported), and how together with field data can be used to assess net depositional vs. erosional trajectory. The most common PFIGS in suspension (based on largest percentage of

area) in the river is fine sand (125-250 µm), in floodplain channels and in remaining areas of the floodplain is very fine sand (62-125µm; Figure 2.8a). These sediment sizes could be transported, by area, in 80% of the river (125-250 µm), in 70% of floodplain channels (62-125 µm), and across 62% of remaining areas of the floodplain (62-125 µm; Figure 2.8a). The 50th and 90th percentile (spatially) PFIGS in suspension in the river is 81 µm and 115 µm, in the floodplain channel is 38 µm and 58 µm, and across the entire floodplain is 36 µm and 57 µm, respectively. The most common PFIGS as bedload (based on largest percentage of area) in the river is coarse gravel (16-32 mm) and in floodplain channels and in remaining areas of the floodplain is very fine gravel (2-4 mm; Figure 2.8b). These sediment sizes could be transported, by area, in 48% of the river (16-32 mm), in 83% of floodplain channels (2-4 mm), and across 59% of remaining areas of the floodplain (2-4 mm; Figure 2.8b). The 50th and 90th percentile (spatially) PFIGS as bedload in the river is 8 mm and 15 mm, in the floodplain channels is 1.7 mm and 4 mm, and across the entire floodplain is 1 mm and 2.8 mm, respectively.

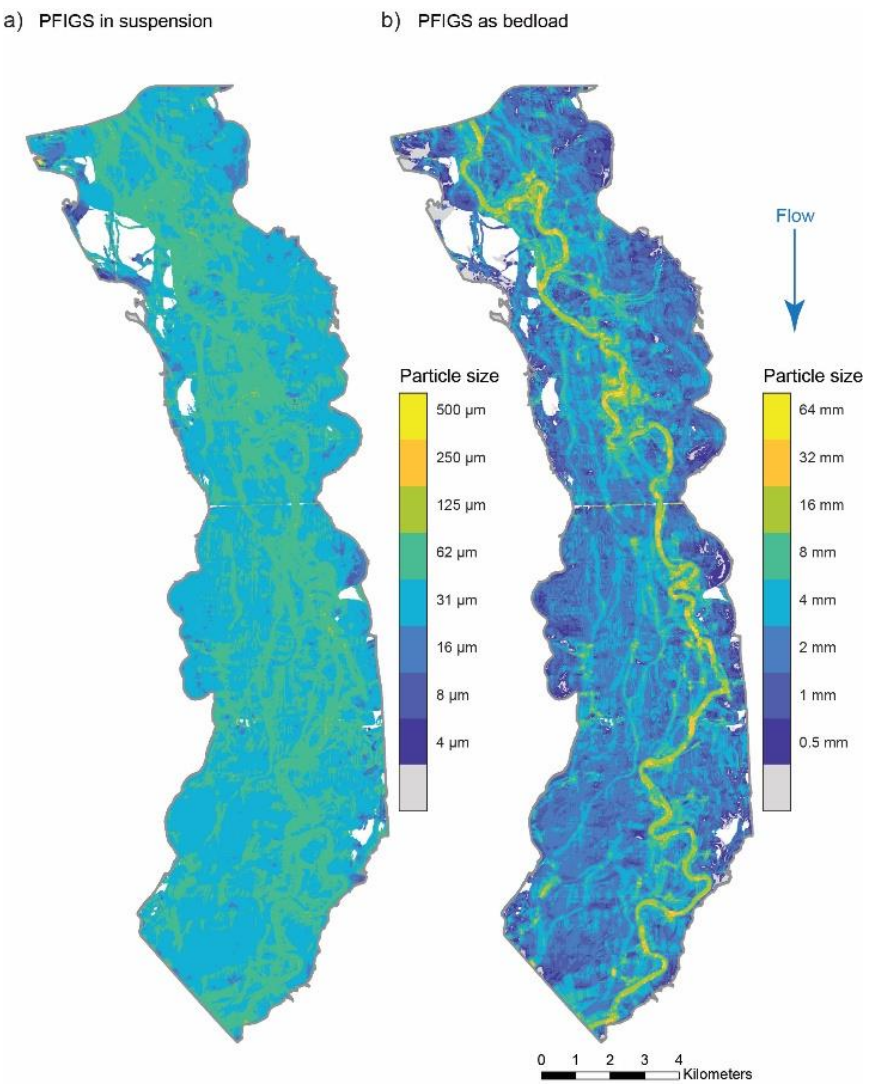

Figure 2.8. Effective sediment size or Probabilistic Flow Integrated Grain Size (PFIGS) in suspension (a) and as bedload (b) within the area of interest (AOI). Note panels (a) and (b) have different color bar scales.

2.4.4 Measured suspended sediment data

Measured SSC, at a flow of approximately 454 m^3/s, was highest in the river (368 mg/L), decreased in floodplain channels proximal to the river (~100 mg/L), and decreased further in floodplain channels distal to the river (62-69 mg/L; Figure 2.9a). At this flow (454 m^3/s), fine silt (11.2 µm) had the highest relative frequency (mode) in the river, very fine silt

(6.83 µm) in proximal floodplain channels, and coarse clay (3.75 µm) in the distal floodplain channels (zonal averages from Figure 2.9b). The measured D50 in suspension also decreased with increasing distance from the main channel; river: 16 µm (medium silt), floodplain channels proximal: 6.3 µm (very fine silt), and floodplain channels distal: 5.3 µm (very fine silt; Figure 2.9c). The sampling flow (454 m^3/s) is just above the high-frequency flood (382 m^3/s) and major floodplain channels are inundated at this flow. The decrease in SSC and suspended sediment size when comparing samples taken proximal to the river (a, b, c) with those farther into the floodplain (d, e, f), suggests that sediment is falling out of suspension from the river to distal floodplain channels.

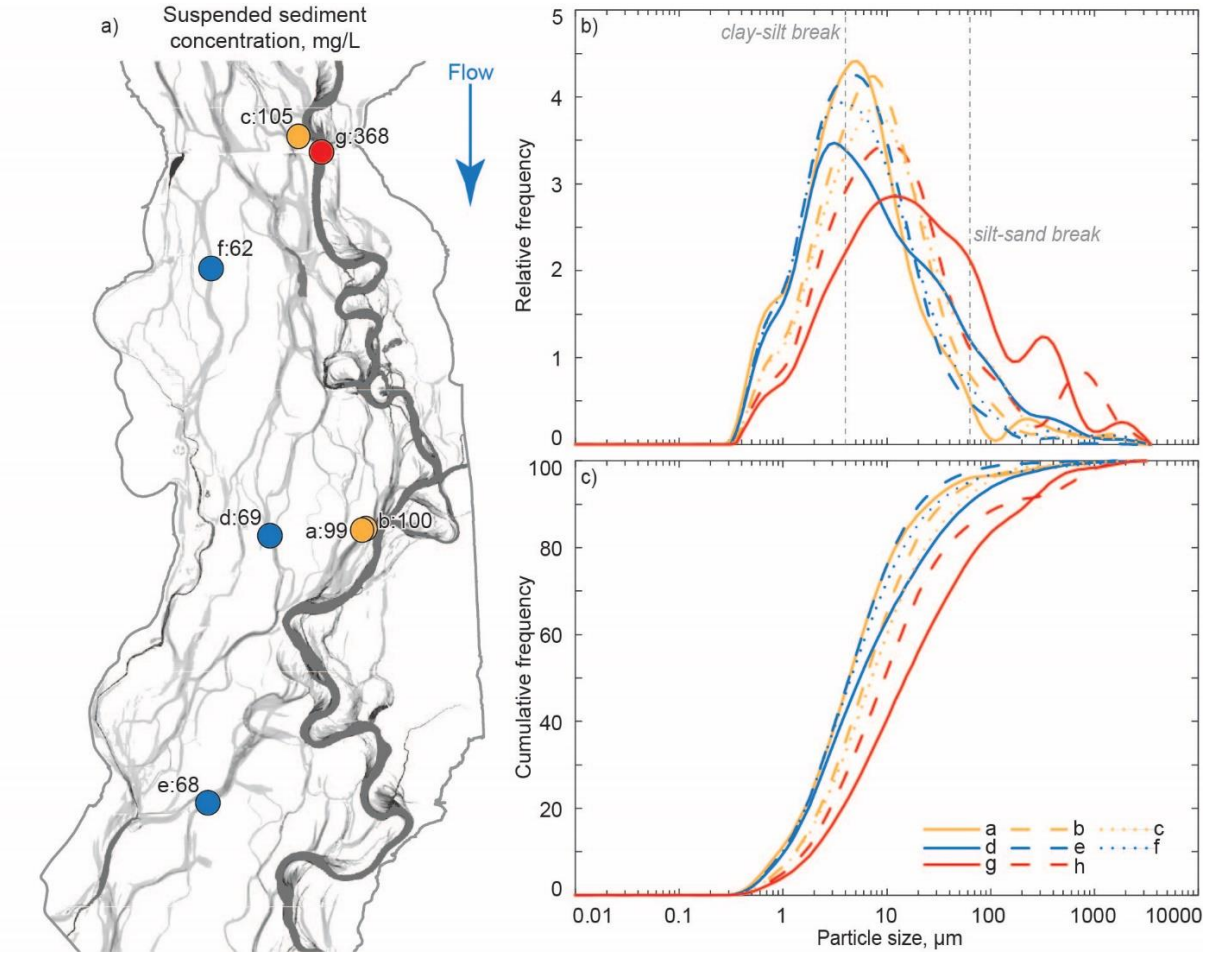

Figure 2.9. Measured suspended sediment in the East Fork White River and its floodplain, in Indiana at eight sampling locations collected on 1-2 May 2017. Red, orange, and blue colors

represent the sampling locations in the river, in floodplain channels proximal to the river, and in floodplain channels distal to the river, respectively. (a) Suspended sediment concentration (mg/L) at seven locations (one location, 'h', is farther downstream). The grey colors are model simulated depths at the approximate conditions (454 m^3/s) when the data were collected. (b) Size distribution of suspended sediment (µm). First dashed line is the clay-silt break (4 µm) and second dashed line is the silt-sand break (62.5 µm). (c) Cumulative particle size distribution of suspended sediment (µm).

Suspended sediment characteristics measured in the river at the USGS gage are shown in Figure 2.10. The variability in SSC decreases at a flow of 268 m^3/s (Figure 2.10a), which is when the most low-lying floodplain channels first become inundated or activated (Czuba et al., 2019). This may be due to the floodplain (and floodplain channels specifically) modulating SSC in the river or it could be due to a lack of sampling at higher flows. As flow increases above 268 m^3/s, the SSC in the river may plateau or continue to increase slightly. For context, we also show measured SSC in regards to the rising and falling limb and season (Figure 2.10a). But again, due to the lack of sampling across a range of flows (particularly for the data on the rising limb) we do not attempt any statistical analyses of this dataset. Most sediment in suspension in the river at the USGS gage is fines (finer than 62.5 µm; Figure 2.10b). There is no clear pattern in percent fines measured in regards to flow, the rising and falling limb, or season from these measurements (Figure 2.10b). This may in part be due to the presence of a low-head dam just upstream of the USGS gage that likely traps some sand (see description and location in Czuba et al., 2019).

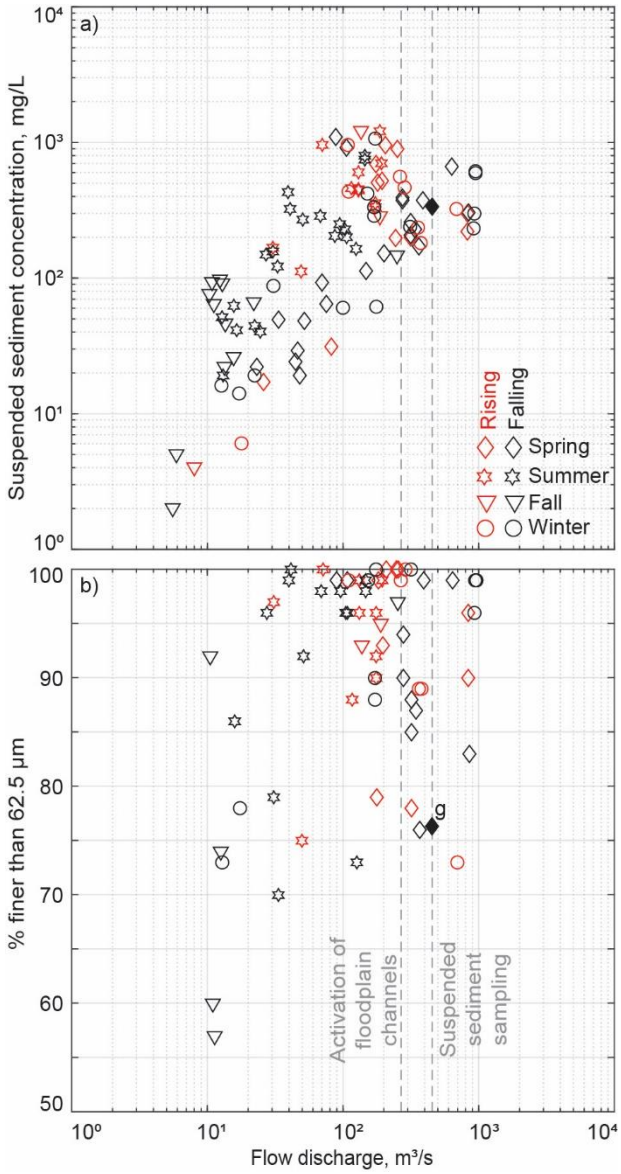

Figure 2.10. Suspended sediment measured at USGS streamflow-gaging station 03365500 East Fork White River at Seymour, Indiana (approximately 5.7 km along the channel centerline downstream from the AOI). (a) Suspended sediment concentration (mg/L) and (b) percent fines (finer than 62.5 µm) on the rising (red) and falling (black) limb of the hydrograph during different seasons (symbols). Solid black diamond shows the value measured in the river at sampling location 'g' (from Figure 2.9) at a flow of 454 m^3/s. First dashed line represents the activation of floodplain channels (268 m^3/s; Czuba et al., 2019) and second dashed line indicates the flow (454 m^3/s) representative of conditions at the time of suspended sediment sampling (Figure 2.9).

2.4.5 Comparison of PFIGS with measured data

We compared our predicted PFIGS grain sizes with a range of grain sizes from measured distributions (D50-D99). Suspended sediment in the river (1 location) and floodplain (6 locations) were compared with PFIGS and LSM in suspension at the sampling flow (454 m^3/s). The D97 in suspension from measured data in the floodplain best agreed with PFIGS and the LSM in suspension at the sampling flow (PFIGS: 0.04 mm MAE, 0.06 mm RMSE, 32% NMAE, 49% NRMSE, and 35% RRMSE; LSM: 0.04 mm MAE, 0.05 mm RMSE, 38% NMAE, 46% NRMSE, and 47% RRMSE; n=6 excluding the river sample; Figure 2.11). At one distal floodplain channel location ('f' in Figure 2.9a), D90 was the best match with PFIGS and LSM in suspension, and in the river, D85 was the best match with PFIGS and D86 was the best match with LSM. Best matches of measured suspended sediment percentile sizes with PFIGS and LSM in suspension ranged from D94 to D99 (PFIGS: 2 MAE, 3.3 RMSE; LSM: 1.8 MAE, 3 RMSE; n=6 excluding river sample).

The D98 from measured bed material samples best agreed with PFIGS as bedload (PFIGS: 3.6 mm MAE, 6.9 mm RMSE, 83% NMAE, 157% NMAE, and 97% RRMSE, n=47; Figure 2.11). The D98 of measured bed material spans nearly two orders of magnitude (449 µm to 16 mm; Figure 2.11). The two locations farthest to the right (in Figure 2.11) where PFIGS is over estimating the sediment sizes are on the bank of the river where close proximity to the river, in the model, leads to a high PFIGS. Other sources of variability included a few locations with randomly larger particles (gravel) in the sample (highest orange circles above the 1:1-line, Figure 2.11; here D75 was generally the best match with PFIGS) and a few locations likely affected by backwater, just upstream of a roadway culvert, for instance (lowest orange circles below the 1:1-line, Figure 2.11). Including all the variability

of all locations, D98 is the best match with PFIGS as bedload, ranging from D90 to D99, and with a 2.4 MAE and 4.5 RMSE (n=47).

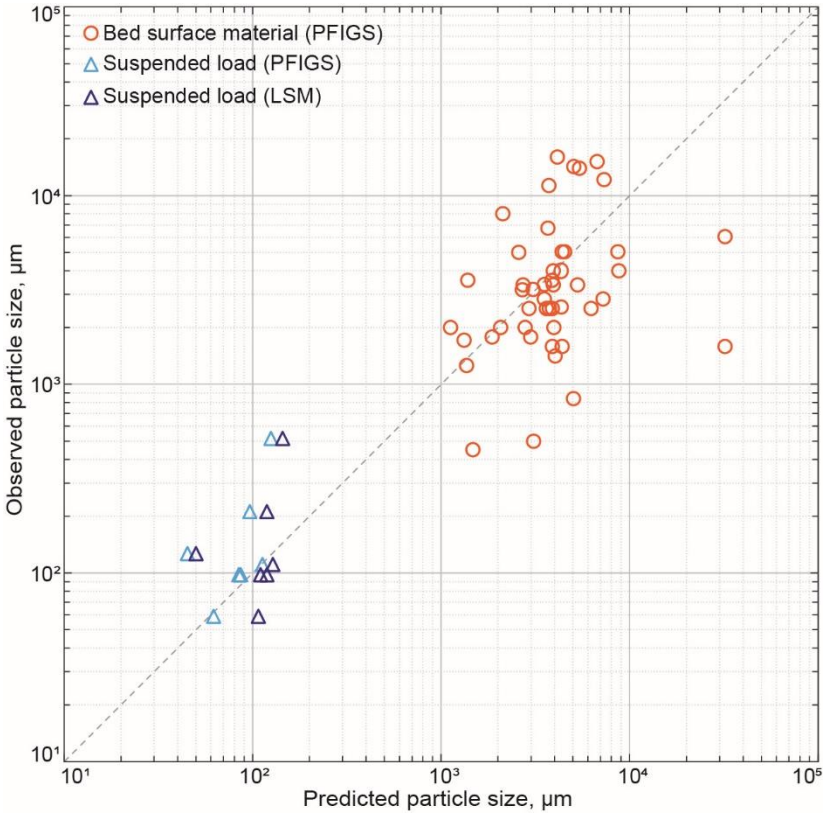

Figure 2.11. Comparison of predicted and observed sediment sizes (µm). PFIGS in suspension (light blue triangles) and LSM at the sampling flow (dark blue triangles; 454 m^3/s) (7 sampling locations) shows good agreement with measured suspended sediment D97. PFIGS as bedload shows good agreement with the D98 (orange circles) of measured floodplain surface (44 sampling locations) and river bar (3 locations). Sampling locations cover a wide range of topographic variation including floodplain channels, depressions, and islands and river bar. See Figure 2.1b for sampling locations.

2.5 Discussion

The EFWR is capable of regularly suspending sediment (the largest size for which the Rouse number, Z_R < 2.43) as coarse as sand (62 to 125 µm; Figure 2.7) high enough in the water column to overtop the river bank and supply the floodplain (Figure 2.9, locations a, b, c). While we do see coarser sands in suspension in the river (Figure 2.9b), these sediments are likely suspended lower in the water column and are not as easily lifted sufficiently high in suspension. During high-frequency floods, the supplied suspended sediment from the river to the floodplain can easily fall out of suspension as the transport capacity is much lower on the floodplain (Figure 2.4 and 2.9). These first flows that inundate the floodplain may be capable of modulating the SSC in the river (Figure 2.10a). We hypothesize that this could occur by the exchange of water from the river to the floodplain, with sediment deposition, and then that water returning back to the river, where this occurs many times over a long reach with many floodplain channels. It is beyond the scope of this study to delve further into this hypothesis, but we leave it for future work with perhaps more field data collection or a morphodynamic model. As flow increases, the SSC in the river may be increasing, however more data are necessary to say with statistical confidence (Figure 2.10a). This could occur because with increasing flow the fraction of suspended sediment depositing on the floodplain decreases, allowing for more suspended sediment to pass over the floodplain and return back to the river, thereby progressively lessening dilution of the SSC in the river. At the highest observed flow, the flow over the floodplain can suspend and convey the 125 µm sediment sizes supplied by the river, essentially passing this sediment across the floodplain with little potential for deposition (Figure 2.4f and 6c). To summarize, fine sediment suspended in the river can deposit on the floodplain during high-frequency floods, but during low-frequency floods, more of the supplied sediment can remain suspended as it passes over the floodplain.

At the same time, these floodplain channels are highly efficient at transporting sediment, and model results suggest that sediment sizes up to 1 to 8 mm (Figure 2.7) can readily be transported as bedload. In the field, at locations where gravel farm roads cross floodplain channels, we have found angular gravel (~2 cm diameter) washed downstream in floodplain channels. These floodplain channels clearly are capable of transporting gravel. This means that any sediment that falls out of suspension in a floodplain channel could still move along the bed. Furthermore, PFIGS as bedload is predictive of the D98 of the surface of floodplain channels (Figure 2.11). This suggests floodplain channels are supply limited and the grain size distribution of the bed surface is set by the flow conditions (Buffington & Montgomery, 1999; Dietrich et al., 1989; Nelson et al., 2009). If the floodplain channels were transport limited, then the grain size distribution would be strongly related to the grain size distribution of the sediment supply (much finer) and not floodplain surface hydraulics (i.e., via PFIGS) (Buffington & Montgomery, 1999; Leopold, 1992; Nolan and Marron, 1995; Rice, 1994). Therefore, floodplain channels that are supply limited are most likely erosional.

It is possible that the cumulative deposition during high-frequency floods could counteract erosion during low-frequency floods, leading to net deposition in floodplain channels. We did not try to quantity the amount of fine sediment that falls out of suspension on the floodplain during high-frequency floods. However, if fine sediment deposition was overwhelming erosion, then the surface grain size should be much finer and not reflective of the LSM/PFIGS as bedload. Therefore, we conclude that the floodplain channels of the EFWR are net erosional. Though, morphodynamic simulations and additional field measurements would help to confirm this conclusion.

A limitation of this analysis is that we do not fully account for flow-vegetation-sediment interactions. In the 2-D HEC-RAS model, vegetation was only accounted for by a Manning’s roughness value based on the National Land-Cover Dataset. Therefore, most of

the floodplain is treated as agricultural lands with a calibrated n-value of 0.050 (Czuba et al., 2019). The National Land-Cover Dataset has a 30-m resolution and, in general, is not sufficient to characterize the variation in vegetation types we see in the field: floodplain channels with corn, soybeans, barren, grass, and weeds. Furthermore, this does not account for the seasonal changes where floodplain channels planted with corn and soybeans are barren with some crop residue in the winter and early spring when some of the highest flows can occur. We interpret our results as being most applicable to floodplain channels that are barren or seasonally barren. It is likely that perennial vegetation in floodplain channels would further dampen flow momentum (not accounted for in the 2-D HEC-RAS model) and promote sediment deposition. Fully exploring this dynamic is a future research direction.

An important advancement presented in this paper is the idea of an effective grain size that is computed as the PFIGS. The effective grain size translates the idea of an effective discharge (Wolman & Miller, 1960) to sediment size and indicates a morphodynamically important grain size assuming the grain size distribution is set by flow hydraulics. With accompanying floodplain surface sediment size data (Figure 2.11), we were able to assess whether this floodplain, and the floodplain channels specifically, are on a net erosional or depositional trajectory. By computing the PFIGS as bedload, we were able to predict the upper end of the grain size distribution of the bed sediment in floodplain channels (D93 to D99). Additionally, by computing the PFIGS in suspension (and the LSM at the sampling flow), we were able to predict the upper end of the suspended sediment grain size distribution (D94 to D99). The effective grain size (PFIGS) probabilistically integrates the LSM. Therefore, the effective grain size represents the upper end of the grain size distribution for sediment in transport or on the bed. The D97 or D98 are sizes characteristic of the largest sizes measured. These sizes at the upper end of the grain size distribution are morphodynamically important because they are the “threshold” size, below which grains are

easy to move and above which are more difficult to move. There may be an intermediate-frequency flood for which the PFIGS, and therefore all sizes on the bed, are fully mobile. The size of sediment supplied relative to this effective grain size will dictate whether that sediment is transported or deposited and lead to any subsequent morphodynamic change. This method is expected to be equally applicable to intermittently flooded coastal areas as well.

The EFWR is an end member of floodplains with channels that appear to be highly effective at transporting sediment. It would be interesting to apply the methods developed in analysis of this floodplain to other floodplains. For instance, in non-channelized floodplains where deposition is more prominent, we would expect to see the distributions of LSM as bedload on the floodplain and LSM in suspension in the river (Figure 2.7) with much less separation, more overlap, or perhaps flip-flopped in comparison to the EFWR. Such results would indicate a lower sediment transport capacity over the floodplain and confirm the method's utility across erosional to depositional floodplains. Then, the ultimate utility is in determining what set of conditions lead to floodplains with erosional vs. depositional tendencies. This would also be valuable in designing floodplain restorations to assess the morphodynamic trajectory of engineered floodplain channels. Without fully accounting for all of the flow-vegetation-sediment feedbacks, the floodplain of the EFWR appears to be on a trajectory of continued maintenance of an anastomosing floodplain channel network that one day may serve as a river-avulsion pathway.

2.6 Concluding remarks

We analyzed size-specific sediment transport potential and assessed whether the channelized floodplain of the East Fork White River near Seymour, Indiana, USA is on a net erosional or depositional trajectory. During high-frequency floods, the largest sediment size that can be moved in suspension in the river is larger than on the floodplain, but during low-frequency floods, the largest sediment size that can be moved in suspension in the river and on the floodplain are the same. Our results suggest that, during high-frequency floods, fine sediment suspended in the river can deposit on the floodplain, but during low-frequency floods, more of the supplied sediment can remain suspended as it passes over the floodplain. These floodplain channels can transport sand-size particles in suspension and gravel-size particles as bedload. This suggests that these floodplain channels could transport the sediment supplied by the river as bedload, which indicates that these floodplain channels are supply limited and the grain size distribution of the bed surface is set by the flow conditions. Supply limited floodplain channels are likely erosional. Finally, our proposed method of probabilistically integrating the largest sediment size that can be moved at various flows can be used to predict the upper end of the grain size distribution in suspension and in bed material, which is applicable to floodplains and coastal areas.

References for Chapter 2

Allen, J. R. L. (1965). A Review of the Origin and Characteristics of Recent Alluvial Sediments. Sedimentology, 5(2), 89–191. https://doi.org/10.1111/j.1365-3091.1965.tb01561.x

Bates, P. D., Anderson, M. G., Price, D. A., Hardy, R. J., & Smith, C. N. (1996). Analysis and development of hydraulic models for floodplain flows. Floodplain processes, 215-254.

Benke, A. C., Chaubey, I., Ward, G. M., & Dunn, E. L. (2000). Flood pulse dynamics of an unregulated river floodplain in the southeastern U.S. coastal plain. Ecology, 81(10), 2730–2741. https://doi.org/10.1890/0012-9658(2000)081[2730:FPDOAU]2.0.CO;2

Bristow, C. S., Skelly, R. L., & Ethridge, F. G. (1999). Crevasse splays from the rapidly aggrading, sand-bed, braided Niobrara River, Nebraska: Effect of base-level rise. Sedimentology, 46(6), 1029–1047. https://doi.org/10.1046/j.1365-3091.1999.00263.x

Brown, A. G. (1996). Floodplain palaeoenvironments, In M. G. Anderson, P. D. Bates, and D. E. Walling (Eds.), Floodplain Processes. (pp. 95–138), Hoboken, NJ: Wiley.

Brownlie, W. R. (1981). Prediction of flow depth and sediment discharge in open channels. Report No. KH-R-43A, Keck Laboratory of Hydraulics and Water Resources, California Institute of Technology, Pasadena, California.

Buffington, J. M., & Montgomery, D. R. (1999). Effects of sediment supply on surface textures of gravel-bed rivers, 35(11), 3523–3530. https://doi.org/doi:10.1029/1999WR900232

Crawford, C. G., Lydy, M. J., & Frey, J. W. (1996). Fishes of the White River Basin, Indiana. U.S. Geological Survey Water-Resources Investigations Report 96–4232, 8 P. Reston, VA: U.S. Geological Survey.

Czuba, J. A., David, S. R., Edmonds, D. A., & Ward, A. S. (2019). Dynamics of Surface-Water Connectivity in a Low-Gradient Meandering River Floodplain. Water Resources Research, 55(3), 1849–1870. https://doi.org/10.1029/2018WR023527

David, S. R., Czuba, J. A., & Edmonds, D. A. (2019). Channelization of meandering river floodplains by headcutting. Geology, 47(1), 15–18. https://doi.org/10.1130/G45529.1

David, S. R., Edmonds, D. A., & Letsinger, S. L. (2017). Controls on the occurrence and prevalence of floodplain channels in meandering rivers. Earth Surface Processes and Landforms, 42(3), 460–472. https://doi.org/10.1002/esp.4002

Despotovic, M., Nedic, V., Despotovic, D., & Cvetanovic, S. (2016). Evaluation of empirical models for predicting monthly mean horizontal diffuse solar radiation. Renewable and Sustainable Energy Reviews, 56, 246–260. https://doi.org/10.1016/j.rser.2015.11.058

Dietrich, W. E. (1987). Mechanics of flow and sediment transport in river bends. In River channels: Environment and process (Vol. 18, pp. 179-227). Oxford: Blackwell.

Dietrich W.E., Kichner J.W., Ikeda H., & Iseya F. (1989). Sediment Supply and the Development of the Surface Layer in Gravel Bedded Rivers. Nature, 340(1975), 215–217.

Edwards, T.K., and Glysson, G.D., 1999, Field Methods for Measurement of Fluvial Sediment: U.S. Geological Survey Techniques of Water-Resources Investigations, Book 3, Chapter C2, 89 p

Engelund, F. (1965a). A criterion for the occurrence of suspended load. La Houille Blanche, 8(7).

Engelund, F. (1965b). Turbulent energy and suspended load. Coastal Eng. Lab., Tech. Univ. of Denmark, Rep, (10).

Fagan, S. D., & Nanson, G. C. (2004). The morphology and formation of floodplain-surface channels, Cooper Creek, Australia. Geomorphology, 60(1–2), 107–126. https://doi.org/10.1016/j.geomorph.2003.07.009

Ferguson, R. I., & Church, M. (2004). A Simple Universal Equation for Grain Settling Velocity. Journal of Sedimentary Research, 74(6), 933–937. https://doi.org/10.1306/051204740933

Garcia, M. (Ed.). (2008, May). Sedimentation engineering: processes, measurements, modeling, and practice. American Society of Civil Engineers.

Guy, H. P. (1969), Laboratory theory and methods for sediment analysis, in Techniques of Water-Resources Investigations of the U.S. Geol. Surv., book 5, chap. C1, 55 p, Reston, Va. [Available at http://pubs.usgs.gov/twri/twri5c1/.]

Homer, C. G., Dewitz, J. A., Yang, L., Jin, S., Danielson, P., Xian, G., et al. (2015). Completion ofthe 2011 National Land Cover Database for the conterminous United States—Representing a decade of land cover change information. Photogrammetric Engineering and Remote Sensing, 81(5), 345–354.

Jackson, R. G. (1976), Depositional model of point bars in the lower Wabash River, J. Sediment. Petrol., 46, 579–594.

James, C. S. (1985). Sediment transfer to overbank sections. Journal of hydraulic research, 23(5), 435-452.

Kleinhans, M. G., & van den Berg, J. H. (2011). River channel and bar patterns explained and predicted by an empirical and a physics-based method. Earth Surface Processes and Landforms, 36(6), 721–738. https://doi.org/10.1002/esp.2090

Knight, D., & Shiono, K. (1996). River channel and floodplain hydraulics. In M. G. Anderson, P. D. Bates, & D. E. Walling (Eds.), Floodplain Processes (pp. 139–182). Hoboken, NJ: Wiley.

Kupfer, J. A., Meitzen, K. M., & Gao, P. (2015). Flooding and surface connectivity of Taxodium-Nyssa stands in a southern floodplain forest ecosystem. River Research and Applications, 31(10), 1299–1310. https://doi.org/10.1002/rra.2828

Lamb, M. P., & Venditti, J. G. (2016). The grain size gap and abrupt gravel-sand transitions in rivers due to suspension fallout. Geophysical Research Letters, 43(8), 3777–3785. https://doi.org/10.1002/2016GL068713

Lauer, J. W., & Parker, G. (2008). Modeling framework for sediment deposition, storage, and evacuation in the floodplain of a meandering river: Application to the Clark Fork River, Montana. Water Resources Research, 44(8), 1–16. https://doi.org/10.1029/2006WR005529

Lauer, J. W., & Willenbring, J. (2010). Steady state reach-scale theory for radioactive tracer concentration in a simple channel/floodplain system. Journal of Geophysical Research: Earth Surface, 115(4), 1–21. https://doi.org/10.1029/2009JF001480

Leopold, L. B. (1992). Sediment Size That Determines Channel Morphology. Dynamics of Gravel-Bed Rivers, 297–311.

Lewin, J., & Ashworth, P. J. (2014). The negative relief of large river floodplains. Earth-Science Reviews, 129, 1–23. https://doi.org/10.1016/j.earscirev.2013.10.014

Lewin, J., Ashworth, P. J., & Strick, R. J. P. (2017). Spillage sedimentation on large river floodplains. Earth Surface Processes and Landforms, 42(2), 290–305. https://doi.org/10.1002/esp.3996

Limaye, A. B. (2017). Extraction of Multithread Channel Networks With a Reduced-Complexity Flow Model. Journal of Geophysical Research: Earth Surface, 122(10), 1972–1990. https://doi.org/10.1002/2016JF004175

Marriott, S. (1992). Textural analysis and modelling of a flood deposit: River Severn, UK. Earth Surface Processes and Landforms, 17(7), 687-697.

McKean, J. and Tonina, D., (2013), Bed stability in unconfined gravel bed mountain streams: With implications for salmon spawning viability in future climates, Journal of Geophysical Research: Earth Surface, 118, 3, doi:10.1002/jgrf.20092.

Mertes, L. A. K., Dunne, T., & Martinelli, L. A. (1996). Channel-floodplain geomorphology along the Solimões-Amazon River, Brazil. Bulletin of the Geological Society of America, 108(9), 1089–1107. https://doi.org/10.1130/0016-7606(1996)108<1089:CFGATS>2.3.CO;2

Middelkoop, H., Van, M., & Perk, D. (1998). Modelling Spatial Patterns of Overbank Sedimentation on Embanked Floodplains. Source: Geografiska Annaler. Series A, Physical Geography, 80(2), 95–109. https://doi.org/10.1111/j.0435-3676.1998.00029.x

Moody, J. A., Pizzuto, J. E., & Meade, R. H. (1999). Ontogeny of a flood plain. Geological Society of America Bulletin, 111(2), 291-303.

Nanson, G. C. (1980). Point bar and floodplain formation of the meandering Beatton River, northeastern British Columbia, Canada. Sedimentology, 27(1), 3–29. https://doi.org/10.1111/j.1365-3091.1980.tb01155.x

Nanson, G. C. (1986). Episodes of vertical accretion and catastrophic stripping: a model of disequilibrium flood-plain development. Geological Society of America Bulletin, 97(12), 1467-1475.

Nanson, G. C., & Croke, J. C. (1992). A genetic classification of floodplains. Geomorphology, 4, 459–486. https://doi.org/https://doi.org/10.1016/0169-555X(92)90039-Q

Nelson, P. A., Venditti, J. G., Dietrich, W. E., Kirchner, J. W., Ikeda, H., Iseya, F., & Sklar, L. S. (2009). Response of bed surface patchiness to reductions in sediment supply. Journal of Geophysical Research: Earth Surface, 114(2), 1–18. https://doi.org/10.1029/2008JF001144

Nicholas, A. P., & Mitchell, C. A. (2003). Numerical simulation of overbank processes in topographically complex floodplain environments. Hydrological Processes, 17(4), 727–

746. https://doi.org/10.1002/hyp.1162

Nicholas, A. P., & Walling, D. E. (1997). Modelling flood hydraulics and overbank deposition on river floodplains. Earth Surface Processes and Landforms. https://doi.org/10.1002/(SICI)1096-9837(199701)22:1<59::AID-ESP652>3.0.CO;2-R

Nicholas, A. P., & Walling, D. E. (1998). Numerical modelling of floodplain hydraulics and suspended sediment transport and deposition. Hydrological Processes, 12(8), 1339–1355. https://doi.org/10.1002/(SICI)1099-1085(19980630)12:8<1339::AID-HYP618>3.0.CO;2-6

Nicholas, A. P., Walling, D. E., Sweet, R. J., & Fang, X. (2006). Development and evaluation of a new catchment-scale model of floodplain sedimentation. Water Resources Research, 42(10), 1–13. https://doi.org/10.1029/2005WR004579

Nicholas, A. R., & McLelland, S. J. (2004). Computational fluid dynamics modelling of three-dimensional processes on natural river floodplains. Journal of Hydraulic Research, 42(2), 131–143. https://doi.org/10.1080/00221686.2004.9628299

Nicholas, A. P., & Walling, D. E. (1996). The significance of particle aggregation in the overbank deposition of suspended sediment on river floodplains. Journal of Hydrology, 186(1–4), 275–293. https://doi.org/10.1016/S0022-1694(96)03023-5

Niño, Y. (1995). Particle motion in the near bed region of a turbulent open channel flow: implications for bedload transport by saltation and sediment entrainment into suspension (Doctoral dissertation, University of Illinois at Urbana-Champaign).

Niño, Y., & García, M. (1998). Engelund's analysis of turbulent energy and suspended load. Journal of Engineering Mechanics, 124(4), 480–483. https://doi.org/10.1061/(ASCE)0733-9399(1998)124:4(480)

Niño, Y., Lopez, F., & Garcia, M. (2003). Threshold for particle entrainment into suspension. Sedimentology, 50(2), 247–263. https://doi.org/10.1046/j.1365-3091.2003.00551.x

Nolan, K. M., & Marron, D. C. (1995). History, causes, and significance of changes in the channel geometry of Redwood Creek, northwestern California, 1936 to 1982. Geomorphic Processes and Aquatic Habitat in the Redwood Creek Basin, Northwestern California. US Geological Survey Professional Paper, 1454, N1-N22.

Nunnally, N. R. (1967). Definition and Identification of Channel and Overbank Deposits and Their Respective Roles In Flood Plain Formation. Professional Geographer, 19(1), 1–4. https://doi.org/10.1111/j.0033-0124.1967.00001.x

O'Brien, P. E., & Wells, a. T. (1986). A small, alluvial crevasse splay. Journal of Sedimentary Research, 56(6), 876–879. https://doi.org/10.1306/212F8A71-2B24-11D7-8648000102C1865D

Park, E., & Latrubesse, E. M. (2017). The hydro-geomorphologic complexity of the lower Amazon River floodplain and hydrological connectivity assessed by remote sensing and field control. Remote Sensing of Environment, 198, 321–332. https://doi.org/10.1016/j.rse.2017.06.021

Pizzuto, J. E. (1987). Sediment diffusion during overbank flows. Sedimentology, 34(2), 301–317. https://doi.org/10.1111/j.1365-3091.1987.tb00779.x

Pizzuto, J. E., Moody, J. A., & Meade, R. H. (2008). Anatomy and Dynamics of a

Floodplain, Powder River, Montana, U.S.A. Journal of Sedimentary Research, 78(1), 16–28. https://doi.org/10.2110/jsr.2008.005

Phillips, J.D., 2011. Universal and local controls of avulsions in southeast Texas Rivers. Geomorphology 130, 17–28.

Rak, G., Kozelj, D., & Steinman, F. (2016). The impact of floodplain land use on flood wave propagation. Natural Hazards, 83(1), 425–443. https://doi.org/10.1007/s11069-016-2322-0

Reinfelds, I., & Nanson, G. (1993). Formation of braided river floodplains, Waimakariri River, New Zealand. Sedimentology, 40(6), 1113–1127. https://doi.org/10.1111/j.1365-3091.1993.tb01382.x

Rice, S. (1994). Towards a model of changes in bed material texture at the drainage basin scale. Process models and theoretical geomorphology, edited by M. J. Kirkby, pp. 160-172, John Wiley, New York, 1994.

Rudorff, C. M., Melack, J. M., & Bates, P. D. (2014). Flooding dynamics on the lower Amazon floodplain: 2. Seasonal and interannual hydrological variability. Water Resources Research, 50(1), 635–649. https://doi.org/10.1002/2013WR014714

Schuurman, F., Marra, W. A., & Kleinhans, M. G. (2013). Physics-based modeling of large braided sand-bed rivers: Bar pattern formation, dynamics, and sensitivity. Journal of Geophysical Research: Earth Surface, 118(4), 2509–2527. https://doi.org/10.1002/2013JF002896

Sturm, T. (2001). Open hydraulics channel, 493. Univenity of Caldornia, Davis, ISBN: 0-07-062445-3

Thayer, J. B., & Ashmore, P. (2016). Floodplain morphology, sedimentology, and development processes of a partially alluvial channel. Geomorphology, 269, 160–174. https://doi.org/10.1016/j.geomorph.2016.06.040

Trigg, M. A., Bates, P. D., Wilson, M. D., Schumann, G., & Baugh, C. (2012). Floodplain channel morphology and networks of the middle Amazon River. Water Resources Research, 48(10). https://doi.org/10.1029/2012WR011888

USGS, (2020). https://nwis.waterdata.usgs.gov/in/nwis/qwdata/?site_no=03365500&agency_cd=USGS

Van Dijk, W. M., Van de Lageweg, W. I., & Kleinhans, M. G. (2013). Formation of a cohesive floodplain in a dynamic experimental meandering river. Earth Surface Processes and Landforms, 38(13), 1550–1565. https://doi.org/10.1002/esp.3400

Van Rijn, L. C. V. (1984). Sediment transport, part II: suspended load transport. Journal of hydraulic engineering, 110(11), 1613-1641

Viparelli, E., Wesley Lauer, J., Belmont, P., & Parker, G. (2013). A numerical model to develop long-term sediment budgets using isotopic sediment fingerprints. Computers and Geosciences, 53, 114–122. https://doi.org/10.1016/j.cageo.2011.10.003

Wolman, M. G., & Leopold, L. B. (1957). River flood plains: Some observations on their formation, U.S. Geological Survey Professional Paper, 282-C, 87–107. Reston, VA: U.S. Geological Survey.

Wolman, M. G., & Miller, J. P. (1960). Magnitude and Frequency of Forces in Geomorphic Processes. The Journal of Geology, 68(1), 54–74. https://doi.org/10.1086/626637

Xu, H., Steeg, S. Van Der, Sullivan, J., Shelley, D., & Cely, J. E. (2020). Intermittent Channel Systems of a Low-Relief , Low-Gradient Floodplain : Comparison of Automatic Extraction Methods. https://doi.org/10.1029/2020WR027603

Zwoliński, Z. (1992). Sedimentology and geomorphology of overbank flows on meandering river floodplains. Geomorphology, 4(6), 367–379. https://doi.org/10.1016/0169-555X(92)90032-J

Chapter 3 Incorporating Flowpaths as an Explicit Measure of River-Floodplain Connectivity to Improve Predictions of Floodplain Sediment Deposition

Sumaiya Sumaiya[1], John T. Schubert[1,2], Jonathan A. Czuba[1], James E. Pizzuto[3]

Abstract

Floodplain topographic relief can lead to gradual flooding across a floodplain and increase river-floodplain connectivity. In this work, we show that incorporating hydrologic flowpaths as an explicit measure of river-floodplain connectivity can improve predictions of floodplain sediment deposition. We focus on the floodplain of the South River, Virginia, where historical mercury contamination has occurred and where measurements of mercury accumulation have been used to estimate decadal-scale sedimentation rates. We developed a 2D HEC-RAS hydrodynamic model for the South River downstream of Waynesboro, Virginia, and used simulated model results with sediment deposition data to create predictive multiple linear regression models describing sedimentation across the floodplain. All of our predictive models incorporated a flowpath length from the location on the floodplain downstream to the riverbank as an explicit measure of river-floodplain connectivity that improved our predictions of floodplain sediment deposition (best model with r^2=0.67). We applied our best regression model to our hydrodynamic model results to create a spatial map of floodplain sedimentation rate and discuss differences on three separate sections of floodplain. We found that two sections of floodplain with variable topography had wider, bimodal probability distribution functions (PDFs) of sedimentation rate (aggregated spatially), capturing greater deposition in low-lying areas that were frequently inundated. The third floodplain without this topographic relief had a much narrower log-normal PDF of sedimentation rate with much lower values. Our work highlights how floodplain topography

and river-floodplain connectivity affect sedimentation rates and can help inform the development of floodplain sediment budgets.

Keywords: 2D HEC-RAS, floodplain sedimentation, floodplain topography, mercury contamination, river-floodplain connectivity, South River.

Key Points:

1. Flowpath length, flow exceedance probability, and suspended sediment concentration best explain sedimentation rate on the South River floodplain.

2. Floodplain topographic variability led to wider, bimodal spatial PDFs of sedimentation rate compared to a narrower log-normal PDF without this variability.

3. Incorporating flowpaths as an explicit measure of river-floodplain connectivity improved predictions of floodplain sediment deposition to r^2=0.67.

3.1 Introduction

Floodplains are important fluvial features in the riparian landscape that provide habitat for biota (Benjankar et al., 2011; Mahoney & Rood, 1998; Nakamura et al., 1997), trap sediment and organic material (Hopkins et al., 2018; Hupp et al., 2019; Sutfin et al., 2016; Wiener et al., 2022), and attenuate flood waves reducing downstream flood risk (Rak et al., 2016; Williams et al., 2012). The formation and evolution of a floodplain is a complex process involving both sediment deposition through lateral migration of sand and gravel point bar deposits and vertical overbank accretion of finer sand, silt, and clay (Brown, 1996; Jackson, 1976; Lauer & Parker, 2008; Nanson, 1980; Nanson & Croke, 1992; Normally, 1967; Wolman & Leopold, 1957). For lowland floodplains, vertical accretion of overbank sediment tends to dominate floodplain formation compared to lateral channel migration (Middelkoop & van der Perk, 1998; Nanson & Croke, 1992; Walling & He, 1998).

A significant portion of the eroded sediment from a drainage basin is deposited within river channel belts and floodplains (Allison et al., 1998; Costa, 1975; Goodbred & Kuehl, 1998; Lambert & Walling, 1987; Walling, 1983). Sediment transported and deposited in the floodplain during an overbank flow can be stored in the floodplain for decades or much longer (Pizzuto, 2014; Pizzuto et al., 2008). Estimating the deposited sediment volume in floodplains is an integral part of calculating a sediment budget (Belmont et al., 2011; Dunne et al., 1998; Fryirs & Brierley, 2001; Goodbred & Kuehl, 1998; Malmon et al., 2002; Nicholas et al., 2006; Park, 2020; Trimble, 1999). The floodplain component of a sediment budget quantifies the inputs, outputs, and storage within the floodplain control volume (Allmendinger et al., 2007; Wohl, 2021).

There are a number of methods that have been used to quantify one or more aspects of the floodplain component in a watershed or reach-scale sediment budget. Regression models

have been developed to explain the spatial variability of sediment and nutrients (Hopkins et al., 2018) and to estimate the deposited sediment volume on a floodplain (Chen et al., 2019; Noe et al., 2022). Seasonal and annual patterns of floodplain sediment storage have been calculated from the measurement of water level and flow discharge in combination with surface suspended sediment maps from remote sensing (Park, 2020; Park & Latrubesse, 2019). Naipal et al. (2016) developed a floodplain sediment budget by simulating spatial patterns and long-term trends of soil erosion and redistribution in floodplains from a sediment mass-balance model. Schenk et al. (2013) expressed floodplain storage as net and gross floodplain trapping factors. Wasson (2003) used a simple approach to estimate sediment storage by measuring the floodplain dimensions and estimating the sediment deposition rate from sediment dating. Moody (2019) used long term measurements of the cross-section topography of active floodplains and point bar to develop dynamic relations between peak-flood discharge and annual sediment deposition.

Over the years many different methods have been developed to estimate sedimentation rates on floodplains over different timescales. At an event timescale, these methods include post-flood topographic surveying, measuring depth of deposits from probing and digging shallow pits, measuring high-water marks on trees and buildings, aerial image analysis (Brinke et al., 1998; Gomez et al., 1997; Kesel et al., 1974), sediment traps (Middelkoop & Asselman, 1998; Walling & Bradley, 1989), and artificial clay pads markers (Hupp et al., 2015; Shenk et al., 2013). At 10+ year timescales, these methods include fallout radionuclides 137Cs and 210Pb (Allison et al., 1998; Du & Walling, 2012; Goodbred & Kuehl, 1998; He & Walling, 1996a, 1996b; Remor et al., 2022; Terry et al., 2002, 2006; Walling & He, 1997a, 1997b), tree-ring (dendrogeomorphic) techniques (Hupp et al., 2015; Mizugaki et al., 2006; Remo et al., 2018; Tichavský et al., 2018), repeat surveying of monumented cross sections (Leopold, 1973; Trimble, 1983), and pollen analyses (Hupp et al.,

2015). All of these methods directly or indirectly measure the sedimentation rate at a limited spatial extent (point scale) and many such measurements are required to accurately assess the spatial distribution of sedimentation rates across the floodplain.

Sediment deposition pattern, rate, and amount on the floodplain is governed by variable hydraulic and geomorphic parameters such as duration and frequency of inundation, flow depths and velocities, sediment load, suspended sediment concentration, flow patterns over the floodplain, vegetation density, and sediment transport mechanism (Maaß & Schüttrumpf, 2019; Middelkoop & van der Perk, 1998; Nicholas & Mitchell, 2003; Nicholas & Walling, 1997, 1998; Park & Latrubesse, 2019; Pizzuto et al., 2008; Zwoliński, 1992). Studies on overbank flows demonstrated strong control of floodplain topographic features on floodplain inundation frequency, flow depth, and velocities (Bates, 1992; Czuba et al., 2019; Lewin & Hughes, 1980; Lindroth et al., 2020; Nicholas & McLelland, 2004; Nicholas & Walling, 1997). Furthermore, floodplain topography has been shown to be highly correlated with overbank sedimentation rates (Middelkoop & Asselman, 1998; Nicholas & Walling, 1998). Floodplain topographic surfaces consist of both positive and negative relief from features such as surface depressions, channel margin slackwater zones, bar-shelter backwaters, tie channels, internal drainage channel networks, drainage ditches, and abandoned channels (Lewin & Ashworth, 2014). Proper representation of these floodplain features is a prerequisite in accurate estimation of sedimentation pattern, rate, and amount (Middelkoop & van der Perk, 1998; Nicholas & Walling, 1997).

Numerical and mathematical models have been applied to simulate river-floodplain hydraulics (Anees et al., 2016; Bates et al., 2005; Horritt & Bates, 2002) and sediment transport and deposition processes (Asselman & van Wijngaarden, 2002; Büttner et al., 2006; Hardy et al., 2000; Nicholas et al., 2006) over a range of time scales and variable topography (Ahilan et al., 2018; Benjankar & Yager, 2012; Middelkoop & van der Perk, 1998; Nicholas

& Mitchell, 2003; Nicholas & Walling, 1997, 1998). Most of these numerical modelling approaches have been limited by poor resolution of topographic data (Hardy et al., 2000; Lauer, 2008; Viparelli et al., 2013) (prior to the widespread availability of lidar data) and considered the floodplain as a flat surface adjacent to the river (Karssenberg & Bridge, 2008). Lidar data with its ability to represent floodplain topography at meter-scale resolution (Hilldale and Raff, 2008) can reveal the complex nature of floodplain hydro-morphodynamic processes (David et al., 2017, 2018; Kupfer et al., 2015; Rak et al., 2016; Thayer & Ashmore, 2016; Xu et al., 2020). Furthermore, incorporating high-resolution topographic data into numerical models, along with field measurements, can better quantify floodplain processes in detail (Czuba et al., 2019; Maaß & Schüttrumpf, 2019; Sumaiya et al., 2021).

Floodplain topographic relief can lead to gradual flooding across a floodplain and increase river-floodplain connectivity (Czuba et al., 2019; Lindroth et al., 2020; Xu et al., 2021). River-floodplain connectivity is the degree of water-driven transport of matter, energy, and organisms between rivers and their floodplains (Amoros and Bornette, 2002; Freeman et al., 2007; Bracken et al., 2015; Covino, 2017; Tockner et al., 2000). The concept of river-floodplain connectivity for understanding river systems is well established (Amoros & Bornette, 2002; Junk et al., 1989; Ward & Stanford, 1995) and has been investigated by using satellite imagery (Alsdorf et al., 2007; Lesack & Melack, 1995; Lewin & Ashworth, 2014; Mertes, 1997; Mertes et al., 1996; Park & Latrubesse, 2017; Trigg et al., 2012) and more recently with lidar data and numerical modeling (Byrne et al., 2019; Czuba et al., 2019, Stone et al., 2017; Tull et al., 2022). However, directly incorporating an explicit measure of river-floodplain connectivity to improve predictions of sediment deposition on floodplains has not been explored.

The purpose of this work is to show that incorporating hydrologic flowpaths as an explicit measure of river-floodplain connectivity can improve predictions of floodplain

sediment deposition. We focus on the floodplain of the South River, Virginia, where historical mercury contamination has accumulated in the floodplain. Measurements of mercury accumulation have been used to estimate decadal-scale sedimentation rates across hundreds of points on this floodplain (Pizzuto et al., 2016). We developed a 2D HEC-RAS hydrodynamic model for the South River downstream of Waynesboro, Virginia, and used simulated model results to predict measurements of sedimentation rate. The results of our work better inform how floodplain topography and river-floodplain connectivity affect sedimentation rates and can help inform the development of floodplain sediment budgets.

3.2 Study area

The South River flows through Waynesboro, Virginia (drainage area 330 km^2), and flows for another 48 km downstream (drainage area 608 km^2) until it joins the North River at Port Republic, Virginia, to form the South Fork Shenandoah River (Figure 3.1). This reach of the river is a fifth-order, gravel-bed, bedrock river with frequent pools and riffles. The channel has a bankfull width and depth of 40 m and 1.5 m, respectively (Rhoades et al., 2009), and an average slope of 0.0013 (Skalak & Pizzuto, 2010). Frequent bedrock exposures along its bed, banks, and forested riparian zone limit channel migration rates to only a few centimeters per year (Rhoades et al., 2009). The South River floodplain consists of a mixture of pasture, forest, and developed areas and is confined in places by levees, fluvial terraces, quaternary alluvial fans, bedrock valley walls, and a railroad bed. Floodplain sediment accumulation rates along the South River are low, having previously been estimated at rates of only a few centimeters per 100 years (Pizzuto et al., 2016). More recent regional scale analysis (including data collected from the South River; Pizzuto et al., 2022) has revised previous estimates and has reported that modern sediments (1950–present) accumulated at a

median rate of 0.25 cm/year, which is one order of magnitude higher than reported earlier by Pizzuto et al. (2016).

Mercury contamination of the South River was first reported in 1976 (Carter, 1977) but initially introduced from a manufacturing facility in Waynesboro, during 1929–1950. During high overbank flows, mercury-contaminated sediments were transported and deposited on the floodplain (Pizzuto, 2012; Rhoades et al., 2009). Mercury concentrations on suspended sediment reached a peak at about 1,000 mg/kg during 1940–1960, then decreased rapidly to ~10 mg/kg by 1970 (Skalak & Pizzuto, 2010, 2014) and were still observed at ~10 mg/kg around 2006-2009 (Flanders et al., 2010). Mercury-contaminated sediments that cycle between the river and floodplain are an important source of mercury in the South River (Flanders et al., 2010; Rhoades et al., 2009). Pizzuto (2014) found that suspended sediment in transport enters floodplain storage after a relatively short distance (~10 km) and that mercury deposition on near-channel floodplains declines exponentially downstream.

Downstream of Waynesboro, there were 13 colonial mill dams, many established in the 1800s. All of these dams except one were breached by 1957 and the last one was breached in 1976 (Pizzuto & O'Neal, 2009). Overbank sedimentation rates could have been locally higher upstream of mill dams within the mill ponds (Walter & Merritts, 2008). The approximate upstream extent of the backwater influence due to mill dams on the South River was estimated to be within 3 km (Pizzuto & O'Neal, 2009). Studies by Pizzuto (2014, 2016) did not find any strong correlations between mercury deposition on the South River floodplain and the presence of historical mill dams.

There are two USGS streamflow gaging stations within our model domain: USGS 01627500 South River at Harriston (daily data 1925-present) and USGS 01626850 South River at Dooms (daily data 1975-present) (Figure 3.1b). Over the simulated 48 km reach of

the South River, the drainage area nearly doubles, with increasing discharge along the reach. However, we only investigate static flows of a specific discharge uniformly across the entire reach, which captures how a specific location would be inundated by that specific flow, but does not capture a realistic picture of the entirety of the South River during a single flow event. When selecting flows, we chose a range of flows based on the Harriston gage because of its central location in the reach, and for reference, we report recurrence intervals of these flows relative to the Harriston gage because it has the longest data record.

We focus on describing our results within an area of interest (AOI, Figure 3.1c), which is an 8.8 km reach of the South River just downstream of Waynesboro, Virginia, and includes three distinct floodplains A, B, and C (Figure 3.1c). The AOI was based on the inundated extent of the largest flow simulated (peak of record at Harriston, 824 m^3/s). We selected this reach because it is close to Waynesboro, has high concentrations of mercury in its floodplain (Pizzuto, 2014), and there are many field measurements of mercury that were used by Pizzuto et al., (2016) to estimate sedimentation rates.

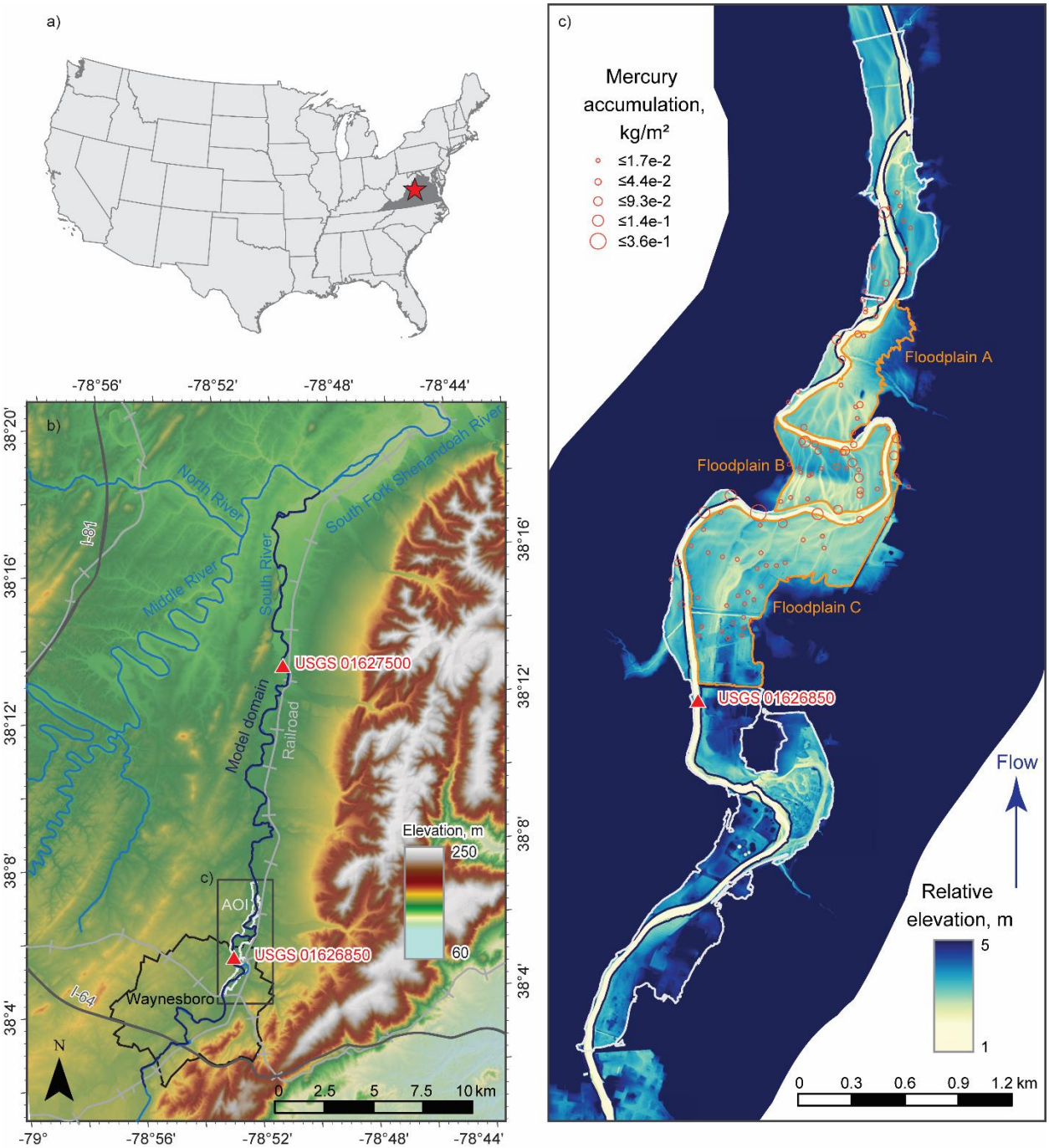

Figure 3.1 Study area of the South River near Waynesboro, Virginia. (a) Red star represents the location of the South River in Virginia, USA. (b) Local setting of the South River downstream of Waynesboro. Dark blue line represents the center line of the South River model domain (HEC-RAS). Red triangles show the location of the USGS gages (01627500 and 01626850) used for model calibration and validation. Light blue lines are other rivers in the area. Light gray line with transverse crosses represents the railroad and the dark gray lines

are highways (I-64 and I-81). Black line demarcates the Waynesboro city boundary and the black rectangle shows the areal extent of (c). White line within the black rectangle is our area of interest (AOI) where we have focused our analysis. (c) Elevation of the floodplain relative to the channel within the AOI as a way of highlighting floodplain features by removing the downstream trending slope from the floodplain topography (Coe, 2016). White line shows the boundary of the AOI and the orange line shows the boundary of three separate sections of floodplain, labeled A, B, and C. Orange circles are the mercury accumulation (kg/m^2) data from Pizzuto et al. (2016); larger sizes indicate higher mercury accumulation.

3.3 Methods

3.3.1 Floodplain sediment and mercury data

Within our AOI, mercury accumulation was measured at 107 sampling locations (orange circles, Figure 3.1c) in the South River channel and floodplain by multiple teams and these data were collectively described by Pizzuto et al. (2016). In 2008, five samples were collected adjacent to the channel and five from cut banks by Pizzuto et al. (2016). The total depth sampled ranged from 1.2 to 2.4 m. At each sample location, the topmost 15 cm was analyzed, deeper deposits were analyzed at intervals of 30 cm. Another 80 floodplain cores were collected by URS Corp in 2008 from the surface down to 75 cm depth. For mercury content, the uppermost 15 cm and the remaining 60 cm cores were analyzed separately (Pizzuto et al., 2016). The Environmental Protection Agency obtained the remaining 17 samples, all were from the surface down to 75 cm deep and sampled at 15-cm intervals (Bruzzesi et al., 2007; Pizzuto et al., 2016). These collected samples were analyzed at commercial laboratories to estimate mercury concentration along with the percent sand, silt, and clay and the percent organic carbon. The total amount of mercury deposited (kg/m^2) in

each location was used by Pizzuto et al. (2016) to estimate a sediment deposition rate (cm/year). Mercury deposition was estimated from the collected samples by applying the equation (Pizzuto et al., 2016):

$$I_{Hg} = \sum_{i=1}^{n} \rho_b \, C_{soilHgi} \, T_i \tag{1}$$

where, I_{Hg} represents mercury deposition (kg/m^2) per unit surface area of the floodplain between 1930 (when mercury was first introduced into the South River) and 2007 when the samples were collected, ρ_b is the floodplain deposit wet bulk density of 1200 kg sediment/m^3 (Pizzuto et al., 2016), $C_{soilHgi}$ is the mercury concentration (units of kg Hg/kg sediment) measured in each soil core, T_i is the sampling interval (m) in each core, and n is the number of sampling intervals in each core.

Mercury deposition I_{Hg} (kg/m^2; 1930-2007) was then converted into a sedimentation rate, T_t (cm/year) by applying the equation (Pizzuto et al., 2016):

$$T_t = \frac{I_{Hg}}{\rho_b T \, C_{Hgs}} \tag{2}$$

where T is the duration of Hg accumulation (1930-2007; 77 years) and C_{Hgs} is the concentration of mercury on suspended sediment, which was initially estimated at 0.000239 kg Hg/kg sediment by Pizzuto et al. (2016). However, after comparing mercury deposition I_{Hg} to sedimentation rates measured by Pizzuto et al. (2022) where both measurements overlapped (at four points), we back-calculated an average C_{Hgs} of 0.00087 kg Hg/kg sediment that we used in our analysis. The reconstruction of mercury concentrations from collected data and the underlying assumptions are described in detail in previous publications (Pizzuto, 2012, 2014; Skalak & Pizzuto, 2010, 2014, Pizzuto et al., 2022). Additionally, the

full process of data collection, laboratory analysis, and conversion of mercury accumulation into sedimentation rate were described by Pizzuto et al. (2016). From here onward, we only focus on the resulting sedimentation rate data.

3.3.2 2D hydrodynamic model

3.3.2.1 Model construction

A two-dimensional unsteady hydrodynamic model was constructed for the South River and its floodplain using 2-D HEC-RAS version 5.0.6 developed by the U.S. Army Corps of Engineers (Brunner, 2016). The model domain included a 48 km reach of the South River and its floodplain from Waynesboro to Port Republic, Virginia (at the confluence of South and North Rivers; Figure 3.1b). The model terrain surface was constructed from 0.76 m lidar data (VGIN, 2017). The elevation of the channel bed was approximated by lowering the water surface at the time of lidar acquisition uniformly by about 1 m, equal to the difference between the lidar water-surface elevation and the zero-discharge stage at the USGS gage (01627500 South River at Harriston, Virginia). This approximation has been shown to provide reasonable results for floodplain-inundating flows when compared to surveyed bathymetry (see supporting information of Czuba et al., 2019). The floodplain topography of the terrain surface was additionally smoothed using a 5 m smoothing window so that smoother streamlines could be generated from the resulting velocity data. The computational mesh was generated with a 23 m nominal orthogonal cell spacing and refined to 7.6 m along break lines positioned along the river channel centerline, banks, major floodplain channels, and roadways. By generating a coarser grid across flat topography and a finer grid in the channel and along structures, we were able to balance model resolution and computational efficiency with 188k cells overall and an average cell area of 371 m^2. The

upstream flux boundary condition was specified as a series of 24 flow discharge values that spanned the range of observed flows at the Dooms and Harriston USGS gages. Each flow was held constant for a few days of model simulation to achieve steady state before incrementing to the next higher flow. The downstream boundary condition was set as normal depth with a friction slope of 0.01. Roughness values were initially assigned based on land cover (Wickham et. al, 2021) using the default Manning's n values from HEC-RAS (Brunner, 2016) and were later adjusted during model calibration.

3.3.2.2 Model calibration and validation

The 2D hydrodynamic HEC-RAS model was calibrated to the USGS streamflow gaging station 01627500 at Harriston (Figure 3.2a; 2b) and validated against the USGS gaging station 01626850 at Dooms (Figure 3.2c; 2d). We calibrated to the Harriston gage because of its longer-term data availability and the floodplain land cover in its vicinity better represented the conditions along the South River. We then validated to the Dooms gage because it was in our AOI. Fourteen land cover-based (2016 National Land Cover Database; Wickham et. al, 2021) Manning’s roughness values were used as calibration parameters (Brunner, 2016).

Table 3.1 The roughness values changed from the default HEC-RAS values (Brunner, 2016)

Land cover	Calibrated roughness values	% of inundated area
Open water	0.0375	12%
Low-intensity developed area	0.06	5%

Medium- and High-intensity developed area	0.05	4%, 6%
Barren	0.035	0.13%
Deciduous, evergreen, and mixed forest	0.0325	14%, 9%, and 1.2%
Developed open space	0.03	8.7%
Pasture/hay	0.015	34.6%
Row-crop agriculture	0.015	5.3%
Woody wetlands	0.08	0.15%

Model calibration at Harriston (USGS 01627500) involved comparing the model simulated water surface elevation (WSEL) with the USGS rating curve (Figure 3.2a) and also comparing the model simulated depth-averaged velocity to the USGS measurements of channel velocity (Figure 3.2b). The reported USGS velocity measurements are cross-sectional average velocities measured at the gage. To appropriately compare to these values, we extracted depth-average velocities along the wetted channel-floodplain cross section at the gage and averaged these values at each flow. Both gage locations were just downstream of a bridge (from where high flow measurements were likely taken) and the bridge abutments confined the flow primarily to the channel for most of the flow conditions considered. The root mean square error (RMSE) of the simulated water surface elevation (WSEL) to the USGS rating curve at Harriston (USGS 01627500) was 0.12 m and mean absolute error (MAE) was 0.10 m (n = 18). The RMSE and MAE of the USGS measurements to the USGS

rating curve at Harriston was 0.25 m and 0.21 m, respectively (n=22; ≥28 m^3/s, RI: 1-year) (Figure 3.2a). Model error compared to the USGS rating curve was close to the variability between the USGS measurements and the rating curve and was therefore considered acceptable (Czuba et al., 2019; Sumaiya et al., 2021). The RMSE and MAE of the model simulated depth-averaged velocity to the USGS measurements of channel velocity was 0.25 m/s and 0.21 m/s, respectively (n=21; ≥28 m^3/s, RI: 1-year) (Figure 3.2b).

Model validation at Dooms (USGS 01626850) involved comparing the model simulated water surface elevation with USGS rating curve (Figure 3.2c) and also comparing the model simulated depth-averaged velocity to the USGS measurements of channel velocity (Figure 3.2d). The RMSE of the simulated WSEL to the USGS rating curve (Figure 3.2c) was 0.13 m and MAE was 0.11 m (n =15). The RMSE of the USGS measurements to the USGS rating at Dooms was 0.10 m and 0.07 m, respectively (n=25) (Figure 3.2d). The RMSE and MAE for simulated depth-average velocities with USGS measurements was 0.20 m/s and 0.13 m/s, respectively (n=24). These velocity errors were comparable to the hydrodynamic model validation errors (RMSE of 0.27 m/s, MAE of 0.21 m/s) reported by Czuba et al. (2019) and Sumaiya et al. (2021) and are considered acceptable. Our reported calibration and validation statistics only include the flows that inundate the floodplain (≥28 m^3/s, RI: 1-year) because our analysis is focused on only floodplain-inundating flows.

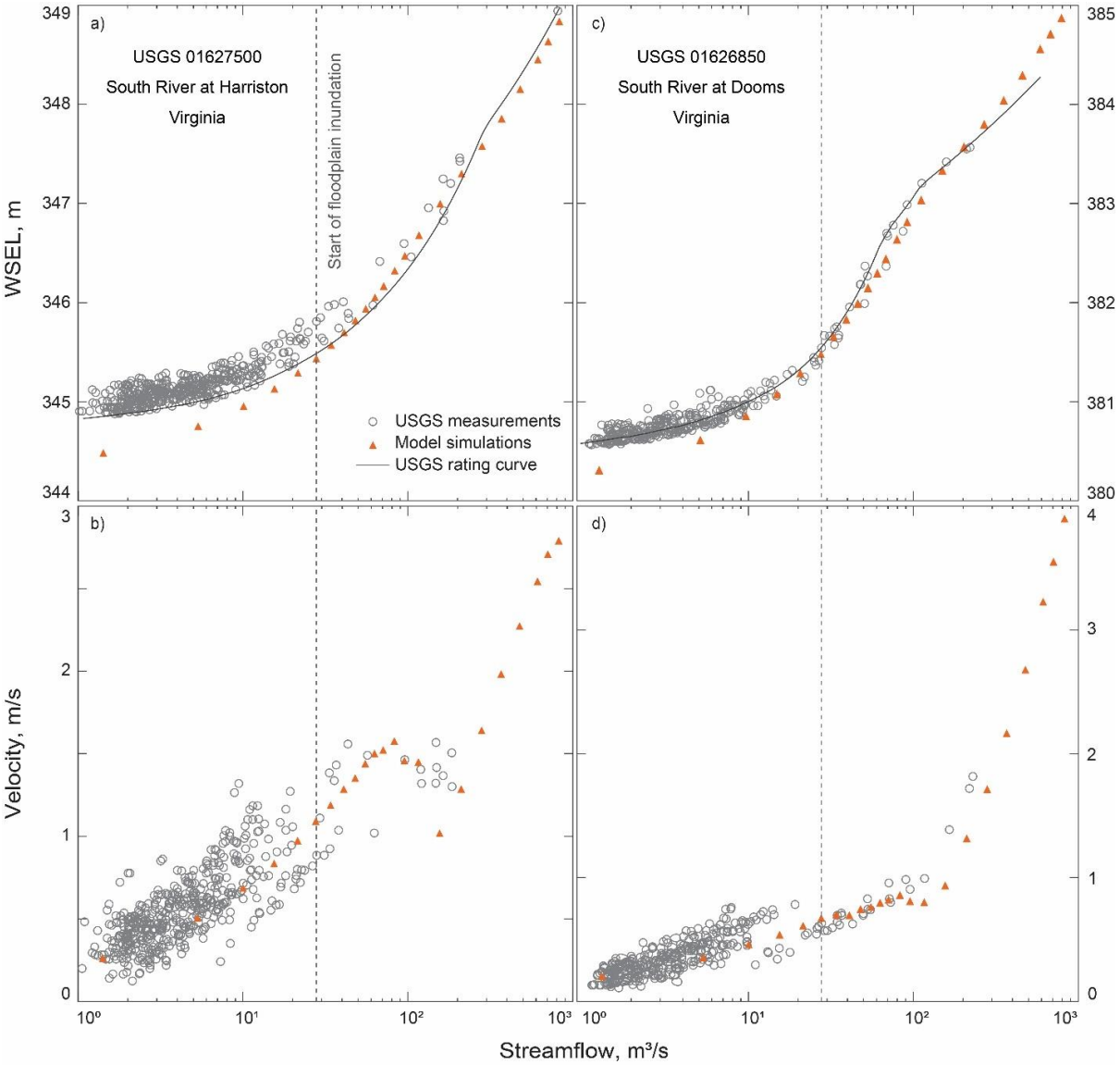

Figure 3.2 Hydrodynamic model calibration and validation at USGS streamflow-gaging stations 01627500 (Harriston) and 01626850 (Dooms) on the South River, Virginia (location shown in Figure 3.1b, red triangle). Water surface elevations (WSEL) relative to flow discharge at Harriston (a) and Dooms (c). Depth-averaged velocities relative to flow discharge at Harriston (b) and Dooms (d). Vertical dash line denotes the first flow inundating the floodplain (28 m^3/s; RI: 1-year).

3.3.2.3 Model outputs

Simulated water depth and depth-averaged velocity (as both x and y components and velocity magnitude) data were the fundamental results used from the 2D HEC-RAS model. The HEC-RAS model computed depth at cell centers and velocity at cell face points and stored the results in a Hierarchical Data Format (HDF) file (Brunner, 2016; Worley et al., 2022). We loaded the HDF file in MATLAB and extracted only the data within AOI and created a 3 × 3 m uniformly spaced mesh grid and interpolated the depth and velocity data to this common grid using the MATLAB griddata function. We calculated bed shear stress at the common grid points from the resistance equation (Garcia, 2008):

$$\tau_b = \rho C_f v^2 \tag{3}$$

where τ_b is the estimated bed shear stress at each common grid cell (Pa), ρ is the water density (kg/m^3), v is the velocity magnitude (m/s), and C_f is the roughness coefficient calculated from the Manning-Strickler form of the logarithmic velocity profile (Garcia, 2008):

$$C_f = [8.1 \left(\frac{H}{k_s}\right)^{\frac{1}{6}}]^{-2} \tag{4}$$

where H is the depth at each grid cell (m), k_s is the effective roughness height (m) proportional to the mean sediment diameter (Brownlie, 1981). The Manning-Strickler form of Manning's roughness coefficient (n) is (Brownlie, 1983):

$$n = \frac{(k_s)^{\frac{1}{6}}}{8.1 g^{\frac{1}{2}}} \tag{5}$$

where g is the gravitational acceleration (m/s^2). Combining Equations (3), (4), and (5), the simplified form of these equations for calculating bed shear stress is:

$$\tau_b = \frac{\rho g n^2 v^2}{H^{\frac{1}{3}}} \tag{6}$$

Calibrated roughness values based on land cover were used in this equation for calculating bed shear stress at the common grid points (with both depth and velocity data).

We generated streamslices in MATLAB from our gridded x and y velocity component data at each flow to aid in visualizing the velocity field. The MATLAB streamslice function draws automatically spaced streamlines from vector data.

3.3.3 Predictor variables of sedimentation rate

3.3.3.1 Flowpath length

A flowpath was generated from each sampling point (Figure 3.1c) at each of the 18 different flows, when inundated, downstream to the river channel using the stream2 function in MATLAB with the gridded x and y velocity components. We also calculated the upstream flowpath, but mention why this was not used in section 3.3.4. Out of the 107 sampling points, only 76 points had complete flowpaths at least at the highest flow. The points at which flowpaths were not generated were either collected in the river bank or outside of the inundation boundary of the highest flow simulated. There were multiple flowpaths at each sampling point, one for every flow that inundated the point, that connected each point downstream to the river channel. We calculated the length of all the individual flowpaths starting from each sampling point and then probabilistically integrated the lengths for each point based on flow recurrence as follows,

$$\text{PFIFL} = \sum_i L_i P_i \tag{7}$$

where, PFIFL is the Probabilistic Flow Integrated flowpath length, L_i is the flowpath length at the ith flow and P_i is the probability of occurrence of the ith flow. Essentially, Equation 7 weights each flowpath length by the probability of that flow occurring when

averaging to a single probabilistic flow integrated flowpath length for each sampling point. Values (here flowpath length) calculated at lower flows are weighted more than those at higher flows when calculating an average value because they have a higher probability of occurrence. This method is similar to the Probabilistic Flow Integrated Grain Size (PFIGS) method described in Sumaiya et al. (2021), which probabilistically integrated a grain size by flow recurrence, and is similar to calculating an effective discharge (Wolman & Miller, 1960), which probabilistically integrates a streamflow by flow recurrence.

3.3.3.2 Exceedance probability of flow

We calculated the exceedance probability (EP) of the flow that first inundates each sampling point using the annual peak flow series (USGS 01627500 South River at Harriston, Virginia, 1925-2021). We also calculated a corresponding recurrence interval (RI) as $RI = \frac{1}{EP}$.

3.3.3.3 Suspended sediment concentration

Suspended sediment concentration (SSC) in the river was estimated for the 18 simulated flows using the sediment rating curve established by Gray (2018) for the South River (USGS stations 1627500 and 1626000) as:

$$SSC = 1.2066\ Q^{0.61433} \tag{8}$$

where SSC is the suspended sediment concentration (mg/l) and Q is the flow discharge in ft^3/s. We determined a single integrated value of SSC for each mercury sampling point by probabilistically integrating the SSC values at and above which the sampling point

was first inundated. This integration followed the same approach as we described for integrating flowpath length as described in section 3.3.1. (Equation 7), but replacing L_i with SSC_i (suspended sediment concentration at ith flow). It is important to note that this suspended sediment concentration is an estimated value in the river channel without any modification for likely settling that would occur with distance across the floodplain.

3.3.3.4 Other parameters considered

We compared many other hydraulic and geomorphic parameters to the measured sedimentation rate data from the South River floodplain. Among all the parameters considered, downstream flowpath length, exceedance probability of flow, and suspended sediment concentration had the highest correlations, which we describe later. Other seemingly relevant parameters that we compared included upstream flowpath length (i.e., the distance from each sampling point upstream to the river channel; r^2 = 0.02, p-value = 0.19); shortest distance from the sample point to the riverbank (r^2 = 0.26, p-value = 3.2e-6); shear stress at each specific flow (highest: r^2 = 0.17, p-value = 1.7e-4; flow: 368 m^3/s, RI= 8.9-years); shear stress and (equivalently in a correlation) shear velocity at the flow first inundating the sampling point (r^2 = 1.6e-3, p-value =0.69), probabilistically integrating shear stress by flow recurrence (r^2 = 0.20, p-value = 3.9e-5), Probabilistic Flow Integrated Grain Size (PFIGS, see Sumaiya et al., 2021) in suspension (r^2 = 0.11, p-value = 2.7e-3) and as bedload (r^2 = 0.14, p-value = 8.3e-4). Additionally, the measured sedimentation rate data were not significantly correlated with the spatial gradient of these hydraulic and geomorphic parameters (such as change in shear stress per cell distance) and the grain size distribution of the floodplain at the sampling point.

3.3.4 Predictive model development

We developed three multiple linear regression models to predict the sedimentation rate along the South River floodplain by applying the MATLAB fitnlm application. The probabilistically integrated downstream flowpath length (section 3.3.1), exceedance probability of the first inundating flow (section 3.3.2), and probabilistically integrated suspended sediment concentration (section 3.3.3) were used as predictor variables. We considered multiple combinations of parameters, but we report out on the best three different multiple linear regression models: Model I, with the only predictor variable of downstream flowpath length; Model II, with predictor variables of downstream flowpath length and exceedance probability of the first inundating flow; and Model III, with predictor variables of downstream flowpath length and suspended sediment concentration.

To assess the multiple linear regression model performance, we computed the p-value, RMSE, coefficient of determination (r^2), and adjusted r^2 of the measured and predicted sedimentation rates (76 samples). A p-value <0.05 indicates statistically significant correlation between predictor variables and the dependent variable. RMSE measures the error of the model, with lower RMSE values indicating less error. In regression models, r^2 is the goodness-of-fit statistic and adjusted r^2 is the corrected goodness-of-fit with higher r^2 values indicating better fit of the model.

3.3.5 Spatial distribution of floodplain sedimentation rate

By applying each of the three multiple linear regression models to the 2D hydrodynamic model results, we created three spatial maps of sedimentation rate within the AOI. From each of these spatial maps we computed the total amount of sediment deposition

in the AOI. Model II and III showed very similar results, and therefore we only show the spatial results of Model I and Model III.

From the spatial maps of sedimentation rate, we also reported the empirical probability distribution function (PDF) and cumulative probability distribution function (CDF) of sedimentation rates spatially within each of three different floodplains (A, B, and C; Figure 3.1c). We expect to learn how floodplain topography affects the spatial pattern and characteristics of floodplain sedimentation. We applied all the available distributions in the MATLAB distributionFitter app to determine the best fit distribution to the empirical sedimentation rate distributions in each of the three floodplains. The distributionFitter app assesses the goodness-of-fit of the distribution computing log likelihood value and standard error (SE). We selected the best fit based on the log likelihood value. The distributions that were best fits included Weibull, Nakagami, Beta, and log-normal.

3.4 Results

3.4.1 Hydrodynamic model simulation results

Simulated water depth (Figure 3a-e; from HEC-RAS) and streamslices (4f-j; generated with MATLAB streamslice) at five representative flow conditions are highlighted here. At the 1.3-year RI flow (83 m^3/s), a few floodplain channels in floodplains A and B (Figure 3.1c) become inundated and connected (Figure 3a). In floodplain C, inundation occurred mostly from backwater flow. There is a roadway at the upstream end of floodplain C (Figure 3.1b) which limits the amount of water conveyed across the floodplain from upstream.

With increasing flow, inundation depths increase in the floodplain with maximum depths in floodplain channels. At a 1.7-year RI flow (116 m3/s) more floodplain channels

become inundated. The streamslices are fairly chaotic at this flow. Much more of the floodplain becomes inundated at the 3.5-year RI flow (280 m^3/s) and streamslices are beginning to organize into a collective floodplain flow direction. Floodplain C is still largely affected by backwater flow while floodplain A more directly conveys floodwaters (Figure 3.3h). Floodplain B has low lying regions similar to floodplain A and higher elevations similar to floodplain C. At the next higher flow (11.5-year RI, 477 m^3/s), most of all three floodplains become inundated except a small high point in floodplain B (Figure 3.3d). Additionally, streamslices are organized into a collective floodplain flow direction across all three floodplains (Figure 3.3i). At the peak of record (824 m^3/s), nearly the entire South River floodplain was inundated with well-organized streamslices (Figure 3.3e, 3.3j).

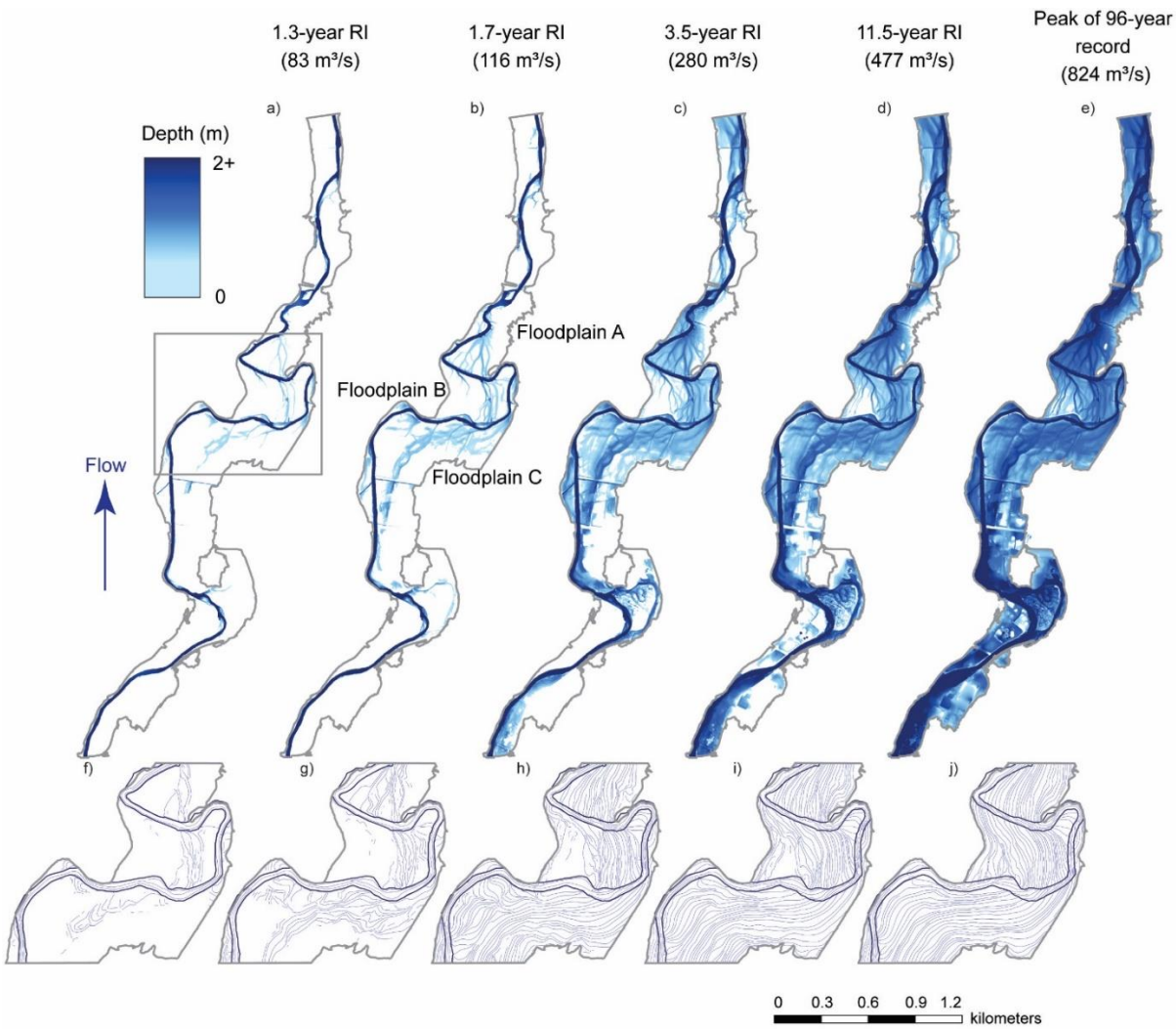

Figure 3.3 Simulated depth (a-e) and streamslices (f-j) for 1.3-year RI flow (a, f; 83 m^3/s), 1.7-year RI flow (b, g; 116 m^3/s), 3.5-year RI flow (c, h; 280 m^3/s), 11.5-year RI flow (d, i; 477 m^3/s), and peak of 96-year record (e, j; 824 m^3/s). The river channel can be seen as the darkest blue line in (a). Gray line is the inundation boundary for the 96-year peak flow. Light gray box in (a) is the extent of streamslices shown in the bottom panels.

Sediment deposition at any location on the floodplain was affected by how frequently these locations became inundated (Figure 3.4a) and the connectivity of that floodplain location with the river (Figure 3.4b). Generally, locations that were inundated more frequently had higher sedimentation rates (Figure 3.4a). Locations proximal to the main channel and floodplain channels with shorter downstream flowpath lengths and that were inundated at 1 to 2-year RI flows had the highest sedimentation rates. Most of the floodplain with lower sedimentation rates were inundated at flows higher than the 2-year RI flow and had longer downstream flowpath lengths.

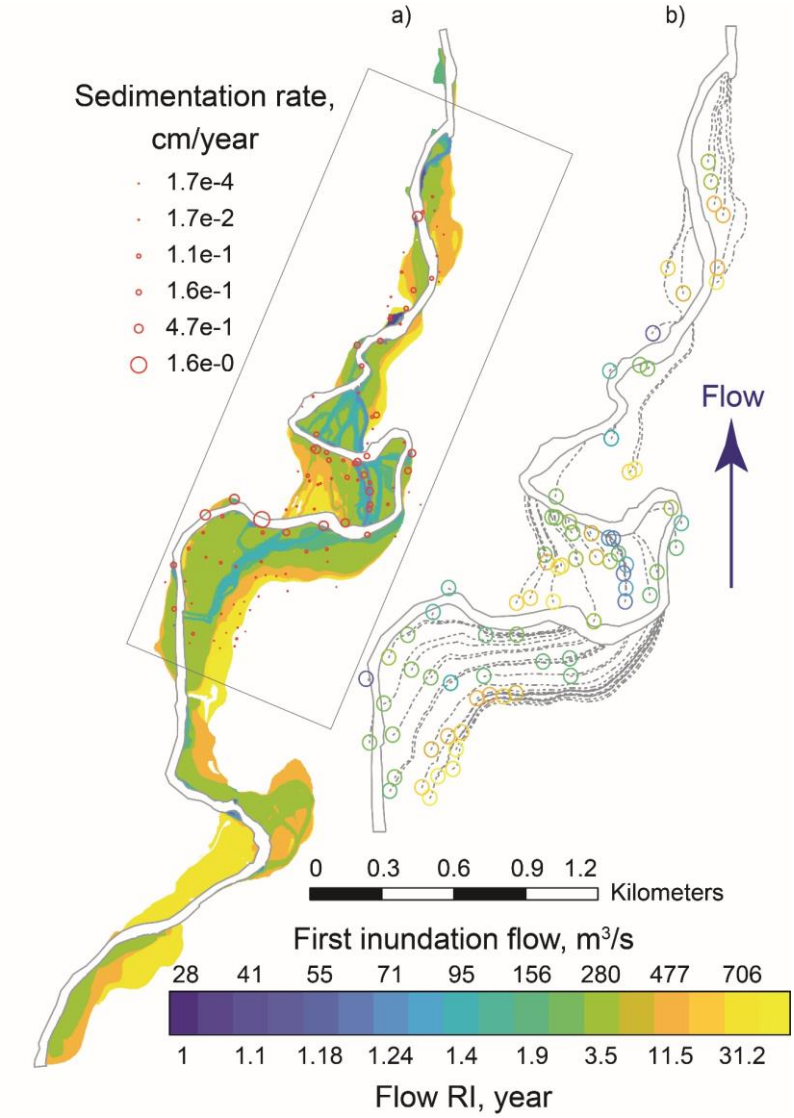

Figure 3.4 Frequency of inundation and river-floodplain connectivity. (a) First flow that inundates the floodplain and corresponding flow recurrence interval (RI). Dark blue is the start of floodplain inundation (vertical dash line at Figure 3.2; 28 m^3/s, RI: 1-year). Sizes of the orange circles represent the sedimentation rate with larger circles indicating higher rates (Pizzuto et al., 2016, 2022). Gray lines denote the channel-floodplain boundary following the high points along the channel banks. (b) Circles represent the sampling points with generated flowpaths (gray lines) at the highest flow (824 m^3/s; peak of 96-year record). Colors of the circles correspond to the first flow that inundates this location, same as in a).

3.4.2 Multiple linear regression models to predict sedimentation rate

Our best three multiple linear regression models (Table 1) included: Model I, with the only predictor variable of downstream flowpath length (m); Model II, with predictor variables of downstream flowpath length (m) and exceedance probability of the first inundating flow (years-1); and Model III, with predictor variables of downstream flowpath length (m) and suspended sediment concentration (mg/l). The flowpath length coefficient ***b*** was in a negative exponential form in all three models (Table 1) indicating that sedimentation rate decreased exponentially as the flowpath length increased.

Model I, with only flowpath distance as the predictor variable, was the simplest of the three multiple linear regression models that we reported. It had a substantially higher r^2 value of 0.59 (Table 1, Figure 3.5a) compared to the other single parameters that were considered, all with r^2 values ≤0.26 (see section 3.3.4). Both Model II and III were improvements over Model I, with r^2 values of 0.66 and 0.67 by incorporating either the exceedance probability (EP) of the first inundating flow or the probabilistic flow integrated suspended sediment concentration (SSC), respectively (Table 1; Figure 3.5b, 5c). Model II and III were marginally different, but Model III was the best performing overall with the highest r^2 value and lowest p-value (Table 1). Combining all three of these parameters into one multiple linear regression (not shown) reduced model performance (r^2 = 0.66). This likely occurred because, when we calculated the probabilistic flow integrated suspended sediment concentration, that calculation incorporated the exceedance probability of the flow. Therefore, the exceedance probability of the flow was essentially double counted (multicollinearity) and ultimately reduced the predictive ability of the resulting multiple linear regression model.

Table 3.2: Three multiple linear regression model equations, coefficient values, p-values, RMSE, r^2, and adjusted r^2 for predicting the sedimentation rate on the floodplain of the South River, Virginia, in the vicinity of the USGS gage at Dooms. Variable definitions: SR, sedimentation rate (cm/year); x, probabilistic flow integrated flowpath length (m); EP, exceedance probability of the first inundating flow (years^{-1}); and SSC, probabilistic flow integrated suspended sediment concentration (mg/l).

	Equation	p-value	RMSE (cm/year)	r^2	Adjusted r^2
Model I	$\boldsymbol{SR = a \times exp^{-bx}}$ $\boldsymbol{a}$ = 0.2238 $\boldsymbol{b}$= 0.0030108	2.6e-15	0.1	0.59	0.294
Model II	$\boldsymbol{SR = a \times exp^{-bx} \times EP^{c}}$ $\boldsymbol{a} =$ 0.26811 $\boldsymbol{b} =$ 0.0022555 $\mathbf{c} =$ 0.3457	4.2e-18	0.1	0.66	0.325
Model III	$\boldsymbol{SR = a \times exp^{-bx} \times SSC^{c}}$ $\boldsymbol{a} =$ 0.0054971 $\boldsymbol{b} =$ 0.0022077 $\mathbf{c} =$ 0.68917	1.4e-18	0.1	0.67	0.33

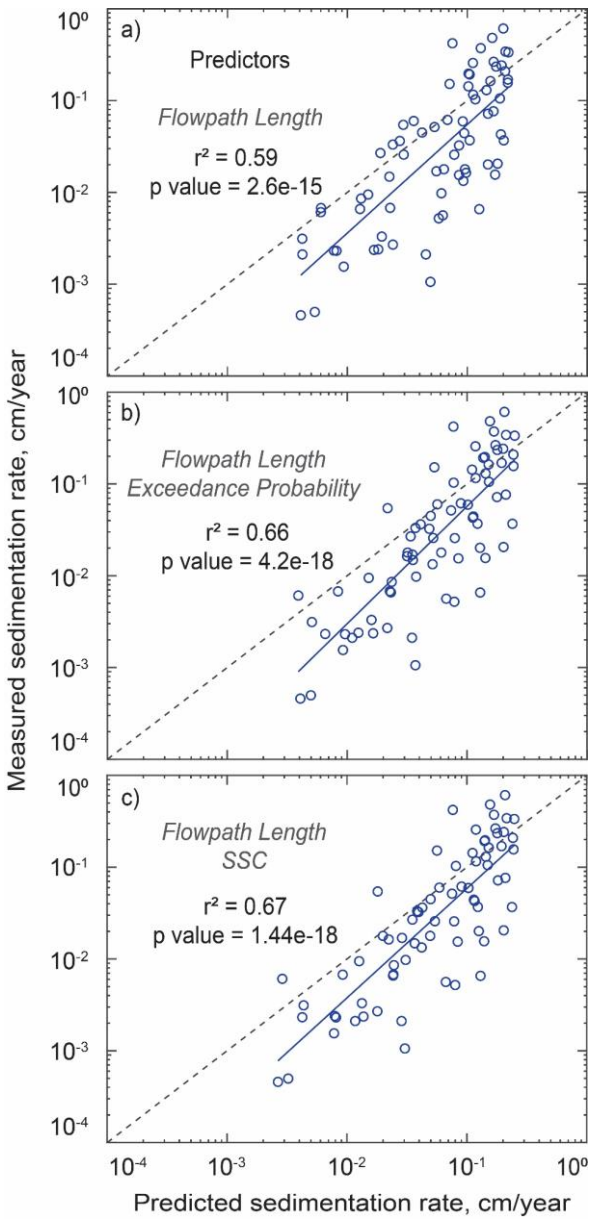

Figure 3.5 Performance of the three multiple linear regression models in predicting the sedimentation rate on the South River floodplain near the USGS gage at Dooms. (a) Model I: downstream flowpath length is the only predictor variable (b) Model II: downstream flowpath length and exceedance probability of flow are the predictor variables. (c) Model III: downstream flowpath length and suspended sediment concentration (SSC) are the predictor variables.

3.4.3 Spatial pattern of sedimentation on the floodplain

To visualize how our multiple linear regression models map to spatial patterns of sedimentation rate, we applied our multiple linear regression model equations to our 2D HEC-RAS results within the AOI (Figure 3.6). Model I predicted that the highest deposition would occur closest to the channel and then decrease exponentially upstream (Figure 3.6a) because the model was only based on the flowpath distance from the sampling point downstream to the channel (or equivalently, the flowpath distance from the river channel upstream to the sampling point). Model II and III additionally included inundation frequency and suspended sediment concentration, respectively, and show high deposition in frequently inundated floodplain channels (Figure 3.6b). We show the results of Model III (Figure 3.6b) because the spatial pattern shown by Model II was very similar to Model III and Model III performed slightly better than Model II (Table 1). The combination of the using 0.76 m lidar data with a 2D HEC-RAS model and applying Model III, we were able to describe the fine scale differences in deposition, primarily in and between floodplain channels (Figure 3.6b).

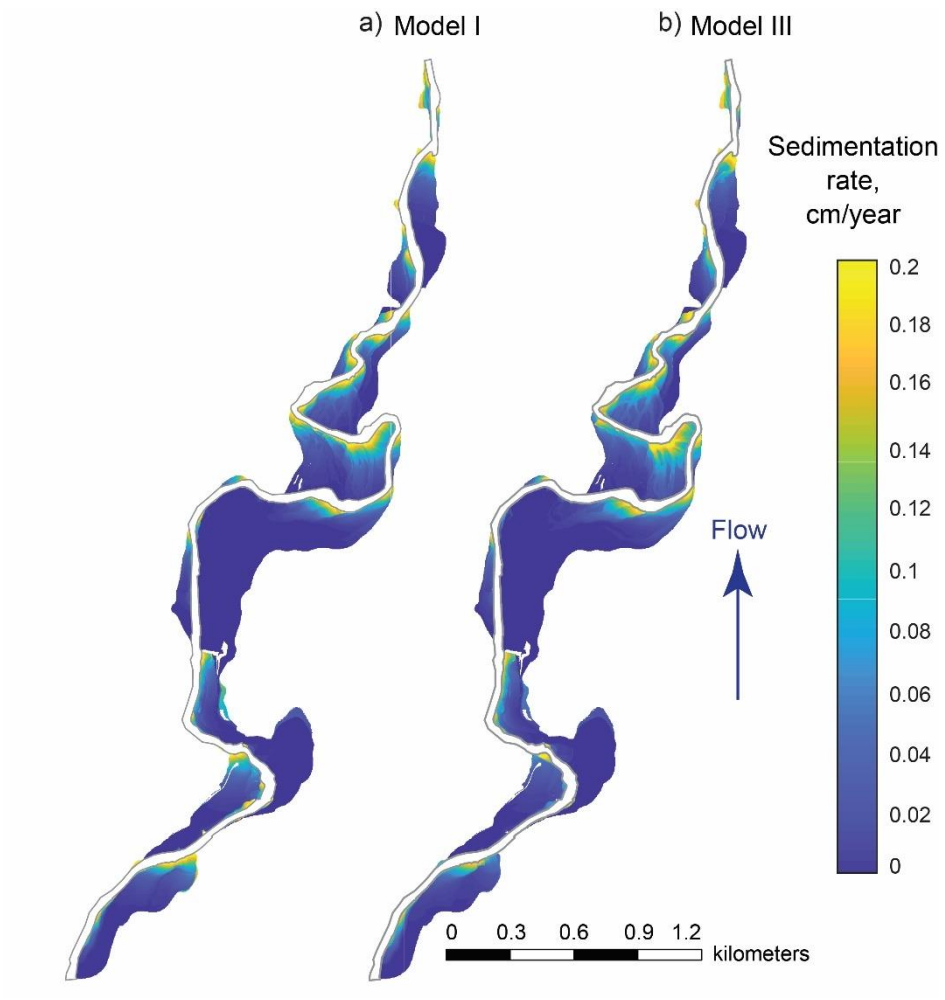

Figure 3.6 Estimated sedimentation rate (cm/year) applying multiple linear regression Model I (a) and Model III (b). For Model I (a), downstream flowpath length was the only predictor variable and for Model III (b), downstream flowpath length and suspended sediment concentration were used as predictor variables. Gray lines denote the boundary of the river and floodplain along the highest points on the channel banks. Results from Model II are not shown because they are similar to those from Model III (b).

The upstream-most section of our AOI is in Waynesboro, which is highly developed, with parking lots, many buildings, a wastewater treatment plant, and other modifications. Furthermore, there is an abandoned meander channel at the first significant strong bend, where the floodplain shows a large “bulge” off to the east. These locations are outside of the extent of the measurements we used and without further analysis, we cannot be certain of the accuracy of these predictions. Finally, there is an area of the AOI near North Park that has already been remediated, with a long section of the bank redesigned and hardened, however, our lidar data predates this remediation effort.

From these spatial results, we then estimated the average sedimentation rate in the 1.63 km^2 area of the AOI. The average sedimentation rate between 1930 and 2007 throughout the AOI was 0.08, 0.08, and 0.07 cm/year from Model I, II, and III, respectively. The spatial map of sedimentation rate (Figure 3.6b) shows that most of the deposited sediment is concentrated near the river channel and in low lying areas of the floodplain that are frequently inundated. From this spatial map (Figure 3.6b), we have quantified the percentage of the total amount of sediment that has deposited if we first start by targeting the areas with the highest amounts of sedimentation and then expanding to areas with lower amounts (Figure 3.7). We estimated that, 11%, 25%, 40%, 66%, and 80% of the sediment deposited in only 3.5%, 9%, 15%, 31%, and 45% of the floodplain area (Figure 2.7).

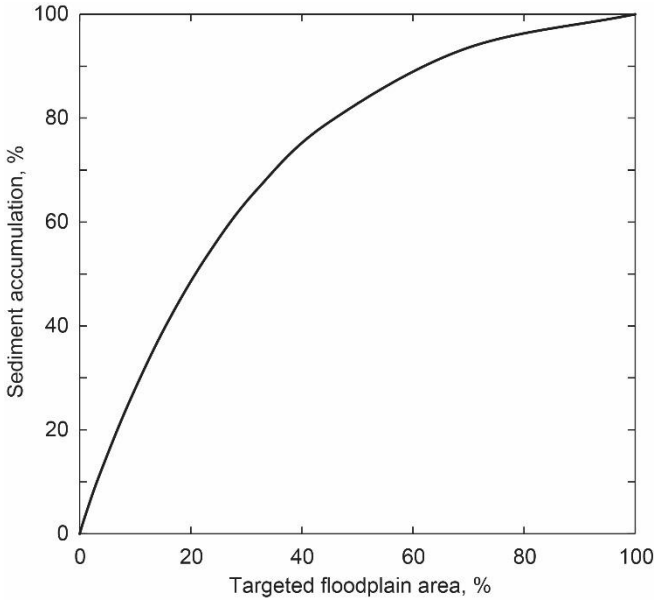

Figure 3.7 Percentage of the total amount of sedimentation relative to the percentage of area targeted if first starting in the areas with the highest amounts of sedimentation and then expanding to areas with lower amounts.

From our spatial maps of sedimentation rate (Figure 3.6), we next analyzed the spatial distributions of sedimentation rate within three physically distinct floodplains. Specifically, we show the empirical probability distribution function (PDF) and cumulative distribution function (CDF) for each of three floodplains, A, B, and C (Figure 3.1c) and for results from Models I and III (Figure 3.8). We also fitted statistical distributions to the empirical data.

The PDFs of Model I (upstream distance only) in floodplains A and B are the closest to a Gaussian distribution (Weibull and Beta as the best fits; Figure 2.8a, b). However, the PDFs of Model III for these same floodplains are bimodal with more skew. Here the best fit is the Nakagami distribution (a special form of the Gamma distribution) for both floodplains although these are not very good fits because of the bimodal nature of the data. We applied the statistical fits to help guide the eye rather than definitively state that the data follow a specific distribution. The first mode of these bimodal distributions is narrow with rates less

than 0.05 cm/year (Figure 2.8a, b) and represents the floodplain areas away from the river channel that are less frequently inundated (dark blue areas in Figure 3.6b). The second mode is wide with sedimentation rates between 0.05 and 0.2 cm/year with the peak of this mode around 0.1 cm/year (Figure 2.8a, b). This second mode represents deposition near the river channel and in low-lying areas of the floodplain that are frequently inundated. The presence of topographic relief in the floodplain seems necessary to strongly realize this second mode. For instance, the PDFs of Models I and III in floodplain C both shows heavy tailed right skewed empirical distributions that are best fit with a log-normal distribution (Figure 2.8c). Because floodplain C is generally flatter with less distinct floodplain channels (Figure 3.1c) and becomes inundated almost uniformly (Figure 3.4) compared to floodplains A and B, the higher deposition rates that characterize the second mode do not occur.

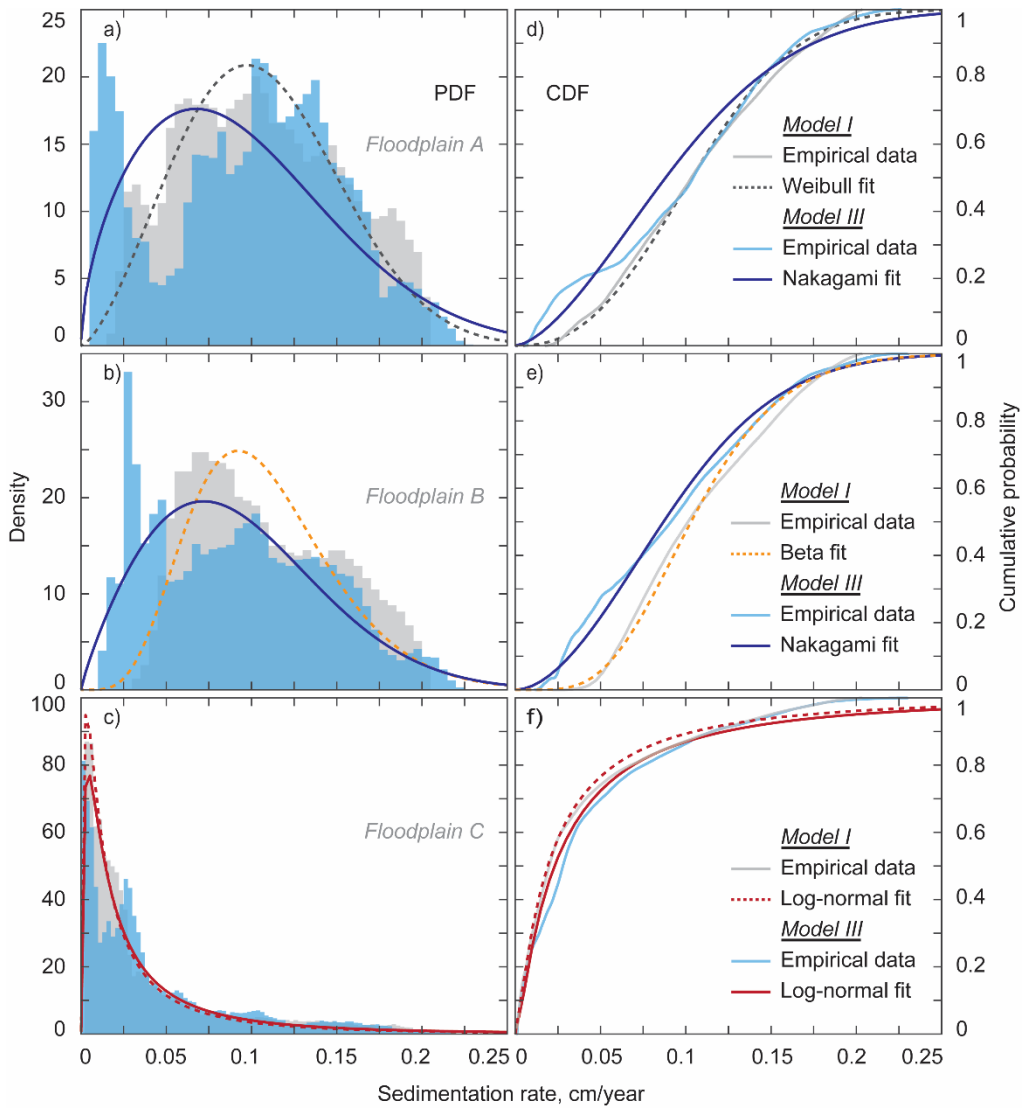

Figure 3.8 Probability distributions of sedimentation rates taken from values spatially across three floodplains along the South River (extent of each floodplain is shown in Figure 3.1c as an orange line and marked as floodplain A, B, C). Probability density function (PDF) and cumulative distribution function (CDF) for floodplain A (a, d), B (b, e), and C (c, f). Gray shaded areas and solid lines indicate the empirical data from Model I and light blue shaded areas and solid lines indicate the empirical data from Model III. Dark blue line is the Nakagami fit for floodplain A (a, d) and B (b, e) for Model III. Black dashed line (a, d) is the Weibull fit and yellow dashed line (b, e) is the Beta fit for Model I. Red solid and dashed line is the log-normal fit for Model I and Model III, respectively, for floodplain C.

3.5 Discussion

We constructed a 2D hydrodynamic model of the South River, Virginia, and combined simulation results with the sedimentation rate data from Pizzuto et al. (2016) into predictive multiple linear regression models describing sedimentation across the floodplain. We developed three multiple linear regression models (Table 1) using variables with the highest predictive capacity that included the probabilistically integrated downstream flowpath length (section 3.3.1), exceedance probability of the first inundating flow (section 3.3.2), and the probabilistically integrated suspended sediment concentration (section 3.3.3). The resulting form of the regression equations and coefficients with flowpath distance raised to a negative exponential (Table 1) indicates that the sedimentation rate decreased exponentially away from the river channel. This finding was consistent with previous literature describing exponential decay of floodplain deposition rates progressing away from the river channel by turbulent diffusion (Allen, 1985; James, 1985; Pizzuto, 1987), advection (Lauer & Parker, 2008; Pizzuto et al., 2008), and from field observations of fine-grained sediment deposition on relatively flat floodplain topography (Allison et al., 1998; Middelkoop & Asselman, 1998; Walling & He, 1998). Additionally, the positive exponent values on exceedance probability and suspended sediment concentration (Table 1) indicate that the sedimentation rate was higher in areas that are inundated more frequently (Liu et al., 2019; Saint-Laurent et al., 2010).

Our multiple linear regression Model I used downstream flowpath length (distance along a streamline starting at a point in the floodplain, proceeding in the downstream direction, and ending at the river) as the only predictor variable (Table 1, Figure 3.5a). Downstream flowpath length was the most predictive distance variable ($r^2 = 0.59$), more so than the upstream flowpath length (distance along a streamline starting at a point in the

floodplain, proceeding in the upstream direction, and ending at the river; $r^2 = 0.02$), maximum/minimum of both distances, and the shortest distance to the riverbank ($r^2 = 0.26$). This means that the distance over the floodplain upstream of the riverbank (which corresponds to downstream flowpath length) is more predictive of sediment deposition than the distance over the floodplain downstream of the riverbank (which corresponds to upstream flowpath length) for the South River. This suggests that sediment along our study reach of the South River may have been deposited primarily via backwater from the river channel (water pushing upstream) rather than from flow spilling out of the river into the floodplain (water moving downstream across the floodplain).

While downstream flowpath length was the variable with the single greatest predictive ability, we know that other hydro-morphodynamic parameters should also influence sedimentation and further improve regression model performance. For instance, sediment deposition on floodplains increases with flood magnitude and duration (Lambert & Walling, 1987; Heitmuller et al., 2017; Liu et al., 2019; Middelkoop & Asselman, 1998; Toonen et al., 2015). After additionally including flood frequency (via the exceedance probability of the first flow that inundates each point on the floodplain; Model II, Table 1, Figure 3.5b), we improved our regression model performance considerably ($r^2 = 0.66$). Furthermore, during these floods the sediment suspended in the river is carried across the floodplain and settles out of suspension (Sumaiya et al., 2021). Quantifying the portion of the suspended sediment load in a river that is conveyed overbank and deposited on floodplains has been used to estimate floodplain sedimentation rates (Lambert & Walling, 1987; Narinesingh et al., 1999; Nicholas et al., 2006). Therefore, by further incorporating suspended sediment concentration (with flood frequency implicit in the calculation, see section 3.3.3) as a predictor variable, we found our best-performing regression model (Model III, $r^2 = 0.67$; Table 1, Figure 3.5c). In all of these models, we incorporated hydrologic

flowpaths as an explicit measure of river-floodplain connectivity that improved our predictions of floodplain sediment deposition compared to the other parameters considered in section 3.3.4.

We created a spatial map with our best prediction for sedimentation rates (Figure 3.6b) along our study reach by applying our best multiple linear regression model (Model III, Table 1, Figure 3.5c) to our 2D hydrodynamic model results (Figure 3.4). Over our study area (AOI) of the South River in Virginia, we estimated an average sedimentation rate of 0.05 cm/year, with maximum values of 0.27 cm/year. In analyzing the sedimentation rates at sample points directly, Pizzuto et al. (2016) reported an average sedimentation rate of 0.025 cm/year with median sedimentation rates of 0.038 cm/year, 0.0137 cm/year, 0.004 cm/year, and 0.001 cm/year for areas in the <0.3-year floodplain, 0.3- to 2-year floodplain, 2- to 5-year floodplain, and 5- to 62-year floodplain, respectively. More recently, Pizzuto et al. (2022) compiled data from rivers in the Mid-Atlantic (including from the South River) and reported that modern sediments (1950–present) accumulated at a median rate of 0.25 cm/year. Our model predicted floodplain sedimentation rates similar to the findings of Pizzuto et al. (2022) because we effectively calibrated the Pizzuto et al. (2016) rates to the Pizzuto et al. (2022) rates (see section 3.1). However, our model predictions appear to be underestimating the largest sedimentation rates by a factor of two (see the cloud of points with the largest rates relative to the curve fit in Figure 3.5).

Our results show that floodplain topography is a strong controlling factor in establishing the spatial distribution of sedimentation rates (Figure 3.1c, 4, 6b). Low-lying areas along the South River, such as floodplain channels, are inundated frequently, affect flow hydraulics, and experience high sediment deposition rates (Büttner et al., 2006). However, some well-developed floodplain channels have been shown to be likely net erosional (Sumaiya et al., 2021). Within our study area, floodplains A and B have well

connected floodplain channels which were inundated more frequently with greater inundation depths than floodplain C (Figure 3.4). Floodplain C is fairly flat with less topographic variation than the other floodplains and was affected more strongly by backwater flow. As a result, floodplains A and B have wider PDFs of sedimentation rate (best fit by a Nakagami distribution, special form of the Gamma distribution) that are bimodal with the one mode occurring at values less than 0.05 cm/year and another mode occurring between 0.05 and 0.2 cm/year with a peak of this mode around 0.1 cm/year (Figure 3.8a, b). This wider second mode represents deposition near the river channel and in low-lying areas of the floodplain that are frequently inundated. Floodplain C has a log-normal PDF of sedimentation rate with most values less than 0.05 cm/year (Figure 3.8c). The absence of major topographic relief in floodplain C seems to preclude a wider distribution of sedimentation rates compared with floodplains A and B.

Ideally, we would like to determine what specific characteristics of the floodplain topography best explain the PDFs of sedimentation rate (Middelkoop & Asselman, 1998; Nicholas & Mitchell, 2003; Nicholas & Walling, 1997, 1998). However, for our study, we have only investigated three distinct floodplains and would need spatial maps of sedimentation rates for many more floodplains. This is possible with our current 2D hydrodynamic model results that extend from Waynesboro to Port Republic, Virginia (48 km reach; Figure 3.1b), but was beyond the scope of the present study. Doing so may also require including distance downstream of Waynesboro as one of the predictive variables in an updated multiple linear regression model (Pizzuto, 2014, Pizzuto et al., 2014). Knowing more about how the subtle floodplain topographic relief affects the spatial pattern of sedimentation is important for more accurately determining the floodplain component of sediment budget models (Dunne et al., 1998; Fryirs & Brierley, 2001; Goodbred & Kuehl, 1998; Malmon et al., 2002; Nicholas et al., 2006; Park, 2020).

Our spatial map of sedimentation rate shows that most of the deposited sediments are concentrated in hotspots near the river channel and in low lying areas of the floodplain that are frequently inundated (Figure 3.6b). We estimated that 80% of the sediment has deposited on only 45% of the South River floodplain (Figure 3.7). The results of our work better inform how floodplain topography and river-floodplain connectivity affects sedimentation rates and can help inform the development of floodplain sediment budgets.

3.6 Concluding remarks

We combined results from a 2D hydrodynamic model of the South River, Virginia, with sedimentation rate data from Pizzuto et al. (2016) into predictive multiple linear regression models describing sedimentation across the floodplain. Downstream flowpath length, exceedance probability of the first inundating flow, and suspended sediment concentration were identified as the dominant predictor variables describing sedimentation rate on the floodplain of the South River downstream of Waynesboro, Virginia. Sedimentation rate decreased exponentially with increasing flowpath distance, measured upstream of the river channel, and increased with inundation frequency and suspended sediment concentration. Our best multiple linear regression model to estimate the sedimentation rate incorporated downstream flowpath length and suspended sediment concentration (with flow exceedance implicit in our calculation) with an r^2 goodness-of-fit statistic of 0.67. In all of these models, we incorporated hydrologic flowpaths as an explicit measure of river-floodplain connectivity that improved our predictions of floodplain sediment deposition compared to the other parameters considered.

Next, we created a spatial map describing sedimentation rates along our study reach by applying our best multiple linear regression model to our 2D hydrodynamic model results.

Floodplains with variable topography leading to low-lying areas, such as floodplain channels, that were inundated frequently had wider PDFs of sedimentation rate that were bimodal with the one mode occurring at values less than 0.05 cm/year and another mode occurring between 0.05 and 0.2 cm/year with a peak of this mode around 0.1 cm/year. This wider second mode represents deposition near the river channel and in low-lying areas of the floodplain that are frequently inundated. In the absence of major topographic relief, another floodplain had a log-normal PDF of sedimentation rate with most values less than 0.05 cm/year. Our estimated average sedimentation rate (0.05 cm/year) between 1930 and 2007 was strongly dominated by this large flat relief floodplain.

Most of the deposited sediment is concentrated near the river channel and in low lying areas of the floodplain that are frequently inundated. We have estimated that 80% of the sediment deposited on 45% of the floodplain area just downstream of Waynesboro, Virginia. In the future, the approach we applied in three floodplains can be extended to the rest of the South River to compile more data relating floodplain topographic variability to spatial distributions of sedimentation rate to better inform the development of floodplain sediment budgets.

References for Chapter 3

Wijesiri, B., Egodawatta, P., McGree, J., Goonetilleke, A., 2015. Influence of pollutant build-up on variability in wash-off from urban road surfaces. Sci. Total Environ. 527–528, 344–350. https://doi.org/10.1016/j.scitotenv.2015.04.093

Ahilan, S., Guan, M., Sleigh, A., Wright, N., & Chang, H. (2018). The influence of floodplain restoration on flow and sediment dynamics in an urban river. *Journal of Flood Risk Management, 11,* S986-S1001. doi: 10.1111/jfr3.12251

Allen, J. R. L. 1985. Principles of Physical Sedimentology. George Allen and Unwin, London.

Allison, M. A., Kuehl, S. A., Martin, T. C., & Hassan, A. (1998). Importance of flood-plain sedimentation for river sediment budgets and terrigenous input to the oceans: Insights from the Brahmaputra-Jamuna River. *Geology, 26* (2), 175–178. doi: https://doi.org/10.1130/0091-7613(1998)026<0175:IOFPSF>2.3.CO;2

Allmendinger, N. E., Pizzuto, J. E., Moglen, G. E., & Lewicki, M. (2007). A sediment budget for an urbanizing watershed, 1951-1996, Montgomery County, Maryland, USA 1. *JAWRA Journal of the American Water Resources Association, 43*(6), 1483-1498. https://doi.org/10.1111/j.1752-1688.2007.00122.x

Alsdorf, D. E., Rodríguez, E., & Lettenmaier, D. P. (2007). Measuring surface water from space. Reviews of Geophysics, 45(2). https://doi.org/10.1029/2006RG000197

Amoros, C., & Bornette, G. (2002). Connectivity and biocomplexity in waterbodies of riverine floodplains. *Freshwater biology*, 47(4), 761-776. https://doi.org/10.1046/j.1365-2427.2002.00905.x

Anees, M. T., Abdullah, K., Nawawi, M. N. M., Ab Rahman, N. N. N., Piah, A. R. M., Zakaria, N. A., ... & Omar, A. M. (2016). Numerical modeling techniques for flood analysis. *Journal of African earth sciences, 124*, 478-486. https://doi.org/10.1016/j.jafrearsci.2016.10.001

Asselman, N. E., & van Wijngaarden, M. (2002). Development and application of a 1D floodplain sedimentation model for the River Rhine in The Netherlands. *Journal of Hydrology, 268*(1-4), 127-142. https://doi.org/10.1016/S0022-1694(02)00162-2

Bates, P. D., Anderson, M. G., Baird, L., Walling, D. E., & Simm, D. (1992). Modelling floodplain flows using a two-dimensional finite element model. *Earth surface processes and landforms, 17*(6), 575-588.

Bates, P. D., Horritt, M. S., Hunter, N. M., Mason, D., & Cobby, D. (2005). Numerical modelling of floodplain flow. *Computational Fluid Dynamics: Applications in Environmental Hydraulics,* 271-304.

Belmont, P., Gran, K. B., Schottler, S. P., Wilcock, P. R., Day, S. S., Jennings, C., ... & Parker, G. (2011). Large shift in source of fine sediment in the Upper Mississippi River. *Environmental science & technology, 45*(20), 8804-8810.

https://doi.org/10.1021/es2019109

Benjankar, R., Egger, G., Jorde, K., Goodwin, P., & Glenn, N. (2011). Dynamic floodplain vegetation model development for the Kootenai River, USA. *Journal of Environmental Management*, 92(12), 3058–3070. https://doi.org/10.1016/j.jenvman.2011.07.017

Benjankar, R., & Yager, E. M. (2012). The impact of different sediment concentrations and sediment transport formulas on the simulated floodplain processes. *Journal of Hydrology, 450,* 230-243. https://doi.org/10.1016/j.jhydrol.2012.05.009

Bracken, L. J., Turnbull, L., Wainwright, J., & Bogaart, P. (2015). Sediment connectivity: a framework for understanding sediment transfer at multiple scales. *Earth Surface Processes and Landforms,* 40(2), 177-188. https://doi.org/10.1002/esp.3635

Brinke, W. B., Schoor, M. M., Sorber, A. M., & Berendsen, H. J. (1998). Overbank sand deposition in relation to transport volumes during large-magnitude floods in the Dutch sand-bed Rhine river system. *Earth Surface Processes and Landforms: The Journal of the British Geomorphological Group, 23*(9), 809-824. https://doi.org/10.1002/(SICI)1096-9837(199809)23:9%3C809::AID-ESP890%3E3.0.CO;2-1

Brown, A. G. (1996). Floodplain palaeoenvironments. *Floodplain processes,* 95-138.

Brownlie, W. R. (1983). Flow depth in sand-bed channels. *Journal of Hydraulic Engineering, 109*(7), 959-990.

Brownlie, W. R. (1981). Prediction of flow depth and sediment discharge in open channels. Report No KH-R-43A, Keck Laboratory of Hydraulics and Water Resources, California Institute of Technology, Pasadena, California.

Brunner, G. W. (2016). *HEC-RAS river analysis system, 2D modeling user's manual version 5.0. (Rep. CPD-68A).* Davis, CA: U.S. Army Corps of Engineers.

Bruzzesi, M.A., Singh, I.L., Gutterman, M., (2007). Final soil, groundwater, and surface water assessment report — GENICOM facility/Schifflet property, Waynesboro, VA. Unpublished Technical Report, ICOR, Ltd., 499

Büttner, O., Otte-Witte, K., Krüger, F., Meon, G., & Rode, M. (2006). Numerical modelling of floodplain hydraulics and suspended sediment transport and deposition at the event scale in the middle river Elbe, Germany. *Acta hydrochimica et hydrobiologica, 34*(3), 265-278. DOI 10.1002/aheh.200500626

Byrne, C. F., Stone, M. C., & Morrison, R. R. (2019). Scalable flux metrics at the channel-floodplain interface as indicators of lateral surface connectivity during flood events. *Water Resources Research,* 55(11), 9788-9807. https://doi.org/10.1029/2019WR026080

Carter, L. (1977). Chemical Plants Leave Unexpected Legacy for Two Virginia Rivers Author (s): Luther J . Carter Published by : American Association for the Advancement of Science Stable URL : http://www.jstor.org/stable/1745339 . *Science, 198*(4321), 1015–1020.

Chen, Y., Overeem, I., Kettner, A. J., Gao, S., Syvitski, J. P., & Wang, Y. (2019).

Quantifying sediment storage on the floodplains outside levees along the lower Yellow River during the years 1580–1849. *Earth Surface Processes and Landforms, 44*(2), 581-594. https://doi.org/10.1002/esp.4519

Coe, D. E., (2016). Floodplain visualization using lidar-derived relative elevation models. Division of Geology and Earth Resources, www.dnr.wa.gov/geology

Costa, J. E. (1975). Effects of agriculture on erosion and sedimentation in the Piedmont Province, Maryland. *Geological Society of America Bulletin, 86*(9), 1281-1286.

Covino, T. (2017). Hydrologic connectivity as a framework for understanding biogeochemical flux through watersheds and along fluvial networks. *Geomorphology*, 277, 133-144. https://doi.org/10.1016/j.geomorph.2016.09.030

Czuba, J. A., David, S. R., Edmonds, D. A., & Ward, A. S. (2019). Dynamics of surface-water connectivity in a low-gradient meandering river floodplain. *Water Resources Research, 55*(3), 1849–1870. https://doi.org/10.1029/2018WR023527

David, S. R., Czuba, J. A., & Edmonds, D. A. (2018). Channelization of meandering river floodplains by headcutting. *Geology, 47*(1), 15–18. https://doi.org/10.1130/G45529.1

David, S. R., Edmonds, D. A., & Letsinger, S. L. (2017). Controls on the occurrence and prevalence of floodplain channels in meandering rivers. *Earth Surface Processes and Landforms, 42*(3), 460–472. https://doi.org/10.1002/esp.4002

Du, P., & Walling, D. E. (2012). Using ^{210}Pb measurements to estimate sedimentation rates on river floodplains. *Journal of environmental radioactivity, 103*(1), 59-75. https://doi.org/10.1016/j.jenvrad.2011.08.006

Dunne, T., Mertes, L. A., Meade, R. H., Richey, J. E., & Forsberg, B. R. (1998). Exchanges of sediment between the flood plain and channel of the Amazon River in Brazil. *Geological Society of America Bulletin, 110*(4), 450-467.

Flanders, J. R., Turner, R. R., Morrison, T., Jensen, R., Pizzuto, J., Skalak, K., & Stahl, R. (2010). Distribution, behavior, and transport of inorganic and methylmercury in a high gradient stream. *Applied Geochemistry, 25*(11), 1756–1769. https://doi.org/10.1016/j.apgeochem.2010.09.004

Freeman, M. C., Pringle, C. M., & Jackson, C. R. (2007). Hydrologic connectivity and the contribution of stream headwaters to ecological integrity at regional scales 1. *JAWRA Journal of the American Water Resources Association*, 43(1), 5-14. DOI: 10.1111/j.1752-1688.2007.00002.x

Fryirs, K., & Brierley, G. (2001). Variability in sediment delivery and storage along river courses in Bega catchment, NSW, Australia: Implications for geomorphic river recovery. *Geomorphology, 38*(3-4), 237-265. https://doi.org/10.1016/S0169-555X(00)00093-3

Garcia, M. (Ed.). (2008). Sedimentation engineering: Processes, measurements, modeling, and practice. American Society of Civil Engineers.

Gomez, B., Phillips, J. D., Magilligan, F. J., & James, L. A. (1997). Floodplain sedimentation

and sensitivity: summer 1993 flood, Upper Mississippi River Valley. Earth Surface Processes and Landforms: *The Journal of the British Geomorphological Group, 22*(10), 923-936. 10.1144/GSL.SP.1999.163.01.06

Goodbred Jr, S. L., & Kuehl, S. A. (1998). Floodplain processes in the Bengal Basin and the storage of Ganges–Brahmaputra river sediment: an accretion study using ^{137}Cs and ^{210}Pb geochronology. *Sedimentary Geology, 121*(3-4), 239-258. https://doi.org/10.1016/S0037-0738(98)00082-7

Gray, H. J. I. F. (2018). *Traveling at the Speed of Light Luminescence as a Means to Quantify Sediment Transport* (Doctoral dissertation, University of Colorado at Boulder).

Hardy, R. J., Bates, P. D., & Anderson, M. G. (2000). Modelling suspended sediment deposition on a fluvial floodplain using a two-dimensional dynamic finite element model. *Journal of Hydrology*, 229(3-4), 202-218. https://doi.org/10.1016/S0022-1694(00)00159-1

He, Q., & Walling, D. E. (1996a). Rates of overbank sedimentation on the floodplains of British lowland rivers documented using fallout ^{137}Cs. *Geografiska Annaler: Series A, Physical Geography, 78*(4), 223-234. https://doi.org/10.1080/04353676.1996.11880469

He, Q., & Walling, D. E. (1996b). Use of fallout Pb-210 measurements to investigate longer-term rates and patterns of overbank sediment deposition on the floodplains of lowland rivers. *Earth Surface Processes and Landforms, 21*(2), 141-154. 10.1002/(SICI)1096-9837(199602)21:2<141::AID-ESP572>3.0.CO;2-9

Heitmuller, F. T., Hudson, P. F., & Kesel, R. H. (2017). Overbank sedimentation from the historic AD 2011 flood along the Lower Mississippi River, USA. *Geology, 45*(2), 107-110. https://doi.org/10.1130/G38546.1

Hilldale, R. C., & Raff, D. (2008). Assessing the ability of airborne LiDAR to map river bathymetry. *Earth Surface Processes and Landforms, 33*(5), 773-783. DOI: 10.1002/esp.1575

Hopkins, K. G., Noe, G. B., Franco, F., Pindilli, E. J., Gordon, S., Metes, M. J., ... & Hogan, D. M. (2018). A method to quantify and value floodplain sediment and nutrient retention ecosystem services. *Journal of Environmental Management, 220*, 65-76. https://doi.org/10.1016/j.jenvman.2018.05.013

Horritt, M. S., & Bates, P. D. (2002). Evaluation of 1D and 2D numerical models for predicting river flood inundation. *Journal of hydrology, 268*(1-4), 87-99. https://doi.org/10.1016/S0022-1694(02)00121-X

Hupp, C. R., & Bazemore, D. E. (1993). Temporal and spatial patterns of wetland sedimentation, West Tennessee. *Journal of Hydrology, 141*(1-4), 179-196. https://doi.org/10.1016/0022-1694(93)90049-F

Hupp, C. R., Kroes, D. E., Noe, G. B., Schenk, E. R., & Day, R. H. (2019). Sediment trapping and carbon sequestration in floodplains of the lower Atchafalaya Basin, LA: Allochthonous versus autochthonous carbon sources. *Journal of Geophysical Research: Biogeosciences, 124*(3), 663-677. https://doi.org/10.1029/2018JG004533

Hupp, C. R., & Osterkamp, W. R. (1996). Riparian vegetation and fluvial geomorphic processes. *Geomorphology, 14*(4), 277-295. https://doi.org/10.1016/0169-555X(95)00042-4

Hupp, C. R., Schenk, E. R., Kroes, D. E., Willard, D. A., Townsend, P. A., & Peet, R. K. (2015). Patterns of floodplain sediment deposition along the regulated lower Roanoke River, North Carolina: Annual, decadal, centennial scales. *Geomorphology, 228,* 666-680. https://doi.org/10.1016/j.geomorph.2014.10.023

Jackson, R. G. (1976). Depositional model of point bars in the lower Wabash River. *Journal of Sedimentary Research, 46*(3), 579-594.

James, C. S. (1985). Sediment transfer to overbank sections. *Journal of hydraulic research, 23*(5), 435-452. https://doi.org/10.1080/00221688509499337

Junk, W. J., Bayley, P. B., & Sparks, R. E. (1989). The flood pulse concept in river-floodplain systems. *Canadian special publication of fisheries and aquatic sciences,* 106(1), 110-127.

Karssenberg, D., & Bridge, J. S. (2008). A three-dimensional numerical model of sediment transport, erosion and deposition within a network of channel belts, floodplain and hill slope: Extrinsic and intrinsic controls on floodplain dynamics and alluvial architecture. *Sedimentology, 55*(6), 1717-1745. https://doi.org/10.1111/j.1365-3091.2008.00965.x

Kesel, R. H., Dunne, K. C., McDonald, R. C., Allison, K. R., & Spicer, B. E. (1974). Lateral erosion and overbank deposition on the Mississippi River in Louisiana caused by 1973 flooding. *Geology, 2*(9), 461-464.

Kupfer, J. A., Meitzen, K. M., & Gao, P. (2015). flooding and surface connectivity of Taxodium-Nyssa stands in a southern floodplain forest ecosystem. *River Research and Applications, 31*(10), 1299–1310. https://doi.org/10.1002/rra.2828

Lambert, C. P., & Walling, D. E. (1987). Floodplain sedimentation: a preliminary investigation of contemporary deposition within the lower reaches of the River Culm, Devon, UK. *Geografiska Annaler: Series A, Physical Geography, 69*(3-4), 393-404. https://doi.org/10.1080/04353676.1987.11880227

Lauer, J. W., & Parker, G. (2008). Modeling framework for sediment deposition, storage, and evacuation in the floodplain of a meandering river: Application to the Clark Fork River, Montana. *Water Resources Research, 44*(8), 1–16. https://doi.org/10.1029/2006WR005529

Leopold, L. B. (1973). River channel change with time: an example: address as retiring president of The Geological Society of America, Minneapolis, Minnesota, November 1972. *Geological Society of America Bulletin, 84*(6), 1845-1860.

Lesack, L. F., & Melack, J. M. (1995). Flooding hydrology and mixture dynamics of lake water derived from multiple sources in an Amazon floodplain lake. Water Resources Research, 31(2), 329-345. https://doi.org/10.1029/94WR02271

Lewin, J., & Ashworth, P. J. (2014). The negative relief of large river floodplains. *Earth-Science Reviews, 129,* 1–23. https://doi.org/10.1016/j. earscirev.2013.10.014

Lewin, J., & Hughes, D. (1980). Welsh floodplain studies: II. Application of a qualitative inundation model. *Journal of Hydrology, 46*(1-2), 35-49. https://doi.org/10.1016/0022-1694(80)90034-7

Lindroth, E. M., Rhoads, B. L., Castillo, C. R., Czuba, J. A., Güneralp, İ., & Edmonds, D. (2020). Spatial variability in bankfull stage and bank elevations of lowland meandering rivers: Relation to rating curves and channel planform characteristics. *Water Resources Research, 56*(8), e2020WR027477.

Liu, X. J., Min, F. Y., & Kettner, A. J. (2019). The impact of large to extreme flood events on floodplain evolution of the middle and lower reaches of the Yangtze River, China. *Catena, 176*, 394-409. https://doi.org/10.1016/j.catena.2019.01.027

Maaß, A. L., & Schüttrumpf, H. (2019). Reactivation of Floodplains in River Restorations: Long-Term Implications on the Mobility of Floodplain Sediment Deposits. *Water Resources Research, 55*(10), 8178-8196. https://doi.org/10.1029/2019WR024983

Mahoney, J. M., & Rood, S. B. (1998). Streamflow requirements for cottonwood seedling recruitment—an integrative model. *Wetlands, 18*(4), 634-645. DOI: 10.1007/BF03161678

Malmon, D. V., Dunne, T., & Reneau, S. L. (2002). Predicting the fate of sediment and pollutants in river floodplains. *Environmental Science & Technology, 36*(9), 2026-2032. https://doi.org/10.1021/es010509+

Mertes, L. A. (1997). Documentation and significance of the perirheic zone on inundated floodplains. Water Resources Research, 33(7), 1749-1762. https://doi.org/10.1029/97WR00658

Mertes, L. A., Dunne, T., & Martinelli, L. A. (1996). Channel-floodplain geomorphology along the Solimões-Amazon river, Brazil. *Geological Society of America Bulletin,* 108(9), 1089-1107. https://doi.org/10.1130/0016-7606(1996)108%3C1089:CFGATS%3E2.3.CO;2

Middelkoop, H., & Asselman, N. E. (1998). Spatial variability of floodplain sedimentation at the event scale in the Rhine–Meuse delta, The Netherlands. *Earth Surface Processes and Landforms: The Journal of the British Geomorphological Group, 23*(6), 561-573. https://doi.org/10.1002/(SICI)1096-9837(199806)23:6%3C561::AID-ESP870%3E3.0.CO;2-5

Middelkoop, H., van der Perk, M. (1998). Modelling spatial patterns of overbank sedimentation on embanked floodplains. Geografiska Annaler—S*eries A: Physical Geography, 80*(2), 95–109. https://doi.org/10.1111/j.0435-3676.1998.00029.x

Mizugaki, S., Nakamura, F., & Araya, T. (2006). Using dendrogeomorphology and ^{137}Cs and ^{210}Pb radiochronology to estimate recent changes in sedimentation rates in Kushiro Mire, Northern Japan, resulting from land use change and river channelization. *Catena, 68*(1), 25-40. https://doi.org/10.1016/j.catena.2006.03.014

Moody, J. A. (2019). Dynamic relations for the deposition of sediment on floodplains and point bars of a freely-meandering river. Geomorphology, 327, 585-597.

Naipal, V., Reick, C., Van Oost, K., Hoffmann, T., & Pongratz, J. (2016). Modeling long-term, large-scale sediment storage using a simple sediment budget approach. *Earth Surface Dynamics, 4*(2), 407-423. https://doi.org/10.5194/esurf-4-407-2016

Nakamura, F., Yajima, T., & Kikuchi, S. I. (1997). Structure and composition of riparian forests with special reference to geomorphic site conditions along the Tokachi River, northern Japan. *Plant Ecology, 133*(2), 209-219. https://doi.org/10.1023/A:1009787614455

Nanson, G. C., & Croke, J. C. (1992). A genetic classification of floodplains. *Geomorphology, 4,* 459–486. https://doi.org/https://doi.org/10.1016/0169-555X(92)90039-Q

Narinesingh, P., Klaassen, G. J., & Ludikhuize, D. (1999). Floodplain sedimentation along extended river reaches. *Journal of Hydraulic Research, 37*(6), 827-845. https://doi.org/10.1080/00221689909498514

Nicholas, A. R., & McLelland, S. J. (2004). Computational fluid dynamics modelling of three-dimensional processes on natural river floodplains. *Journal of Hydraulic Research, 42*(2), 131-143. https://doi.org/10.1080/00221686.2004.9628299

Nicholas, A. P., & Mitchell, C. A. (2003). Numerical simulation of overbank processes in topographically complex floodplain environments. *Hydrological Processes, 17*(4), 727-746. https://doi.org/10.1002/hyp.1162

Nicholas, A. P., & Walling, D. E. (1997). Investigating spatial patterns of medium-term overbank sedimentation on floodplains: a combined numerical modelling and radiocaesium-based approach. *Geomorphology, 19*(1-2), 133-150. https://doi.org/10.1016/S0169-555X(96)00043-8

Nicholas, A. P., & Walling, D. E. (1998). Numerical modelling of floodplain hydraulics and suspended sediment transport and deposition. *Hydrological Processes, 12*(8), 1339-1355. https://doi.org/10.1002/(SICI)1099-1085(19980630)12:8%3C1339::AID-HYP618%3E3.0.CO;2-6

Nicholas, A. P., Walling, D. E., Sweet, R. J., & Fang, X. (2006). Development and evaluation of a new catchment-scale model of floodplain sedimentation. *Water Resources Research, 42*(10). https://doi.org/10.1029/2005WR004579

Noe, G. B., Hopkins, K. G., Claggett, P. R., Schenk, E. R., Metes, M. J., Ahmed, L., ... & Hupp, C. R. (2022). Streambank and floodplain geomorphic change and contribution to watershed material budgets. *Environmental Research Letters, 17(6),* 064015. URL/DOI: https://doi.org/10.5066/P93OUWYZ.

Normally, N. R. (1967). Definition and identification of channel and overbank deposits and their respective roles in flood plain formation. *The Professional Geographer, 19*(1), 1-4.. https://doi.org/10.1111/j.0033-0124.1967.00001.x

Park, E. (2020). Characterizing channel-floodplain connectivity using satellite altimetry: Mechanism, hydrogeomorphic control, and sediment budget. *Remote Sensing of Environment, 243,* 111783. https://doi.org/10.1016/j.rse.2020.111783

Park, E., & Latrubesse, E. M. (2019). A geomorphological assessment of wash-load sediment fluxes and floodplain sediment sinks along the lower Amazon River. *Geology, 47*(5), 403-406. https://doi.org/10.1130/G45769.1

Park, E., & Latrubesse, E. M. (2017). The hydro-geomorphologic complexity of the lower Amazon River floodplain and hydrological connectivity assessed by remote sensing and field control. *Remote Sensing of Environment*, 198, 321-332. https://doi.org/10.1016/j.rse.2017.06.021

Pizzuto, J. E. (2014). Long-term storage and transport length scale of fine sediment: Analysis of a mercury release into a river. *Geophysical Research Letters, 41*(16), 5875–5882. https://doi.org/10.1002/2014GL060722

Pizzuto, J. (2012). Predicting the accumulation of mercury-contaminated sediment on riverbanks-an analytical approach. *Water Resources Research, 48*(7), 1–13. https://doi.org/10.1029/2012WR011906

Pizzuto, J. E. (1987). Sediment diffusion during overbank flows. *Sedimentology, 34*(2), 301-317. https://doi.org/10.1111/j.1365-3091.1987.tb00779.x

Pizzuto, J. E., Moody, J. A., & Meade, R. H. (2008). Anatomy and dynamics of a floodplain, Powder River, Montana, USA. *Journal of Sedimentary Research, 78*(1), 16-28.

Pizzuto, J., & O'Neal, M. (2009). Increased mid-twentieth century riverbank erosion rates related to the demise of mill dams, South River, Virginia. *Geology, 37*(1), 19–22. https://doi.org/10.1130/G25207A.1

Pizzuto, J., Schenk, E. R., Hupp, C. R., Gellis, A., Noe, G., Williamson, E., ... & Newbold, D. (2014). Characteristic length scales and time-averaged transport velocities of suspended sediment in the mid-Atlantic Region, USA. *Water Resources Research, 50*(2), 790-805.

Pizzuto, J. E., Skalak, K. J., Benthem, A., Mahan, S. A., Sherif, M., & Pearson, A. J. (2022). Spatially averaged stratigraphic data to inform watershed sediment routing: An example from the Mid-Atlantic United States. *GSA Bulletin.* https://doi.org/10.1130/B36282.1

Pizzuto, J., Skalak, K., Pearson, A., & Benthem, A. (2016). Active overbank deposition during the last century, South River, Virginia. *Geomorphology, 257,* 164–178. https://doi.org/10.1016/j.geomorph.2016.01.006

Rak, G., Kozelj, D., & Steinman, F. (2016). The impact of floodplain land use on flood wave propagation. *Natural hazards, 83*(1), 425-443. https://doi.org/10.1007/s11069-016-2322-0

Remo, J. W., Ryherd, J., Ruffner, C. M., & Therrell, M. D. (2018). Temporal and spatial patterns of sedimentation within the batture lands of the middle Mississippi River, USA. *Geomorphology, 308,* 129-141. https://doi.org/10.1016/j.geomorph.2018.02.010

Remor, M. B., Vilas Boas, M. A., Sampaio, S. C., Damatto, S. R., Stevaux, J. C., & dos Reis, R. R. (2022). Sedimentation rate and accumulation of nutrients in the Upper Paraná river floodplain. *Journal of Radioanalytical and Nuclear Chemistry, 331*(2), 1019–1027. https://doi.org/10.1007/s10967-021-08153-5

Rhoades, E. L., O'Neal, M. A., & Pizzuto, J. E. (2009). Quantifying bank erosion on the South River from 1937 to 2005, and its importance in assessing Hg contamination. *Applied Geography*, *29*(1), 125–134. https://doi.org/10.1016/j.apgeog.2008.08.005

Saint-Laurent, D., Lavoie, L., Drouin, A., St-Laurent, J., & Ghaleb, B. (2010). Floodplain sedimentation rates, soil properties and recent flood history in southern Québec. *Global and Planetary Change, 70*(1-4), 76-91.

Schenk, E. R., Hupp, C. R., Gellis, A., & Noe, G. (2013). Developing a new stream metric for comparing stream function using a bank–floodplain sediment budget: a case study of three Piedmont streams. *Earth Surface Processes and Landforms, 38*(8), 771-784. https://doi.org/10.1002/esp.3314

Shenk, G. W., & Linker, L. C. (2013). Development and application of the 2010 Chesapeake Bay watershed total maximum daily load model. J*AWRA Journal of the American Water Resources Association, 49*(5), 1042-1056. https://doi.org/10.1111/jawr.12109

Skalak, K. J., & Pizzuto, J. (2014). Reconstructing suspended sediment mercury contamination of a steep, gravel-bed river using reservoir theory. *Environmental Geosciences, 21*(1), 17–35. https://doi.org/10.1306/eg.08151313007

Skalak, K., & Pizzuto, J. (2010). The distribution and residence time of suspended sediment stored within the channel margins of a gravel-bed bedrock river. *Earth Surface Processes and Landforms, 35*(4), 435–446. https://doi.org/10.1002/esp.1926

Stone, M. C., Byrne, C. F., & Morrison, R. R. (2017). Evaluating the impacts of hydrologic and geomorphic alterations on floodplain connectivity. *Ecohydrology*, 10(5), e1833.

Sumaiya, S., Czuba, J. A., Schubert, J. T., David, S. R., Johnston, G. H., & Edmonds, D. A. (2021). Sediment transport potential in a hydraulically connected river and floodplain-channel system. *Water Resources Research, 57*, e2020WR028852. https://doi.org/10.1029/2020WR028852

Sutfin, N. A., Wohl, E. E., & Dwire, K. A. (2016). Banking carbon: a review of organic carbon storage and physical factors influencing retention in floodplains and riparian ecosystems. *Earth Surface Processes and Landforms, 41*(1), 38-60. https://doi.org/10.1002/esp.3857

Terry, J. P., Garimella, S., & Kostaschuk, R. A. (2002). Rates of floodplain accretion in a tropical island river system impacted by cyclones and large floods. *Geomorphology, 42*(3-4), 171-182. https://doi.org/10.1016/S0169-555X(01)00084-8

Terry, J. P., Kostaschuk, R. A., & Garimella, S. (2006). Sediment deposition rate in the Falefa River basin, Upolu island, Samoa. *Journal of Environmental Radioactivity, 86*(1), 45-63. https://doi.org/10.1016/j.jenvrad.2005.07.004

Thayer, J. B., & Ashmore, P. (2016). Floodplain morphology, sedimentology, and development processes of a partially alluvial channel. *Geomorphology, 269*, 160–174. https://doi.org/10.1016/j.geomorph.2016.06.040

Tichavský, R., Kluzová, O., Břežný, M., Ondráčková, L., Krpec, P., Tolasz, R., & Šilhán, K. (2018). Increased gully activity induced by short-term human interventions–

Dendrogeomorphic research based on exposed tree roots. *Applied Geography, 98*, 66-77. https://doi.org/10.1016/j.apgeog.2018.07.008

Tockner, K., Malard, F., & Ward, J. V. (2000). An extension of the flood pulse concept. *Hydrological processes*, 14(16-17), 2861-2883. https://doi.org/10.1002/1099-1085(200011/12)14:16/17%3C2861::AID-HYP124%3E3.0.CO;2-F

Toonen, W. H. J., Winkels, T. G., Cohen, K. M., Prins, M. A., & Middelkoop, H. (2015). Lower Rhine historical flood magnitudes of the last 450 years reproduced from grain-size measurements of flood deposits using End Member Modelling. *Catena, 130*, 69-81. https://doi.org/10.1016/j.catena.2014.12.004Törnqvist, T. E., Bridge, J. S., & Asselman, N. E. M. (1996). Quantitative analysis of overbank deposition in the Rhine–Meuse and Mississippi deltas: implications for 3-D modelling of alluvial architecture. In *Proceedings 3e Nederlands Aardwetenschappelijk Congres Veldhoven*, Mei 1996.

Trigg, M. A., Bates, P. D., Wilson, M. D., Schumann, G., & Baugh, C. (2012). Floodplain channel morphology and networks of the middle Amazon River. *Water Resources Research*, 48(10). https://doi.org/10.1029/2012WR011888

Trimble, S. W. (1999). Decreased rates of alluvial sediment storage in the Coon Creek Basin, Wisconsin, 1975-93. *Science, 285*(5431), 1244-1246.

Trimble, S. W. (1983). A sediment budget for Coon Creek basin in the Driftless Area, Wisconsin, 1853-1977. *American Journal of Science, 283*(5), 454-474. https://doi.org/10.2475/ajs.283.5.454

Tull, N., Passalacqua, P., Hassenruck-Gudipati, H. J., Rahman, S., Wright, K., Hariharan, J., & Mohrig, D. (2022). Bidirectional River-Floodplain Connectivity During Combined Pluvial-Fluvial Events. *Water Resources Research, 58(3)*, e2021WR030492.

URS Corp. (2012), Final report: Ecological study of the South River and a segment of the South Fork Shenandoah River, Virginia, p. 1804, Fort Washington, Pa. [Available at www.southriverscienceteam.org/news]

USEPA (2009) United States Environmental Protection Agency, Appendix A. Generic SSLs for the residential and commercial/ industrial scenarios

VGIN (2017). Virginia LiDAR Downloads. Accessed 2 November 2017 at https://www.arcgis.com/home/item.html?id=1e964be36b454a12a69a3ad0bc1473ce

Viparelli, E., Wesley Lauer, J., Belmont, P., & Parker, G. (2013). A numerical model to develop long-term sediment budgets using isotopic sediment fingerprints. *Computers and Geosciences, 53*, 114–122. https://doi.org/10.1016/j.cageo.2011.10.003

Walling, D. E. (1983). The sediment delivery problem. *Journal of hydrology, 65*(1-3), 209-237. https://doi.org/10.1016/0022-1694(83)90217-2

Walling, D. E., & Bradley, S. B. (1989). Rates and patterns of contemporary floodplain sedimentation: a case study of the River Culm, Devon, UK. *GeoJournal, 19*(1), 53-62. https://doi.org/10.1007/BF00620549

Walling, D. E., & He, Q. (1998). The spatial variability of overbank sedimentation on river

floodplains. *Geomorphology, 24*(2-3), 209-223. https://doi.org/10.1016/S0169-555X(98)00017-8

Walling, D. E., & He, Q. (1997a). Use of fallout ^{137}Cs in investigations of overbank sediment deposition on river floodplains. *Catena, 29*(3-4), 263-282. https://doi.org/10.1016/S0341-8162(96)00072-0

Walling, D. E., & He, Q. (1997b). Investigating spatial patterns of overbank sedimentation on river floodplains. *Water, Air, and Soil Pollution, 99*(1), 9-20. https://doi.org/10.1007/BF02406840

Walter, R. C., & Merritts, D. J. (2008). Natural streams and the legacy of water-powered mills. *Science, 319*(5861), 299–304. https://doi.org/10.1126/science.1151716

Ward, J. V., & Stanford, J. A. (1995). Ecological connectivity in alluvial river ecosystems and its disruption by flow regulation. Regulated rivers: research & management, 11(1), 105-119. https://doi.org/10.1002/rrr.3450110109

Wasson, R. J. (2003). A sediment budget for the Ganga–Brahmaputra catchment. *Current science*, 1041-1047.

Wiener, K. D., Schlegel, P. K., Grenfell, S. E., & van der Waal, B. (2022). Contextualising sediment trapping and phosphorus removal regulating services: A critical review of the influence of spatial and temporal variability in geomorphic processes in alluvial wetlands in drylands. *Wetlands Ecology and Management*, 1-34. https://doi.org/10.1007/s11273-022-09861-9

Williams, L., Harrison, S., & O'Hagan, A. M. (2012). The use of wetlands for flood attenuation. Report for an Taisce. Ireland, Cork, University College Cork, Aquatic Services Unit.

Wickham, J., Stehman, S. V., Sorenson, D. G., Gass, L., & Dewitz, J. A. (2021). Thematic accuracy assessment of the NLCD 2016 land cover for the conterminous United States. *Remote Sensing of Environment*, 257, 112357.

Wolman, M. G., & Leopold, L. B. (1957). River flood plains: Some observations on their formation. In U.S. Geological Survey Professional Paper (pp. 87–109). Reston, VA: U.S. Geological Survey. https://doi.org/10.3133/pp282c

Wolman, M. G., & Miller, J. P. (1960). Magnitude and Frequency of Forces in Geomorphic Processes. *The Journal of Geology, 68*(1), 54–74. https://doi.org/10.1086/626637

Wohl, E. (2021). An integrative conceptualization of floodplain storage. *Reviews of Geophysics, 59*(2), e2020RG000724. https://doi.org/10.1029/2020RG000724

Worley, L. C., Underwood, K. L., Vartanian, N. L., Dewoolkar, M. M., Matt, J. E., & Rizzo, D. M. (2022). Semi-automated hydraulic model wrapper to support stakeholder evaluation: A floodplain reconnection study using 2D hydrologic engineering center's river analysis system. *River Research and Applications, 38*(4), 799-809.

Xu, H., Torres, R., van der Steeg, S., & Viparelli, E. (2021). Geomorphology of the Congaree River floodplain: Implications for the inundation continuum. *Water Resources Research,*

57(12), e2020WR029456.

Xu, H., Steeg, S., Sullivan, J., Shelley, D., Cely, J. E., Viparelli, E., et al., (2020). Intermittent channel systems of a low-relief, low-gradient floodplain: Comparison of automatic extraction methods. *Water Resources Research, 56*. https://doi.org/10.1029/2020WR027603

Zwoliński, Z. (1992). Sedimentology and geomorphology of overbank flows on meandering river floodplains. *Geomorphology*, *4*(6), 367–379. https://doi.org/10.1016/0169-555X(92)90032-J

Chapter 4 Potential for Juvenile Freshwater Mussels to Settle onto River Beds from Field Investigation

Sumaiya Sumaiya[1]; Jonathan A. Czuba[1]

[1]Department of Biological Systems Engineering, Virginia Tech, Blacksburg, Virginia, USA

Abstract

In aquatic environments, freshwater mussels play an important role in ecosystem functioning. Despite their importance, freshwater mussel populations have been declining at an alarming rate around the world. Several potential causes for this decline have been proposed, but none are definitive. Herein, we investigate whether changing flow conditions, as they affect juvenile freshwater mussel settling, could be a potential causative factor for this decline in the Dan River, North Carolina, USA. We deployed two uplooking velocity sensors on the river bed between May and November 2019 to calculate shear velocity, which is a measure of the turbulence that acts to lift particles (sediment or juvenile mussels) into suspension and acts against the particle settling velocity. A shear velocity of 0.46 cm/s or less would be required to settle the largest and densest juvenile mussels onto the river bed; however, the lowest shear velocity we measured at the velocity sensors was 0.87 cm/s. Additionally, at these locations, we estimated that juvenile freshwater mussels as large as 280-508 µm could always be suspended during our study period and not be able to settle onto the river bed. Therefore, the flow and shear velocity during 2019 was high enough to prohibit recruitment of juvenile freshwater mussels from settling out of suspension at the sensor locations. However, modest flow obstructions such as large boulders, downed trees, or large wood that create downstream wakes may be important features that provide suitable

conditions for settling of juvenile freshwater mussels onto the river bed. Furthermore, we have identified that low flows have been increasing since 2000 that may be exacerbating the decline in freshwater mussel population.

4.1 Introduction

Freshwater mussels are important to the health of aquatic ecosystems because of their role in water filtration, nutrient cycling, and providing habitat for other aquatic organisms (Geist, 2010; Lummer et al., 2016; Vaughn et al., 2008; Vaughn and Hakenkamp, 2001). Despite their importance, freshwater mussels are currently one of the most imperiled faunal groups globally (Lopes-Lima et al., 2017; Master et al., 2000; Williams et al., 1993). Recent studies show an alarming rate of decline in freshwater mussel species and abundance in many river systems in North America (Haag, 2019; Strayer et al., 2004). Their decline could alter the function of riverine systems having negative consequences on biodiversity.

The life cycle of freshwater mussels is unique and could be broadly divided into four life stages (Haag, 2012). Survival in each life stage is determined by the mortality rate, habitat suitability, and abiotic conditions (Bauer, 1994; Haag, 2012; Jansen et al., 2001). The estimated mortality probabilities were 0.9999, 0.60, 0.50, and 0.05 for the egg/larvae, parasitic, juvenile, and adult stages, respectively (Bauer, 2001; Jansen et al., 2001; Stein, 1973). The life cycle initiates when the male mussel released sperm and females filter the sperm into their gill chambers where the eggs are fertilized and released in the water as tiny larvae called glochidia (Haag, 2012). Released glochidia can survive in the water column before entering in to parasitic stage between a few hours to 14 days (Haag, 2013). Glochidia starts a parasitic stage attaching themselves to the gills or fins of a specific host, mostly fish, and may remain encysted from only a few hours to several weeks depending on the fish host, the attachment position and the abiotic conditions, and water temperature (Bauer, 1994; Dillon, 2000; El-Nobi, & Geist, 2014; Roberts & Barnhart, 1999; Taeubert,). Water temperature in between 11°C and 20°C are found suitable for glochidia survival (Gascho et al., 2012). Glochidia can be present in stream drift year-round, their abundance typically

peaks during May to mid-August (Bruenderman & Neves, 1993; Haag & Warren, 2003; Neves & Widlak, 1988). After metamorphosis on the parasitic stage, juvenile mussels drop off and can be further dispersed via drift (Irmscher, 2018; Morales et al., 2006;). Settling in suitable habitats is important for juveniles to survive and continue their development. Adulthood is reached after 5 years and reproduction begins.

There are several potential causes that could be responsible for the decline in freshwater mussels including water-quality degradation, invasive species, and streamflow or habitat alteration by impoundments (Lydeard et al., 2004; Haag, 2019; Strayer et al., 2004). Alteration of flow regimes and channel characteristics by man-made modifications like dam construction or changes in the climate has significantly reduced the biodiversity in many riverine ecosystems including freshwater mussels (Haag, 2012; Poff et al., 2007). Other potential factors that could be responsible may include fish host distributions, food quality and quantity, water quality, and temperature (Strayer 2008). Some streams previously with highest mussel species abundance experienced sever declination of mussel where no specific cause was reported and referred as enigmatic declines of fresh water mussel (Haag, 2019).

Freshwater mussels are particularly sensitive to changes in hydrologic conditions (Strayer et al., 2004; Watters, 2000;). Complex hydraulic parameters affect the freshwater mussel habitat during both high and low flow conditions. Mussel abundance is low in areas of high shear stresses during high flows (Gangloff and Feminella, 2007; Howard and Cuffey, 2003; Hardison and Layzer, 2001) because excessive shear stresses at high flows can prevent juvenile mussels from settling into streambed (Hardison and Layzer, 2001; Layzer and Madison, 1995). At low flows, minimum values of velocity, depth, Froude and Reynolds numbers are requiered for mussel occupancy and abundance (Gagnon et al., 2004; Maloney et al., 2012; Steuer et al,.2008). Changes in the flow regime due to anthropogenic disturbance, climate change, land-use change, or river impoundments can prevent the riverine

ecosystem from achieving a suitable condition for mussel habitat, which could lead to extirpation and/or extinction of freshwater mussels.

Over the years, several studies have analyzed the hydraulic conditions suitable for mussel habitat. Measured hydraulic parameters at both low and high flows have been investigated to understand the impacts of flow regime (Hardison and Layzer, 2001). Predictive statistical models were developed to analyze the relationships between complex hydraulic variables and mussel habitat quality (Gangloff and Feminella, 2007; Steuer et al., 2008; Zigler et al., 2008). Most of these studies were focused on understanding the dispersal of Glochidia (Modesto, 2018) and stability of the river bed (Morales et al., 2006). However, flow conditions can also strongly affect juvenile freshwater mussel recruitment when they detach from their fish host and settle onto the streambed. Only if the turbulent shear velocity is low enough relative to the mussel fall velocity, would a juvenile freshwater mussel be able to settle onto the river bed. Fall velocity increases with mussel size although varies within the species. Foot movement of juvenile mussel decreases the fall velocity (Schwalb and Ackerman, 2011).

Freshwater mussels in the Dan River, North Carolina, U.S., have been declining over the last few decades. In this study, we investigated whether changes in streamflow conditions affecting the settling of juvenile freshwater mussels, or lack thereof, may be responsible for this decline. We deployed two uplooking velocity sensors in the Dan River between May and November 2019 to measure hydraulic parameters used to estimate turbulent shear velocity. From this data and an estimate of juvenile freshwater mussel settling velocity, we calculated whether juvenile mussels could settle at the locations of our sensors during the time period analyzed. We also extended our analysis back in time using data from a U.S. Geological Survey (USGS) streamflow-gaging station to understand how long-term changes in streamflow may have contributed to freshwater mussel decline.

4.2 Study area

The Dan River drains the Blue Ridge Mountains and Piedmont of Virginia, crossing into North Carolina (Figure 4.1a-b), before entering the John H. Kerr Reservoir where it joins the Roanoke River. Our study reach is the Dan River upstream of its confluence with Big Creek (Figure 4.1c) at US Highway 89 where James spinymussel (*Parvaspina collina*) populations were historically high, but are now federally listed as an endangered species (U.S. Fish & Wildlife Service, 2022). The watershed upstream of our study area is 426 km^2 covered with predominantly forest (70%, NLCD 2016; Wickham et. al, 2021). Upstream in the Blue Ridge Mountains, Townes and Talbott Dams were built in 1938 (Figure 4.1b). The USGS has operated a streamflow gaging station on the Dan River near Francisco, North Carolina (02068500) since 1924. The 99-yrs (1924-2022) mean daily streamflow at this gage is 5.5 m^3/s with all-time minimum and maximum daily flows of about 0.59 m^3/s and 193 m^3/s, respectively (USGS, 2022). Flow is generally high during spring (March-May) and low during August and September. Summer thunderstorms and hurricane remnants contribute to

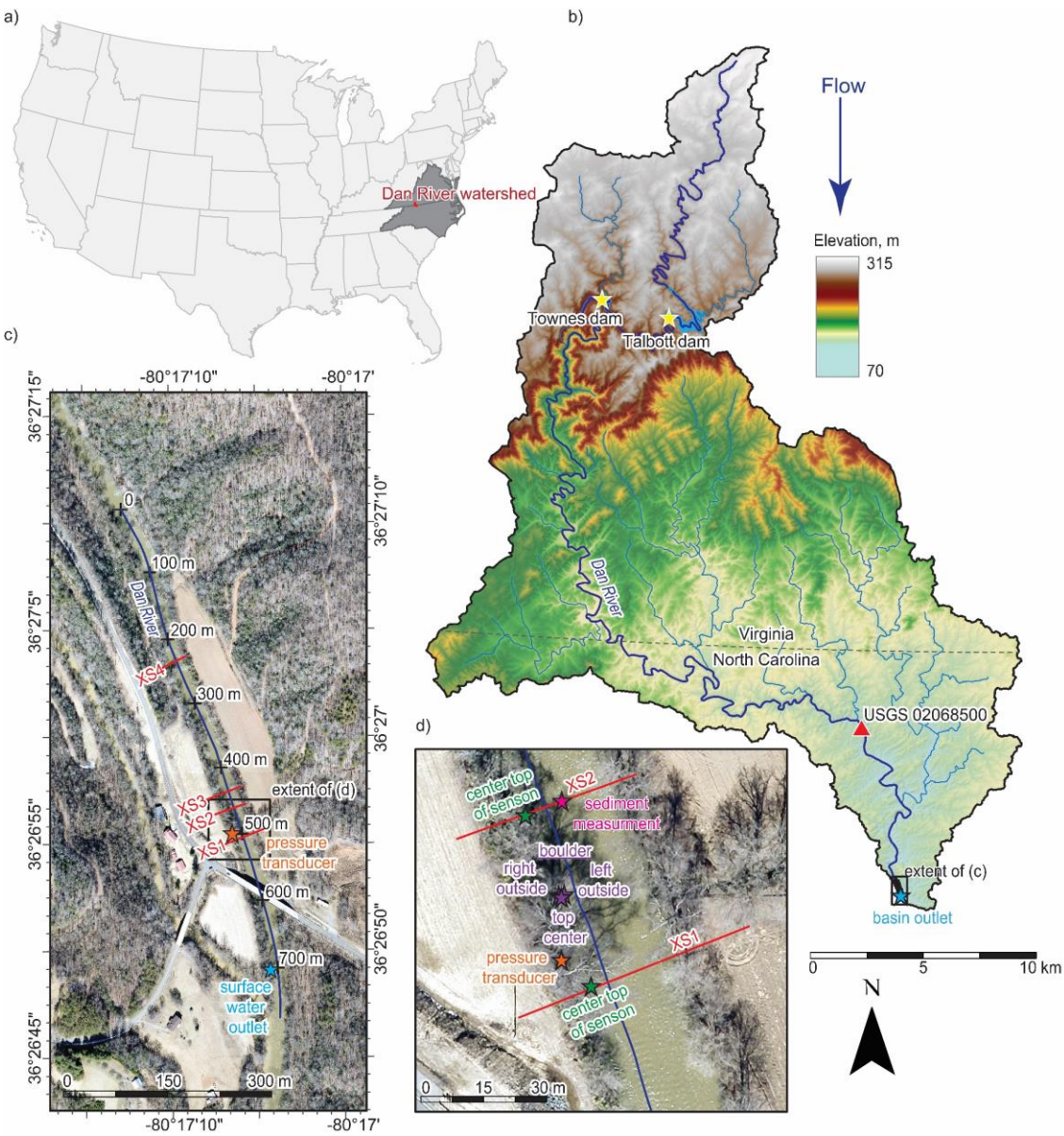

Figure 4.1 (a) Study area map of the Dan River in Virginia and North Carolina. (b) Dan River watershed upstream of our study reach. Dark blue line represents the mainstem Dan River and light blue lines represent major tributaries. Red triangle is the USGS gage near Francisco, North Carolina. Yellow stars indicate the major dams. Black rectangular box is the extent of map (c). (c) Study reach along the Dan River. Blue line with stationing (black +) shows the extent of the surveyed long profile. Red lines indicate the four surveyed cross sections. Orange star indicates the location of a pressure transducer. Black box is the extent of map (d). (d) Zoom of cross sections 1 and 2 where velocity sensors (green stars) were deployed. Dark

yellow stars indicate the edges and top of a large boulder. Purple star at cross section 2 is the sediment measurement location.

4.3 Methods

4.3.1 Field data

We measured hydraulic and sediment characteristics in the Dan River along our 770-m study reach (Figure 4.1c). Two Sontek-IQ Plus uplooking acoustic Doppler velocity meters (Sontek/YSI/Xylem, Yellow Springs, Ohio) were anchored to the streambed at two locations in a run downstream from a riffle (Figure 4.1d). Each sensor measured water velocity profiles above the sensor, water depths above the sensor, and water temperatures at the sensor on the streambed. Both sensors collected data at 15-min intervalsc between 1 May 2019 and 6 November 2019 over the period when juvenile freshwater mussels typically release from their fish hosts and potentially settle onto the streambed. Depth-averaged velocity and turbulent shear velocity was estimated from fitting a logarithmic curve to each velocity profile to account for unmeasured regions in the velocity profile (near the bed and at the water surface) (Keulegan 1938; Garcia 2008).

An Onset HOBO water level data logger (pressure and temperature sensor; Onset, Bourne, Massachusetts) was deployed along the streambank between 24 May 2019 and 6 November 2019 and recorded water depth above the sensor and temperature at 15-min intervals. We mention these data for completeness and we include them in our data repository, but because these data provided no additional information beyond what was reported by the velocity sensors, we no longer refer to the pressure sensor data from hereon.

Four cross sections and a longitudianal profile were measured on three separate field days. Cross-sections 1 and 2 and the profile from 103 to 772 m were surveyed on 27 June

2019 using a Trimble R10 real-time kinematic global positioning system (RTK-GPS; Trimble, Sunnyvale, California) and Topcon GTS-105 Total Station (Topcon, Livermore, California). The longitudinal (long) profile from 0 to 86 m was surveyed on 24 July 2019 using an optical level and tape measure. Cross sections 3 and 4 and the long profile from 177 to 360 m was surveyed on 25 July 2019 using the RTK-GPS and Total Station for cross section 3 and the long profile and an optical level and tape measure for cross section 4. The biggest uncertainties were with cross-section 4 and the long profile from 0 to 86 m. The stage on 27 June and 25 July at the time of the survey were the same. The stage on 24 July was 0.11 m higher and we accounted for this in the data processing by lowering the surveyed water-surface elevation (WSEL) of the long profile from 24 July by 0.11 m to create a composite 27 June (or 25 July) WSEL for the reach.

The grain-size distribution of the bed particles was measured on 25 July by randomly selecting the first particle encountered without looking and measuring the intermediate axis diameter (Wolman, 1954). This process was repeated every 1 m, back and forth across the river (at least three times), until a total of 100 particles were measured. Our first return visit to the study reach after the velocity sensor deployment was on 24 May 2019. This was after a moderate flood that had moved sediment because we noticed sand deposited in the wake of some boulders we placed on the velocity sensor cable from the sensor to the bank to anchor it in place. Additionally, we found a 13-mm diameter rock lodged between our anchoring boulders. In the wake of the boulders anchoring, each velocity sensor cable and near the center of the channel along cross-section 2 (Figure 4.1d), we collected grab samples of sand to sieve in the lab for a sand particle size distribution.

The USGS streamflow-gaging station on the Dan River near Francisco, North Carolina (02068500) was measuring at the same 15-min interval as our velocity sensors. This USGS gage has been measuring daily data from 1 September 1924 to present (missing data: 1

October 1926 – 31 March 1927 and 13 October 1987 – 30 November 1991), 30-min data from 1 October 1984 to 9 March 1998, and 15-min data from 12 March 1998 to present (USGS, 2022). We performed a cross correlation between the USGS data and the velocity sensors (23 river km apart) and determined there was a 1.75-hr time lag on average between the two locations. Whenever we compared the data between the velocity sensors and the USGS gage at 15-min intervals, we applied this time lag. To reduce the measurement noise in some of our data, we averaged our 15-min data over a 3-hr period.

4.3.2 Size, density, and settling velocity of juvenile freshwater mussels

Studies have been performed to investigate juvenile mussel settling in suspension using sediment or polymer microparticles with a known density and settling velocity as a juvenile mussel surrogate (Irmscher, 2018). Schwalb and Ackerman (2011) measured the settling velocity directly in a temperature-balanced settling chamber, mussel shell length and height from image analysis, and mussel density from density gradient centrifugation. Several laboratory investigations of different species of juvenile freshwater mussels have been performed to measure mussel size, density, and settling velocity (Table 4.1). Most literature values of juvenile mussel sizes ranged from 150 to 500 µm with a mean of 250 µm, specific densities ρ_m ranged from 1.0 to 1.28 g/cm^3 with a non-weighted mean of 1.16 g/cm^3, and experimental settling velocities were measured from 0.03 to 0.46 cm/s depending on the size and age of mussel. For our analysis on the potential for juvenile freshwater mussels to settle out of suspension, we used conservative values for size, specific density, and settling velocity of 250-500 µm, 1.28 g/cm^3, and 0.24- 0.46 cm/s, respectively.

Table 4.1: Information on freshwater juvenile mussel shell diameters (D_m), density (ρ_m), and settling velocity (w_m).

References	age (days)	size (D_m, µm)	specific density (ρ_m, g/cm^3)	settling velocity (w_m, cm/s)
Irmscher (2018)	1-3	260-280	1-1.28	0.24
French and Ackerman (2014)	0-29	158-458	–	–
Daraio et al. (2012)	–	220	1.18-1.22	–
Daraio et al. (2010)	–	250	1.28	–
Morales et al. (2006)	–	200	1.0-1.1	0.03
Wächtler et al. (2001)	–	150-200	–	–
Schwalb and Ackerman (2011)	–	200-350	1.2-1.26	0.24-0.46
Stein (1973)	–	220	–	–

4.3.3 Theory of sediment and juvenile freshwater mussel settling and transport

The theory and methods used to describe sediment transport can and has been applied to freshwater mussels by using a specific density for mussels (ρ_m) rather than one for sediment (typically quartz, ρ_s = 2.65 g/cm^3; Irmscher, 2018; Schwalb and Ackerman, 2011). In this section, we describe the sediment transport theory that describes the largest size sediment particle that can be moved in suspension or as bedload from the resulting flow (turbulent shear velocity or bed shear stress, respectively). By applying values for juvenile freshwater mussel size, density, and settling velocity from the literature (Table 4.1), we can compute the potential for the hydraulic conditions we measured in the field to suspend or settle out juvenile freshwater mussels.

The largest sediment and mussel sizes in suspension were estimated using a Rouse number criterion and the largest sediment size transported as bedload was estimated using a Shields stress mobility criterion. The Rouse number (Z_R) was calculated by (Garcia, 2008)

$$Z_R = \frac{w}{\kappa u_*} \tag{1}$$

where κ is von Karman's constant (0.41), u_* is the turbulent shear velocity estimated from the velocity profile data (m/s), and w is the settling velocity of sediment or juvenile mussel (m/s), which is a function of particle diameter and density.

Sediment and mussel settling velocities were calculated using the Ferguson & Church (2004) equation as

$$w_s = \frac{RgD^2}{C_1 \upsilon + \sqrt{0.75\, C_2 RgD^3}} \tag{2}$$

where R is the submerged specific gravity (1.65) for sediment and (0.28) for mussels (detail in section 3.2; Table 4.1), g is the gravitational acceleration (9.81 m/s^2), D is the particle diameter, υ is the kinematic viscosity of water (1×10^{-6} m^2/s), C_1 is a constant with a theoretical value of 18, and C_2 is a constant representing the asymptotic value of the drag coefficient (C_2 = 1 for natural grains).

The threshold condition for a particle to remain in suspension is when the tendency for a particle to settle out of suspension (settling velocity) is balanced by turbulence acting to keep that particle in suspension (shear velocity). That is, when the fall velocity is equal to the shear velocity or, equivalently, when the Rouse number is equal to 2.43 ($1/\kappa$), which is the threshold value for a particle to remain in suspension (Engelund, 1965a,b; Van Rijn, 1984; Niño, 1995; Niño & García, 1998; Niño et al., 2003). The largest sediment or juvenile freshwater mussel size was calculated by combining Equations (1) and (2), inputting parameters relevant for sediment or mussels, can calculating the D for a given value of u_*.

The largest sediment size moved as bedload was computed by comparing Shields stress (τ^*) with critical Shields stress (τ_c^*). Shields stress (τ^*) was calculated as

$$\tau^* = \frac{\tau_b}{\rho g R D} \tag{3}$$

where τ_b is the estimated bed shear stress (Pa), ρ is the density of water (1000 kg/m^3), g is the gravitational acceleration (9.81 m/s^2), R is the dimensionless submerged specific gravity of a sediment particle (1.65).

Bed shear stress (Pa) was estimated from shear velocity (m/s) applying as

$$\tau_b = \frac{{u_*}^2}{\rho} \tag{4}$$

Critical Shields stress (τ_c^*) was calculated as (Brownlie, 1981; Garcia, 2008)

$$\tau_c^* = \frac{1}{2}\left[0.22\, R_{ep}^{-0.6} + 0.06\, exp\left(-17.77\, R_{ep}^{-0.6}\right)\right] \tag{5}$$

where R_{ep} is the particle Reynolds number expressed as

$$R_{ep} = \frac{\sqrt{gRD}\, D}{\upsilon} \tag{6}$$

We computed a Shields stress and an associated critical Shields stress for sediment sizes between 1 µm and 100 mm with 1 µm increments. The largest size for which the calculated $\tau^* > \tau_c^*$ is what we refer to as the largest sediment size that can be transported as bedload. We did not do this bedload analysis for juvenile freshwater mussels because we are mostly interested in the settling process.

4.3.4 Analysis of timeseries data

We primarily analyzed the 99-yr daily streamflow record (1924-2022) from the USGS streamflow gage (02068500) on the Dan River near Francisco, North Carolina, to contextualize our velocity measurements made in 2019. We calculated the minimum, maximum, and mean daily flow and the number of days <2 m^3/s (as a suitable low-flow

indicator, discussed later) for each year and also for the two-month periods of May-June and July-August. May-June is about when we expect freshwater mussels to release their glochidia on fish hosts and July-August is about when we expect juvenile freshwater mussels to detach from their fish hosts and potentially settle onto the streambed. At the time of analysis, 1924 and 2022 only had partial data for the year available, so we analyzed the 97-year streamflow record (1925-2021). To contextualize any recent trends in streamflow characteristics with potential trends in the past, we divided the data into four segments of about 21-year periods of time (1930-1950; 1950-1970; 1970-2000; 2000-2021). Data were unavailable from 1987 to 1991, so we grouped data from 1970-2000.

Trendlines were generated for each of these four periods for the yearly, May-June, and July-August flow record of minimum, maximum, and mean daily streamflow by applying the MATLAB polyfit function. Significant increasing or decreasing trends were identified using the Mann-Kendall trend analysis. The Mann-Kendall trend analysis is one of the most widely used non-parametric methods for long term trend analysis (Buffoni et al. 1999; Déry and Wood, 2005; Jain and Kumar, 2012; Mondal et al. 2012). P-value at 5% level were considered as significant for Mann-Kendall test which means p-value< 0.05 indicates that the trend has statistical significance.

4.4 Results

4.4.1 Channel geometry

For the relatively low-flow conditions characterized by the long profile (27 June or equivalently 25 July 2019; 4.78 m^3/s), depth varied from 0.3 m to 1.3 m with the deepest depths near cross section 4 in a pool (Figure 4.2a). Cross-section 3 is across a riffle and both cross-sections 3 and 4 are located in a run just downstream of a riffle (Figure 4.2a). The slope

of the Dan River in our study reach, estimated from the long profile, is about 0.002. At cross-sections 1 and 2, the bankfull top width is roughly 36 m and the bankfull hydraulic radius is about 3 m (Figure 4.2b-c). The location of the velocity sensors was near the right bank (when looking downstream) and the range of WSELs measured by the velocity sensors is indicated on each cross section (Figure 4.2b-c). The WSEL shown in the long profile was slightly above the lowest WSEL measured by the velocity sensors (as indicated on the cross sections).

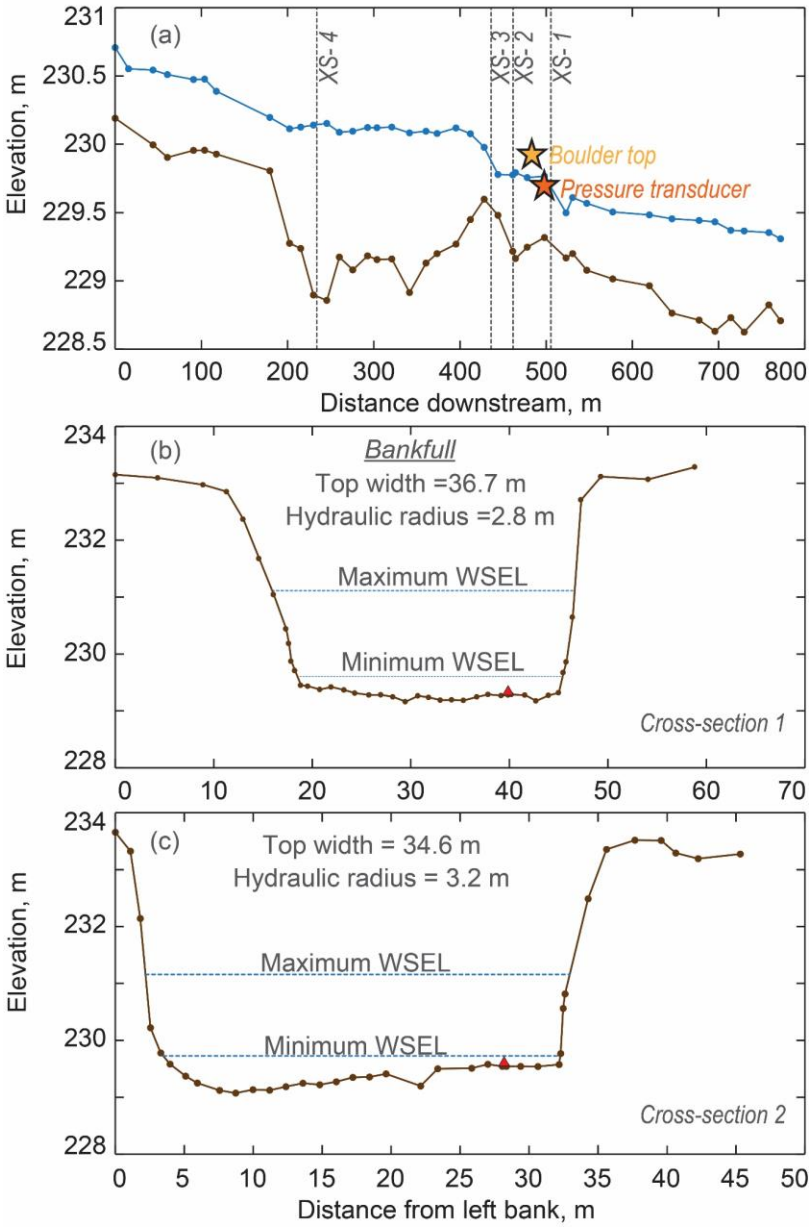

Figure 4.2 Channel geometry of the Dan River at our study area. (a) Longitudinal profile of the 772-m long study reach. Blue line is the water surface elevation (WSEL) from 27 June

2019 or equivalently 25 July 2019 (4.78 m^3/s) and brown line is the thalweg elevation. Vertical dashed lines indicate cross-section measurement locations (Figure 4.1c). Dark yellow circle marks the top of a large boulder that was protruding above the water surface and orange circle marks the submerged pressure transducer. (b) Cross section 1 (XS-1) and (c) cross section 2 (XS-2). Blue dash line is the maximum and minimum WSELs measured by the velocity sensors in 2019. Dark brown line with circles is the surveyed river bed elevations. Red triangle marks the location of the velocity sensors on the river bed. Elevation is above the North American Vertical Datum of 1988 (NAVD88).

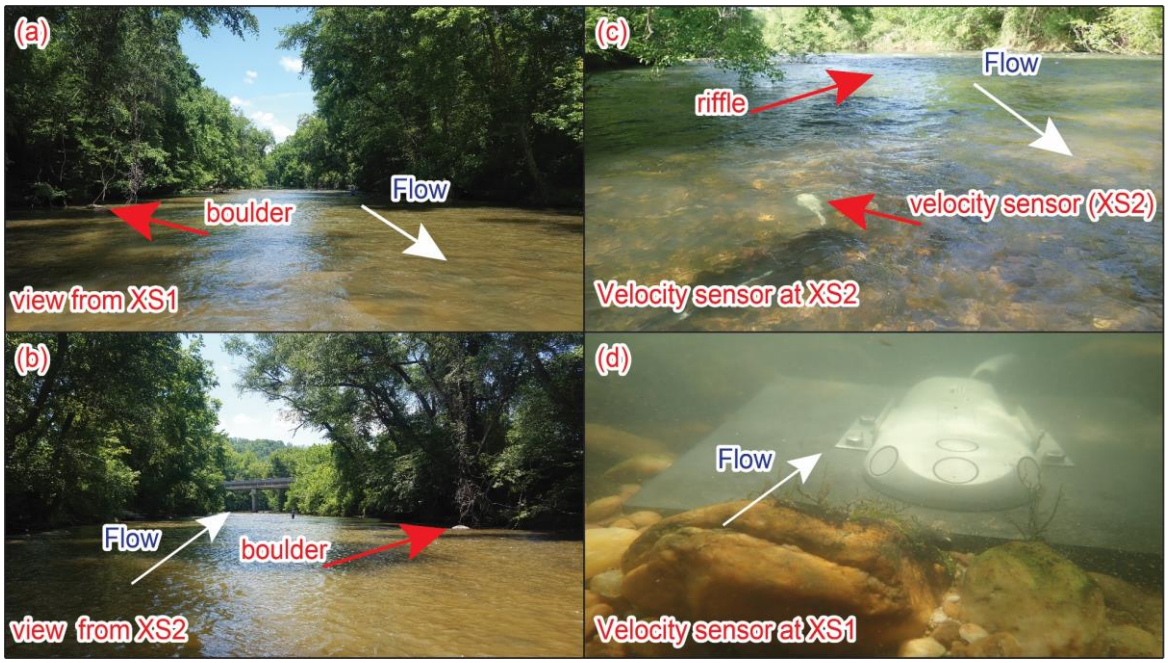

Figure 4.3 Setting of the Dan River study area and velocity sensors. (a) View from cross section 1 looking upstream. (b) View from cross section 2 looking downstream. (c) View showing the submerged velocity sensor at cross section 2 in the foreground and looking upstream toward the riffle in the background. (d) Underwater photo of the velocity sensor at cross section 1, note the small particles in suspension on 1 May 2019.

4.4.2 Hydraulic characteristics

The hydraulic characteristics of our study reach between May and November 2019 in our study reach are shown in Figure 4.4. Characteristics of depth-average velocity (Figure 4.4a), depth above the bed (at the sensor location; Figure 4.4b), streamflow (Figure 4.4c), WSEL (Figure 4.4e), and shear velocity (Figure 4.4d) mostly covaried in time. The depth-average velocities and shear velocities were generally higher with shallower depths at the velocity sensor location at XS2 compared with XS1 because of its closer proximity to the riffle and presence on a more defined gravel bar (Figure 4.2). During the period of data collection, depths above the bed at the sensor locations varied between 0.3 and 1.8 m (XS1) and between 0.18 and 1.6 m (XS2; Figure 4.4b). The maximum depth occurred on 17 June 2019 when the river flow was 75 m^3/s (Figure 4.4c). On that same day depth-average velocity was also at its maximum (1.75 m/s at XS1; 1.25 m/s at XS2; Figure 4.4a). The lowest flow during our data collection period was 2.2 m^3/s which occurred for a 6-day period on 5-11 Oct. 2019. Shear velocities at the location of the velocity sensors ranged from 2.07 to 19.09 cm/s at cross section 1 and 0.87 to 20.36 cm/s at cross section 2 (Figure 4.4d).

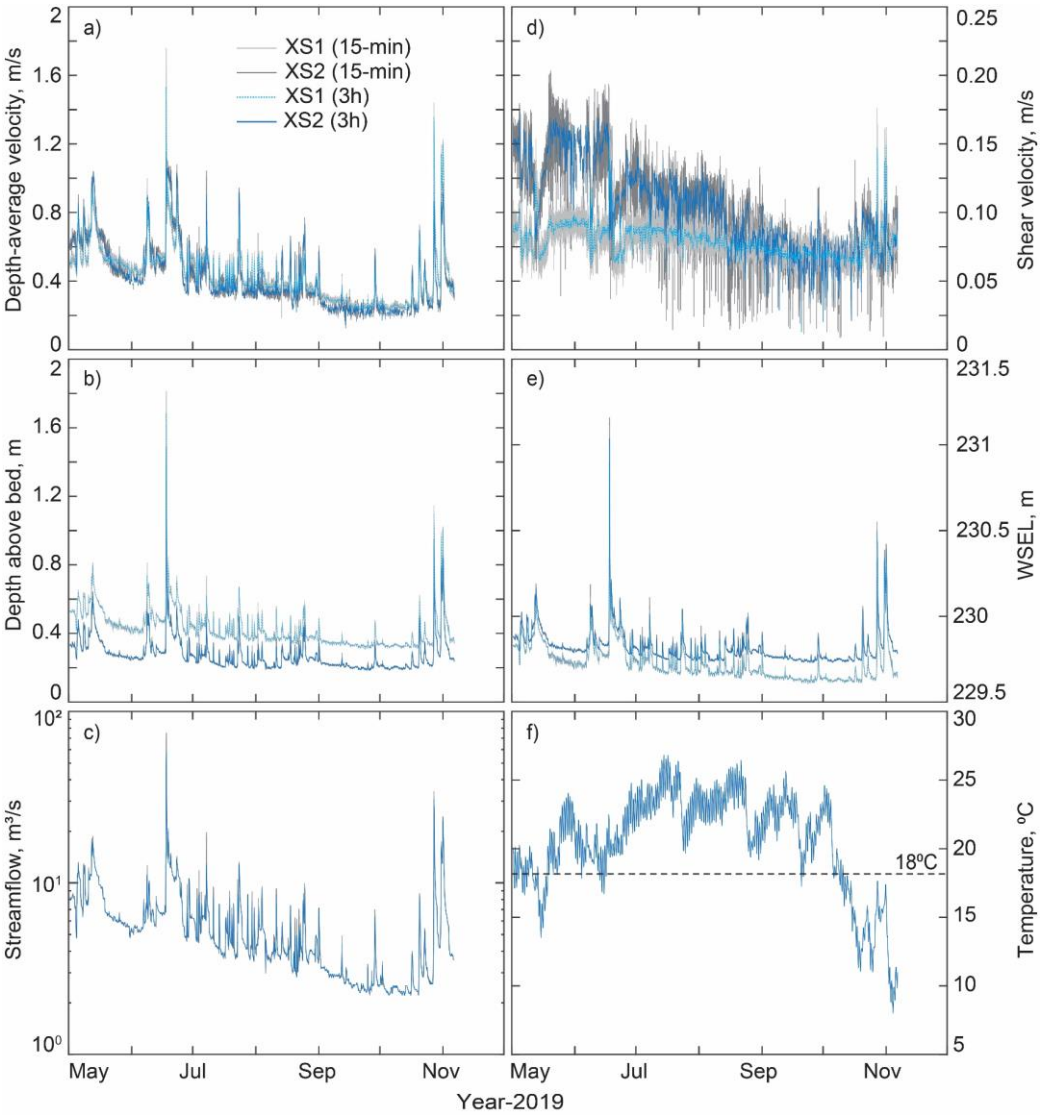

Figure 4.4 Hydraulic characteristics of our study reach between May and November 2019. (a) Depth-averaged velocities, (b) depth above bed, (c) streamflow, (d) shear velocity, (e) water surface elevation (WSEL), and (f) temperature. All characteristics were measured by the velocity sensors except for the flow, which was measure by the USGS at the streamflow gaging station on the Dan River near Francisco, North Carolina (02068500). Instantaneous 15-min data are shown as gray lines (at XS1 and XS2, light and dark, respectively) and 3-hour averages are shown as blue lines. Note that (c) y-axis is logarithmic scale.

An important parameter for mussel reproduction is the water temperature. Generally, freshwater mussels release their glochidia when the water temperature is above 18°C (Gascho et al., 2012). Once the glochidia attach to their fish host, they remain attached for about 2 weeks before detaching from the fish to potentially settle on the bed (Araujo et al., 2002). This temperature signal is important because it sets when juvenile freshwater mussels may begin settling. The maximum water temperature during the day was already above 18°C when the sensors were first deployed, but the minimum water temperature during the day remained above 18°C between 1 May and 13 May 2019, and then after 16 June 2019 the minimum daily water temperature remained above 18°C for the rest of the Spring and Summer.

Hydraulic characteristics of depth-average velocity, shear velocity, and depth were mostly determined by streamflow (Figure 4.5). Depth-average velocity (Figure 4.5a) and depth (Figure 4.5c) generally increase with streamflow, however for the highest flows we measured, (75 m^3/s) there is a strong anticlockwise hysteresis in depth-averaged velocity at both sensor locations (Figure 4.5a). This means that depth-averaged velocity is higher on the falling limb of the hydrograph. Shear velocity was more complicated, where it increased with increasing flow between 2.2 and 6 m^3/s, locally peaking at 6.54 m^3/s, decreased with increasing flow between 6 m^3/s and 15 m^3/s, and then was more variable (due to the velocity hysteresis) but generally increased with increasing flow above 15 m^3/s (Figure 4.5b).

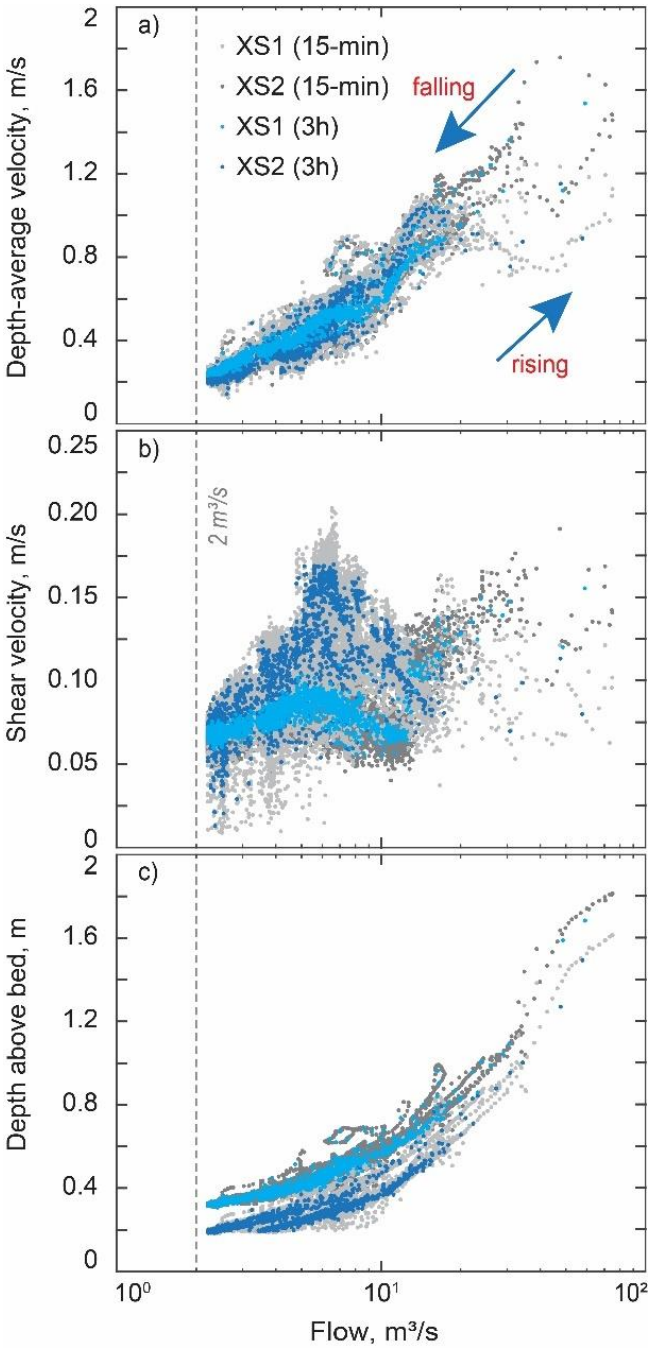

Figure 4.5 Variation in select hydraulic characteristics with streamflow. (a) Depth-average velocity, (b) shear velocity, and (c) depth above bed. Instantaneous 15-min data are shown as gray circles (at XS1 and XS2, light and dark, respectively) and 3-hour averages are shown as blue circles. Vertical gray dash lines marks 2 m^3/s as a low-flow indicator, discussed later. Note that all x-axes are logarithmic scale.

The streamflow conditions we measured in the Dan River in 2019 were generally higher than average, particularly for the low flows (Figure 4.6a). We have reproduced and rotated Figure 4.5b as Figure 4.6b to align it with the historical daily flow record. For juvenile freshwater mussels of 200 to 350 µm, the settling velocity is 0.24 m/s and 0.46 m/s (Table 4.1, Schwalb and Ackerman, 2011). These sizes of juvenile freshwater mussels would be expected to settle to the bed at shear velocities less than at these same values (indicated as dashed lines in Figure 4.6b). The lowest instantaneous shear velocity that we measured above our velocity sensors during May-November 2019 was about 0.087 m/s at a flow just above 2 m^3/s (Figure 4.6b). This suggests that the shear velocities at the specific locations of our velocity sensors during May-November 2019 were too high for our most conservative estimates of juvenile freshwater mussels to settle (largest size, density, and settling velocity; Table 4.1). Therefore, we are unable to determine a specific flow threshold at which juvenile freshwater mussels have the potential to settle to the river bed at these locations and which we could use to investigate how the occurrence of that flow condition has changed in the past. Instead, we have selected 2 m^3/s as a suitable low-flow condition which may be close to allowing juvenile freshwater mussels to settle that we can use as a proxy for assessing how low flows (relevant to juvenile freshwater mussels) may have changed in the past.

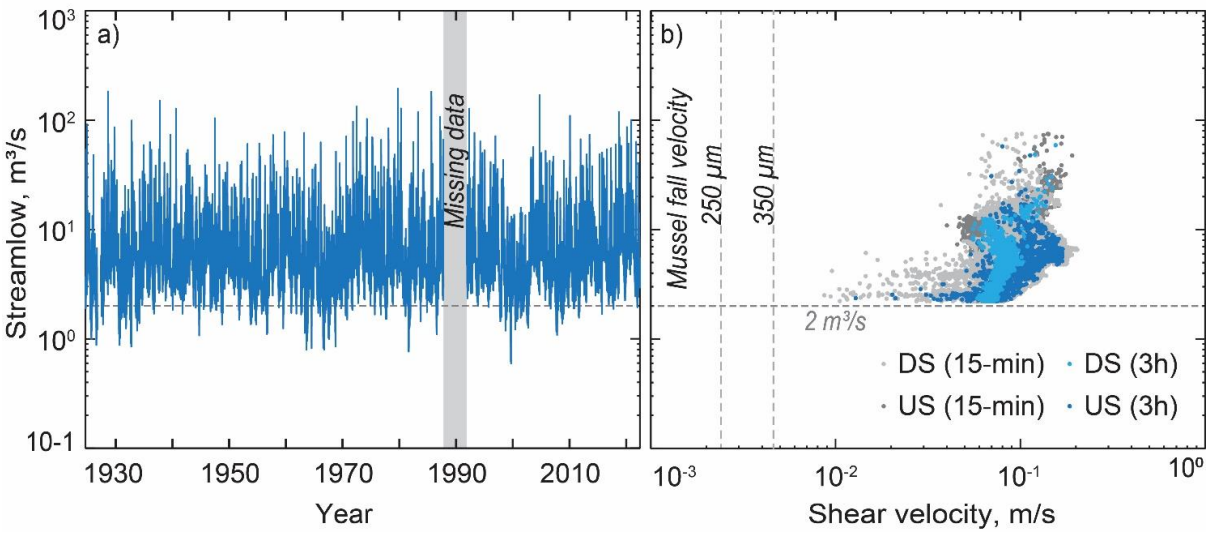

Figure 4.6 Historical streamflow data relative to 2019 shear velocity measurements. (a) Daily streamflow at the USGS streamflow gaging station on the Dan River near Francisco, North Carolina (02068500). Gray bar indicates missing data (13 October 1987 to 30 November 1991). (b) Shear velocity measured at the velocity sensors. Instantaneous 15-min data are shown as gray circles (at XS1 and XS2, light and dark, respectively) and 3-hour averages are shown as blue circles. Vertical dash lines denote the fall velocity for 250 µm and 500 µm sizes of juvenile freshwater mussels (Table 4.1). Horizontal gray dash line indicates 2 m^3/s as a low-flow indicator. Note that both y-axes and x-axis of (b) are logarithmic scale.

4.4.3 Largest sediment and mussel size potentially in suspension

The largest sediment size that could potentially be lifted in suspension and transported as bedload are indicated in Figure 4.7a-b. Between when the velocity sensors were first deployed on 1 May 2019 and when we revisited the sensors on 24 May 2019, we found a 13-mm diameter rock lodged between the boulders that we placed to anchor the velocity sensor cables (at XS1; red line Figure 4.7b). This rock was the largest sediment size that we could confirm that was transported over that period. We estimated that the peak flow on 18 June

2019 was capable of moving sediment as bedload as large as 41 mm (Figure 4.7b). We also noted during our initial velocity sensor deployment, that sand was easily suspended at the velocity sensors (see sand particles in Figure 4.2d). We estimated that sediment as large as 0.8 mm and 1.4 mm were capable of being suspended on 1 May 2019 at cross section 1 and 2, respectively (Figure 4.1a-b) and that the sand sizes on the streambed had a D50 of 0.6 mm to 0.7 mm (Table 4.2). Therefore, we generally confirm the utility of this approach.

At the velocity sensor at cross section 2, we estimated that the flow could have suspended a sediment particle as large as 2 mm and at a minimum always suspend a sediment particle as large as 108 µm (Figure 4.7a). At the velocity sensor at cross section 1, we estimated that the flow could have suspended a sediment particle as large as 1.8 mm and at a minimum always suspend a sediment particle as large 184 µm (Figure 4.7b). Whereas, for juvenile freshwater mussels at cross section 2, the flow could have suspended (or prevented from settling) a mussel size as large as 11 mm and at a minimum always suspend a mussel as large as 280 µm (Figure 4.7c). At cross section 1, the flow could have suspended a mussel size as large as 10 mm and at a minimum always suspend a mussel as large as 508 µm (Figure 4.7d). These results further indicate that at the velocity sensor locations, juvenile freshwater mussels as large as 280-508 µm could always be suspended between May and November 2019 and not be able to settle on to the river bed.

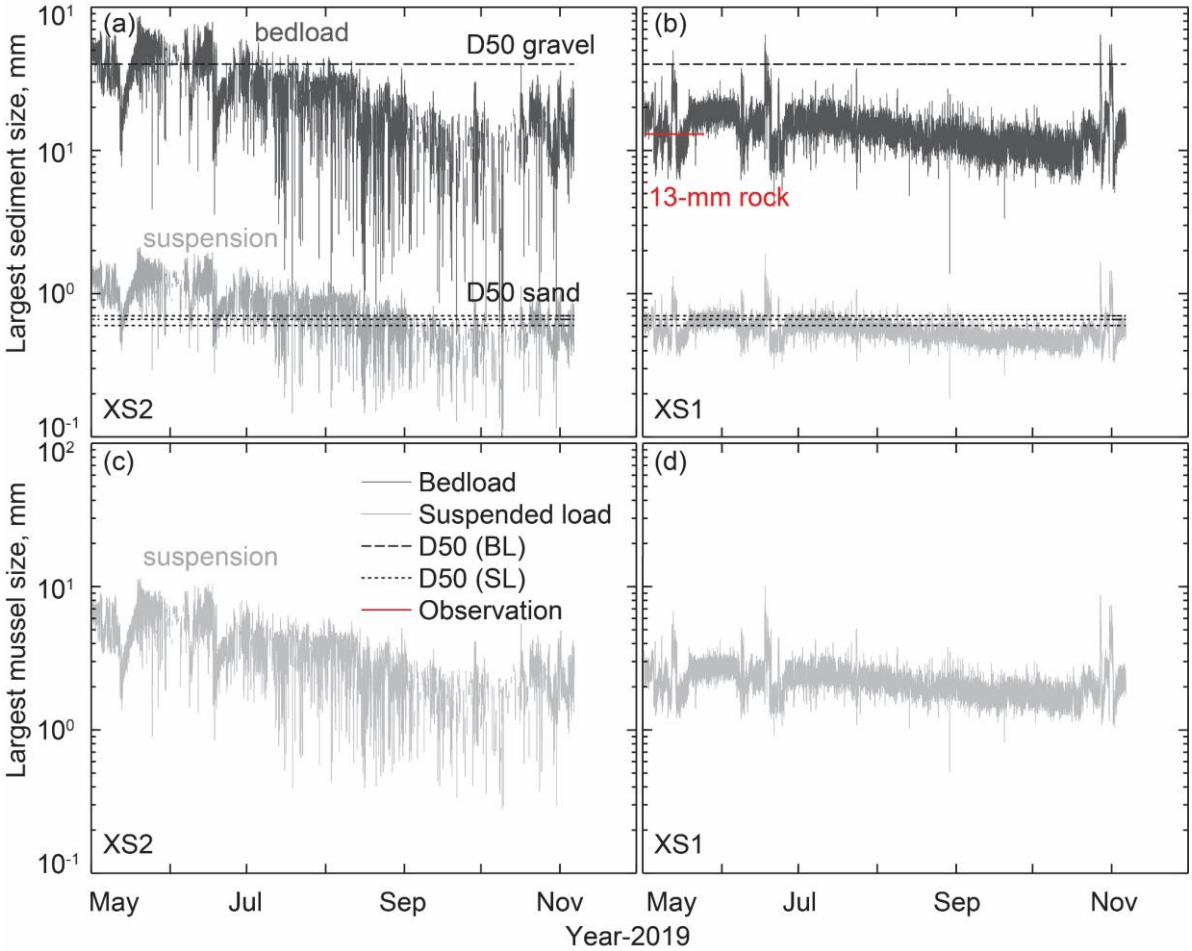

Figure 4.7 Largest sediment and mussel sizes that could be moved by the flow conditions at the location of the velocity sensors. Largest sediment size in suspension (gray line) and as bedload (black line) at the velocity sensors at cross sections 2 (a) and 1 (b). Black long-dash line is the D50 of gravel and gray short-dashed line is the D50 of the sand (one for each of three samples; Table 4.2). Red line represents the 13-mm diameter sediment particle that was observed to have moved sometime within the time period indicated by the length of the line at cross section 1. Largest juvenile freshwater mussel size in suspension at cross sections 2 (c) and 1 (d).

Table 4.2: Particle size statistics of bed material sand and gravel (See Figure 4.1d for sand sampling locations)

Particle size distribution	Sand Size (mm)			Gravel Size (mm)
	XS1 velocity sensor	XS2 velocity sensor	XS2 toward channel center	
D10	0.25	0.25	0.31	6
D16	0.29	0.30	0.37	10
D50	0.59	0.69	0.66	41
D84	1.06	1.89	0.99	138
D90	1.53	2.89	1.36	173

4.4.4 Historical changes in select streamflow characteristics

Since 2000, there was a statistically significant (p-value < 0.05) increasing trend in the maximum, mean, and minimum daily flows for the year (Figure 4.8a) and mean and minimum daily flows during May-June (Figure 4.8b; Table 4.3). There were no statistically significant trends identified during this time period in July-August, however, the p-value for the mean and minimum daily flows was nearly significant with a p-value of 0.06 (Table 4.3). For historical context, both increasing and decreasing trends in these streamflow characteristics have occurred. The historical time period of 1930-1950 had nearly as significant increasing trends with an increase in mean daily flow for the year, maximum, mean, and minimum daily flows during May-June, and mean and minimum daily flows during July-August (Figure 4.8, Table 4.3). Specifically, since 2010, there have been very few flows < 2 m^3/s during May-June and July-August compared with historical conditions that could have been important recruitment periods for freshwater mussels. The most recent potential recruitment periods may have been around 1999-2002 and 2007-2011 when more than roughly 24 days were < 2 m^3/s during July-August.

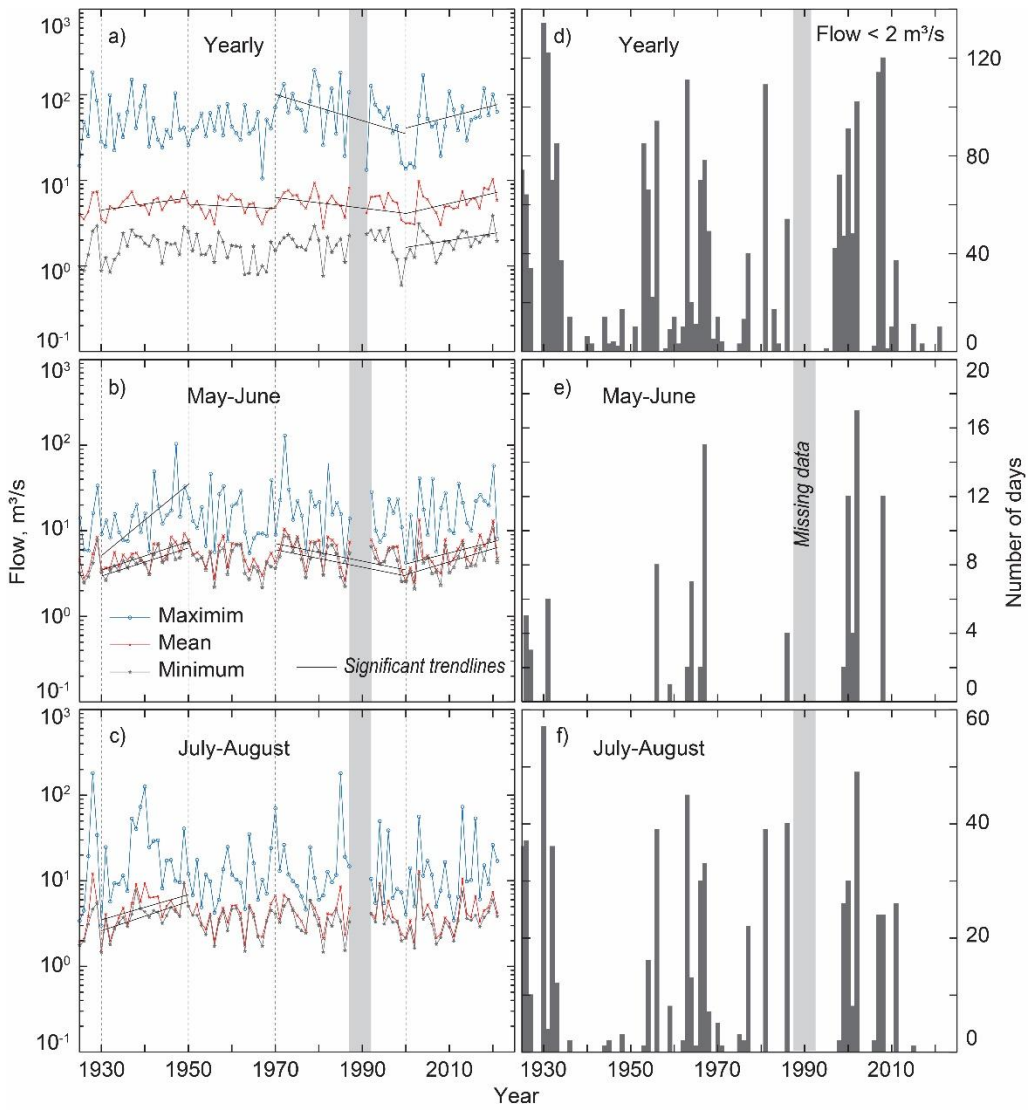

Figure 4.8 Changes in select streamflow characteristics over time (1925-2021) at the USGS streamflow-gaging station on the Dan River near Francisco, North Carolina (02068500). Solid blue, red, and gray lines in panel (a, b, c) represent the maximum, mean, and minimum daily flow values, respectively, for the entire year (a), May-June (b), and July-August (c). Dark gray bars in panel (d, e, f) represent the number of days with streamflow below 2 m^3/s, for the entire year (d), May-June (e), and July-August (f). Light gray bar highlights a period of missing data (13 October 1987 to 30 November 1991). Solid black lines denote the significant trendlines (Table 4.3). Note the y-axes of (a-c) are logarithmic scale and that the y-axes scales are different for (d-f).

Table 4.3: Identification of statistically significant trendlines for flow time series from Mann-Kendall test. H (null hypothesis) and p-value indicate significance: a p-value < 0.05, H= 1 indicates the trend is significant; a p-value > 0.05, H= 0 indicates the trend is not significant.

Flow	**Time**	**Mean**		**Minimum**		**Maximum**	
		H	P-Value	H	P-Value	H	P-Value
Yearly	1930-2021	0	0.448	0	0.123	0	0.345
	1930-1950	1	0.027	0	0.065	0	0.975
	1950-1970	1	0.009	0	0.065	0	0.450
	1970-2000	1	0.013	0	0.454	1	9.32 e-06
	2000-2021	1	0.015	1	0.001	1	0.015
May-June	1930-2021	0	0.321	0	0.439	0	0.447
	1930-1950	1	5.15 e-04	1	0.004	1	0.014
	1950-1970	0	0.215	0	0.174	0	0.414
	1970-2000	1	0.0068	1	0.035	0	0.077
	2000-2021	1	0.0153	1	0.011	0	0.175
July-August	1930-2021	0	0.130	0	0.327	0	0.237
	1930-1950	1	0.020	1	0.001	0	0.290
	1950-1970	0	0.145	0	0.739	0	0.381
	1970-2000	0	0.061	0	0.086	0	0.160
	2000-2021	0	0.062	0	0.064	0	0.3521

4.5 Discussion

We deployed two uplooking velocity sensors in the Dan River at locations where freshwater mussel populations have been ageing with low recruitment of juveniles (Figure 4.1d). Between May and November 2019, we measured water depths, depth-average velocities, and estimated shear velocities (Figure 4.4) that we combined with sediment

transport theory applied to juvenile freshwater mussels (Figure 4.6b and 7c,d) to assess whether the flow conditions at these locations would allow juvenile freshwater mussels to settle onto the river bed. Our conservative estimate (fastest settling) for the largest and densest juvenile freshwater mussel (Table 4.1) that potentially might settle onto the streambed would settle at a rate of 0.46 cm/s and thus would require a shear velocity of 0.46 cm/s or less to actually settle onto the streambed. The lowest shear velocity we measured at the velocity sensors was 0.87 cm/s (Figure 4.4d and 6b). Additionally, at these locations, we estimated that juvenile freshwater mussels as large as 280-508 µm could always be suspended between May and November 2019 and not be able to settle onto the river bed (Figure 4.7c,d). This suggests that during the late Spring through Summer 2019, the flow was high enough to prohibit any juvenile freshwater mussels from settling onto the streambed at the locations of the velocity sensors.

Even though we were not able to measure flow conditions conducive to juvenile mussel settling at the locations of the velocity sensors, there might have been other areas in the river during this time where juvenile mussels could have settled onto the streambed. For instance, there is a large boulder between the two velocity sensors. In the immediate wake of this boulder, we suspect that the flow conditions would have been sufficient at some time (not measured) where juvenile mussels could have settled onto the river bed. If so, this location (and similar locations) could serve as settling locations from which young mussels could then move out from and colonize nearby gravel beds. Other similar locations might include behind downed trees and large wood along the banks of the river, but these features may be more ephemeral than the large boulders.

The higher low flows in 2019 appeared to be part of an increasing trend since 2000 where there was a statistically significant (p-value < 0.05) increasing trend in the maximum, mean, and minimum daily flows for the year (Figure 4.8a) and mean and minimum daily

flows during May-June (Figure 4.8b; Table 4.3). The increasing trend in mean and minimum daily flows during July-August was nearly significant with a p-value of 0.06 (Table 4.3). Additionally, since 2010, there have been very few flows < 2 m^3/s during May-June and July-August compared with historical conditions that could have been important recruitment periods for freshwater mussels. The most recent potential recruitment periods may have been around 1999-2002 and 2007-2008 when more than roughly 20 days were < 2 m^3/s during July-August. Historically, 1930-1950 also had statistically significant increasing trends in many of the streamflow characteristics (Figure 4.8).

Low flows could have been affected through time by the completion of Townes and Talbott Dams in 1938 or a change in operational practices, fluctuating precipitation patterns on decadal scales (Kurtzman, 2007; Schmidt et al. 1999; Trenberth and Guillemot, 1996; Zhao, 2022;), and/or increased precipitation due to the effects of climate change, which are becoming more pronounced (IPCC, 2022). However, determining which or the degree to which each of these factors may have affected low flows is beyond the scope of the present study. For future work, beyond the streamflow characteristics analyzed herein, investigating the rate of change of a hydrograph rise or streamflow responses that occur without precipitation, and how this has changed over time, should provide insight into the potential role of changing dam operations on low flows.

4.6 Concluding remarks

Freshwater mussel populations have been declining in the Dan River, North Carolina. We investigated whether changing flow conditions, as they affect juvenile freshwater mussel settling, could be a potential causative factor for this decline. We deployed two uplooking velocity sensors in the Dan River between May and November 2019 to measure water depth,

depth-average velocity, and shear velocity. A shear velocity of 0.46 cm/s or less would be required to settle the largest and densest juvenile mussels onto the river bed, however, the lowest shear velocity we measured at the velocity sensors was 0.87 cm/s. Additionally, at these locations, we estimated that juvenile freshwater mussels as large as 280-508 µm could always be suspended during our study period and not be able to settle onto the river bed. This suggests that during the late Spring through Summer 2019, the flow was high enough to prohibit any juvenile freshwater mussels from settling onto the streambed at the locations of the velocity sensors. This highlights the potential importance of modest flow obstructions such as large boulders, downed trees, or large wood that create downstream wakes that may provide suitable conditions for settling of juvenile freshwater mussels onto the river bed. Furthermore, we have identified that low flows have been increasing since 2000 that may be exacerbating the decline in freshwater mussel population.

References for Chapter 4

Araujo, R., Cámara, N., & Ramos, M. A. (2002). Glochidium metamorphosis in the endangered freshwater mussel Margaritifera auricularia (Spengler, 1793): a histological and scanning electron microscopy study. *Journal of Morphology*, *254*(3), 259-265.

Bauer, G. (2001). *Ecology and Evolution of the Freshwater Mussels Unionoida: With 38 Tables* (Vol. 145). Springer Science & Business Media.

Bauer, G. (1994). The adaptive value of offspring size among freshwater mussels (Bivalvia; Unionoidea). *Journal of Animal Ecology*, 933-944. https://doi.org/10.2307/5270

Brownlie, W. R. (1981). Prediction of flow depth and sediment discharge in open channels Report No. KH-R-43A. Pasadena, CA: Keck Laboratory of Hydraulics and Water Resources, California Institute of Technology.

Bruenderman, S. A., & Neves, R. J. (1993). Life history of the endangered fine-rayed pigtoe Fusconaia cuneolus(Bivalvia: Unionidae) in the Clinch River, Virginia. *American Malacological Bulletin*, *10*(1), 83-91.

Buffoni, L., Maugeri, M., & Nanni, T. (1999). Precipitation in Italy from 1833 to 1996. *Theoretical and Applied Climatology*, 63(1), 33-40. https://doi.org/10.1007/s007040050089

Daraio, J. A., Weber, L. J., Zigler, S. J., Newton, T. J., & Nestler, J. M. (2012). Simulated effects of host fish distribution on juvenile unionid mussel dispersal in a large river. *River research and applications*, *28*(5), 594-608. DOI: 10.1002/rra.1469

Daraio, J. A., Weber, L. J., Newton, T. J., & Nestler, J. M. (2010). A methodological framework for integrating computational fluid dynamics and ecological models applied to juvenile freshwater mussel dispersal in the Upper Mississippi River. *Ecological Modelling*, *221*(2), 201-214. https://doi.org/10.1016/j.ecolmodel.2009.10.008

Déry, S. J., & Wood, E. F. (2005). Decreasing river discharge in northern Canada. *Geophysical research letters*, *32*(10). https://doi.org/10.1029/2005GL022845

Dillon, R. T. (2000). The ecology of freshwater molluscs.

Engelund, F. (1965a). A criterion for the occurrence of suspended load. La Houille Blanche, 8(7). Engelund, F. (1965b). Turbulent energy and suspended load (Vol. 10). Coastal Engineering Laboratory, Technical University of Denmark.

Ferguson, R. I., & Church, M. (2004). A simple universal equation for grain settling velocity. Journal of Sedimentary Research, 74(6), 933–937. https://doi.org/10.1306/051204740933

French, S. K., & Ackerman, J. D. (2014). Responses of newly settled juvenile mussels to bed shear stress: implications for dispersal. *Freshwater Science*, *33*(1), 46-55. https://doi.org/10.1086/674983

Gagnon, P. M., Golladay, S. W., Michener, W. K., & Freeman, M. C. (2004). Drought

responses of freshwater mussels (Unionidae) in coastal plain tributaries of the Flint River basin, Georgia. *Journal of Freshwater Ecology*, *19*(4), 667-679. https://doi.org/10.1080/02705060.2004.9664749

Gangloff, M. M., & Feminella, J. W. (2007). Stream channel geomorphology influences mussel abundance in southern Appalachian streams, USA. *Freshwater Biology*, *52*(1), 64-74. https://doi.org/10.1111/j.1365-2427.2006.01673.x

Garcia, M. (Ed.). (2008). Sedimentation engineering: Processes, measurements, modeling, and practice. American Society of Civil Engineers.

Garcia, M. Chapter 2 Sediment Transport and Morphodynamics. In Sedimentation Engineering: Processes, Measurements, Modeling, and Practice; American Society of Civil Engineers: Reston, VA, USA, 2008; ISBN 0-7844-0814-9

Gascho Landis, A. M., Mosley, T. L., Haag, W. R., & Stoeckel, J. A. (2012). Effects of temperature and photoperiod on lure display and glochidial release in a freshwater mussel. *Freshwater Science*, 31(3), 775-786. https://doi.org/10.1899/11-082.1

Geist, J. (2010). Strategies for the conservation of endangered freshwater pearl mussels (Margaritifera margaritifera L.): a synthesis of conservation genetics and ecology. *Hydrobiologia*, *644*(1), 69-88. https://doi.org/10.1007/s10750-010-0190-2

Haag, W. R. (2019). Reassessing enigmatic mussel declines in the United States. *Freshwater Mollusk Biology and Conservation*, 22(2), 43-60. https://doi.org/10.31931/fmbc.v22i2.2019.43-60

Haag, W. R. (2013). The role of fecundity and reproductive effort in defining life-history strategies of North American freshwater mussels. *Biological Reviews*, 88(3), 745-766. https://doi.org/10.1111/brv.12028

Haag, W. R. (2012). *North American freshwater mussels: natural history, ecology, and conservation*. Cambridge University Press.

Haag, W. R., & Warren Jr, M. L. (2003). Host fishes and infection strategies of freshwater mussels in large Mobile Basin streams, USA. *Journal of the North American Benthological Society*, *22*(1), 78-91. https://doi.org/10.2307/1467979

Hardison, B. S., & Layzer, J. B. (2001). Relations between complex hydraulics and the localized distribution of mussels in three regulated rivers. *Regulated Rivers: Research & Management: An International Journal Devoted to River Research and Management*, *17*(1), 77-84. https://doi.org/10.1002/1099-1646(200101/02)17:1%3C77::AID-RRR604%3E3.0.CO;2-S

Howard, J. K., & Cuffey, K. M. (2003). Freshwater mussels in a California North Coast Range river: occurrence, distribution, and controls. *Journal of the North American Benthological Society*, *22*(1), 63-77. https://doi.org/10.2307/1467978

IPCC, 2022: Summary for Policymakers [H.-O. Pörtner, D.C. Roberts, E.S. Poloczanska, K. Mintenbeck, M. Tignor, A. Alegría, M. Craig, S. Langsdorf, S. Löschke, V. Möller, A. Okem (eds.)]. In: Climate Change 2022: Impacts, Adaptation and Vulnerability. Contribution of Working Group II to the Sixth Assessment Report of the

Intergovernmental Panel on Climate Change [H.-O. Pörtner, D.C. Roberts, M. Tignor, E.S. Poloczanska, K. Mintenbeck, A. Alegría, M. Craig, S. Langsdorf, S. Löschke, V. Möller, A. Okem, B. Rama (eds.)]. Cambridge University Press, Cambridge, UK and New York, NY, USA, pp. 3–33, doi:10.1017/9781009325844.001.

Irmscher, P., & Vaughn, C. C. (2018). Effects of juvenile settling and drift rates on freshwater mussel dispersal. *The American Midland Naturalist*, *180*(2), 258-272.

Jansen, W., Bauer, G., & Zahner-Meike, E. (2001). Glochidial mortality in freshwater mussels. In *Ecology and evolution of the freshwater mussels Unionoida* (pp. 185-211). Springer, Berlin, Heidelberg. DOI: 10.1007/978-3-642-56869-5_11

Layzer, J. B., & Madison, L. M. (1995). Microhabitat use by freshwater mussels and recommendations for determining their instream flow needs. *Regulated Rivers: Research & Management*, *10*(2-4), 329-345. https://doi.org/10.1002/rrr.3450100225

Jain, S. K., & Kumar, V. (2012). Trend analysis of rainfall and temperature data for India. *Current Science*, 37-49.Keulegan, G.H. Laws of turbulent flow in open channels. *J. Res. Natl. Inst. Stand. Technol.* **1938**, *21*, 707

Kurtzman, E. N. S. O. Pacific Decadal Oscillation impacts on precipitation in the southern and central United States: evaluation of spatial distribution and predictions. *Water Resour. Res*, (43), W10427.

Lummer, E. M., Auerswald, K., & Geist, J. (2016). Fine sediment as environmental stressor affecting freshwater mussel behavior and ecosystem services. *Science of the Total Environment*, *571*, 1340-1348. https://doi.org/10.1016/j.scitotenv.2016.07.027

Lopes-Lima, M., Sousa, R., Geist, J., Aldridge, D. C., Araujo, R., Bergengren, J., ... & Zogaris, S. (2017). Conservation status of freshwater mussels in Europe: state of the art and future challenges. *Biological reviews*, *92*(1), 572-607. https://doi.org/10.1111/brv.12244

Lydeard, C., Cowie, R. H., Ponder, W. F., Bogan, A. E., Bouchet, P., Clark, S. A., ... & Thompson, F. G. (2004). The global decline of nonmarine mollusks. *BioScience*, *54*(4), 321-330. https://doi.org/10.1641/0006-3568(2004)054[0321:TGDONM]2.0.CO;2

Maloney, K. O., Lellis, W. A., Bennett, R. M., & Waddle, T. J. (2012). Habitat persistence for sedentary organisms in managed rivers: the case for the federally endangered dwarf wedgemussel (Alasmidonta heterodon) in the Delaware River. *Freshwater Biology*, *57*(6), 1315-1327. https://doi.org/10.1111/j.1365-2427.2012.02788.x

Master, L. L., Stein, B. A., & Hammerson, G. A. K. (2000). Vanishing assets: conservation status of US species. In *Precious heritage*. Oxford University Press.

Modesto, V., Ilarri, M., Souza, A. T., Lopes-Lima, M., Douda, K., Clavero, M., & Sousa, R. (2018). Fish and mussels: importance of fish for freshwater mussel conservation. *Fish and Fisheries*, *19*(2), 244-259.

Mondal, A., Kundu, S., & Mukhopadhyay, A. (2012). Rainfall trend analysis by Mann-Kendall test: A case study of north-eastern part of Cuttack district, Orissa. *International Journal of Geology, Earth and Environmental Sciences*, *2*(1), 70-78.

Morales, Y., Weber, L. J., Mynett, A. E., & Newton, T. J. (2006). Effects of substrate and hydrodynamic conditions on the formation of mussel beds in a large river. *Journal of the North American Benthological Society*, *25*(3), 664-676. https://doi.org/10.1899/0887-3593(2006)25[664:EOSAHC]2.0.CO;2

Neves, R. J., & Widlak, J. C. (1988). Occurrence of glochidia in stream drift and on fishes of the upper North Fork Holston River, Virginia. American Midland Naturalist, 111-120. https://doi.org/10.2307/2426059

Niño, Y. (1995). Particle motion in the near bed region of a turbulent open channel flow: Implications for bedload transport by saltation and sediment entrainment into suspension (doctoral dissertation). University of Illinois at Urbana-Champaign.

Niño, Y., & García, M. (1998). Engelund's analysis of turbulent energy and suspended load. Journal of Engineering Mechanics, 124(4), 480–483. https://doi.org/10.1061/(ASCE)0733-9399(1998)124:4(480)

Niño, Y., Lopez, F., & Garcia, M. (2003). Threshold for particle entrainment into suspension. Sedimentology, 50(2), 247–263. https://doi. org/10.1046/j.1365-3091.2003.00551.x

Poff, N. L., Olden, J. D., Merritt, D. M., & Pepin, D. M. (2007). Homogenization of regional river dynamics by dams and global biodiversity implications. *Proceedings of the National Academy of Sciences*, *104*(14), 5732-5737. https://doi.org/10.1073/pnas.0609812104

Rijn, L. C. V. (1984). Sediment transport, part II: Suspended load transport. Journal of Hydraulic Engineering, 110(11), 1613–1641. https:// doi.org/10.1061/(asce)0733-9429(1984)110:11(1613)

Roberts, A. D., & Barnhart, M. C. (1999). Effects of temperature, pH, and CO 2 on transformation of the glochidia of Anodonta suborbiculata on fish hosts and in vitro. *Journal of the North American Benthological Society*, *18*(4), 477-487. https://doi.org/10.2307/1468380

Schmidt, N., Lipp, E. K., Rose, J. B., & Luther, M. E. (2001). ENSO influences on seasonal rainfall and river discharge in Florida. *Journal of Climate*, 14(4), 615-628. https://doi.org/10.1175/1520-0442(2001)014%3C0615:EIOSRA%3E2.0.CO;2

Schwalb, A. N., & Ackerman, J. D. (2011). Settling velocities of juvenile Lampsilini mussels (Mollusca: Unionidae): the influence of behavior. *Journal of the North American Benthological Society*, *30*(3), 702-709.

Stein, C. B. (1973). *The life history of Amblema plicata (Say, 1817), the three-ridge naiad (Mollusca: Bivalvia)*. The Ohio State University.

Strayer, D. L. (2008). *Freshwater mussel ecology: a multifactor approach to distribution and abundance* (Vol. 1). Univ of California Press.

Strayer, D. L., Downing, J. A., Haag, W. R., King, T. L., Layzer, J. B., Newton, T. J., & Nichols, J. S. (2004). Changing perspectives on pearly mussels, North America's most imperiled animals. *BioScience*, *54*(5), 429-439. https://doi.org/10.1641/0006-3568(2004)054[0429:CPOPMN]2.0.CO;2

Taeubert, J. E., El-Nobi, G., & Geist, J. (2014). Effects of water temperature on the larval parasitic stage of the thick-shelled river mussel (Unio crassus). *Aquatic Conservation: Marine and Freshwater Ecosystems*, *24*(2), 231-237. https://doi.org/10.1002/aqc.2385

Trenberth, K. E., & Guillemot, C. J. (1996). Physical processes involved in the 1988 drought and 1993 floods in North America. *Journal of Climate*, *9*(6), 1288-1298. https://doi.org/10.1175/1520-0442(1996)009%3C1288:PPIITD%3E2.0.CO;2

U.S. Fish & Wildlife Service, (2022). *ECOS Environmental Conservation Online System.* Retrieved From: https://ecos.fws.gov/ecp/species/2212

USGS. (2021). National Water Information System: Web Interface. Retrieved From: https://waterdata.usgs.gov/nwis/uv?02068500

Vaughn, C. C., & Hakenkamp, C. C. (2001). The functional role of burrowing bivalves in freshwater ecosystems. *Freshwater Biology*, *46*(11), 1431-1446. https://doi.org/10.1046/j.1365-2427.2001.00771.x

Vaughn, C. C., Nichols, S. J., & Spooner, D. E. (2008). Community and foodweb ecology of freshwater mussels. *Journal of the North American Benthological Society*, *27*(2), 409-423. https://doi.org/10.1899/07-058.1

Wächtler, K., Dreher-Mansur, M. C., & Richter, T. (2001). Larval types and early postlarval biology in naiads (Unionoida). In *Ecology and evolution of the freshwater mussels Unionoida* (pp. 93-125). Springer, Berlin, Heidelberg.

Watters, G. T. (1999, March). Freshwater mussels and water quality: A review of the effects of hydrologic and instream habitat alterations. In *Proceedings of the First Freshwater Mollusk Conservation Society Symposium* (Vol. 1999, pp. 261-274). Columbus: Ohio Biological Survey.

Wickham, J., Stehman, S. V., Sorenson, D. G., Gass, L., & Dewitz, J. A. (2021). Thematic accuracy assessment of the NLCD 2016 land cover for the conterminous United States. *Remote Sensing of Environment*, 257, 112357.

Williams, J. D., Warren Jr, M. L., Cummings, K. S., Harris, J. L., & Neves, R. J. (1993). Conservation status of freshwater mussels of the United States and Canada. *Fisheries*, *18*(9), 6-22. https://doi.org/10.1577/1548-8446(1993)018%3C0006:CSOFMO%3E2.0.CO;2

Wolman, M. G. (1954). A method of sampling coarse river-bed material. EOS, Transactions American Geophysical Union, 35(6), 951-956.

Zhao, C., & Brissette, F. (2022). Impacts of large-scale oscillations on climate variability over North America. *Climatic Change*, *173*(1), 1-21.

Zigler, S. J., Newton, T. J., Steuer, J. J., Bartsch, M. R., & Sauer, J. S. (2008). Importance of physical and hydraulic characteristics to unionid mussels: a retrospective analysis in a reach of large river. *Hydrobiologia*, *598*(1), 343-360. DOI 10.1007/s10750-007-9167-1

Chapter 5 Conclusions and Future Research Needs

5.1 Key findings

This research was focused on improving our understanding of sediment and juvenile freshwater mussel transport in rivers and of river-floodplain connectivity as a measure of floodplain sediment deposition.

In Chapter 2, we applied a two-dimensional hydrodynamic model and used simulated model results to estimate the largest sediment size that can be moved in suspension and as bedload at various flows for a range of grain size classes. We proposed a method of probabilistically integrating the largest sediment size that can be moved at various flows to predict the upper end of the grain size distribution in suspension and in bed material, which is applicable to floodplains as well as coastal areas.

In Chapter 3, we developed a 2D HEC-RAS hydrodynamic model for the South River downstream of Waynesboro, Virginia, and used simulated model results with sediment deposition data to create predictive multiple linear regression models describing sedimentation across the floodplain. Our work highlights how floodplain topography and river-floodplain connectivity affect sedimentation rates and can help inform the development of floodplain sediment budgets.

In Chapter 4, we investigated whether changing flow conditions, as they affect juvenile freshwater mussel settling, could be a potential causative factor for the decline of fresh water mussels in the Dan River, North Carolina. We deployed two uplooking velocity sensors on the river bed and collected field measurements. We identified that low flows have been increasing since 2000 that may be exacerbating the decline in freshwater mussel population.

5.2 Suggestions for future research

In Chapter 2, we interpret our results as being most applicable to floodplain channels that are barren or seasonally barren. It is likely that perennial vegetation in floodplain channels would further dampen flow momentum and promote sediment deposition. Fully exploring the vegetation dynamic is a future research direction.

In Chapter 3, we constructed our model for a 48 km reach of the South River but concentrated our analysis on an 8.8 km reach covering three distinct floodplains. In the future, the approach we applied in three floodplains can be extended to the rest of the South River to compile more data relating floodplain topographic variability to spatial distributions of sedimentation rate to better inform the development of floodplain sediment budgets.

In Chapter 4, we identified that changing flow conditions may be responsible for mussel decline. For future work, beyond the streamflow characteristics analyzed herein, investigating the rate of change of a hydrograph rise or streamflow responses that occur without precipitation, and how this has changed over time, should provide insight into the potential role of changing dam operations on low flows.